

Copyright Warning & Restrictions

The copyright law of the United States (Title 17, United States Code) governs the making of photocopies or other reproductions of copyrighted material.

Under certain conditions specified in the law, libraries and archives are authorized to furnish a photocopy or other reproduction. One of these specified conditions is that the photocopy or reproduction is not to be “used for any purpose other than private study, scholarship, or research.” If a user makes a request for, or later uses, a photocopy or reproduction for purposes in excess of “fair use” that user may be liable for copyright infringement,

This institution reserves the right to refuse to accept a copying order if, in its judgment, fulfillment of the order would involve violation of copyright law.

Please Note: The author retains the copyright while the New Jersey Institute of Technology reserves the right to distribute this thesis or dissertation

Printing note: If you do not wish to print this page, then select “Pages from: first page # to: last page #” on the print dialog screen

The Van Houten library has removed some of the personal information and all signatures from the approval page and biographical sketches of theses and dissertations in order to protect the identity of NJIT graduates and faculty.

ABSTRACT

MICROMECHANICS OF HOT MIX ASPHALT MATERIAL FORMULATION AND NUMERICAL SIMULATION

**by
Kuo-Neng G. Chang**

Hot Mix Asphalt (HMA), a highway and airfield pavement material, is heterogeneous, granular, and composite. It is traditionally modeled as a homogeneous material using continuum mechanics or semi-empirical methods. As a result, the above models either neglect or over-simplify component reactions, failing to predict field performance problems resulting from particle segregation. This research presents micromechanical modeling, a novel approach that accounts for the components.

A micromechanical model is developed for HMA by modeling it as an assembly of asphalt cement coated particles. The asphalt cement is modeled as a viscoelastic material. To represent asphalt cement, several viscoelastic elements (i.e. Maxwell, Kelvin-Voigt, and Burgers' elements) were considered. From these viscoelastic elements the Burgers' element is shown to be most representative of asphalt binder behavior based on mechanical responses and comparisons with physical experimental results.

The model for HMA, ASBAL, is based on the TRUBAL program, a Discrete Element Method (DEM), with Burgers' element. Monotonic and cyclic tests were simulated to observe the ability of the model to predict the mechanical behavior of HMA.

During these simulations the physical values of microscopic input parameters were varied to determine how each contributes to the overall behavior of HMA.

Then, the ASBAL model was used to simulate a mechanical test with x-ray tomography to accurately predict residual stresses of the laboratory sample after compaction, the initial modulus, stress levels throughout the test, and number of contacts within HMA matrix.

Using the master curve and the time-temperature superposition theory the input parameters for the Burgers' element at different temperatures were calculated. Using those input parameters, the mechanical responses of HMA at different temperatures were simulated. Results show that at higher temperatures the strength and initial stiffness values are a fraction of those found at lower temperatures. Hence the ASBAL model predicts the temperature softening of HMA that contributes to the rutting of HMA. The micromechanical model simulates the discrete mechanical behavior of HMA and hence can be used to develop performance based tests for HMA.

**MICROMECHANICS OF HOT MIX ASPHALT
MATERIAL FORMULATION AND NUMERICAL SIMULATION**

by
Kuo-Neng G. Chang

**A Dissertation
Submitted to the Faculty of
New Jersey Institute of Technology
in Partial Fulfillment of the Requirements for the Degree of
Doctor of Philosophy**

Department of Civil and Environmental Engineering

May 1995

Copy Right © 1995 by Kuo-Neng G. Chang

ALL RIGHTS RESERVED

Blank Page

APPROVAL PAGE

**MICROMECHANICS OF HOT MIX ASPHALT
MATERIAL FORMULATION AND NUMERICAL SIMULATION**

Kuo-Neng G. Chang

Dr. Namunu J. Meegoda, Dissertation Adviser
Associate Professor of Civil and Environmental Engineering, NJIT

Date

Dr. Raj P. Khera, Committee Member
Professor of Civil and Environmental Engineering, NJIT

Date

Dr. Dorairaja Raghu, Committee Member
Professor of Civil and Environmental Engineering, NJIT

Date

Dr. Jonathan Luke, Committee Member
Associate Professor of Mathematics, NJIT

Date

Dr. Anthony Rosato, Committee Member
Professor of Mechanical Engineering, NJIT

Date

BIOGRAPHICAL SKETCH

Author: Kuo-Neng G. Chang
Degree: Doctor of Philosophy
Date: May 1995

Undergraduate and Graduate Education:

- Doctor of Philosophy in Civil Engineering, New Jersey Institute of Technology, Newark, NJ 1995
- Master of Science in Civil Engineering, New Jersey Institute of Technology, Newark, NJ 1991
- Bachelor of Science in Agricultural Engineering, National Taiwan University, Taipei, Taiwan, R.O.C., 1986

Major: Civil Engineering

Publications:

Meegoda, N.J., and Chang, K.G. (1995). "Modeling the Heterogeneity of Hot Mix Asphalt Using Discrete Element Methods," to be presented at the ASCE Engineering Mechanics Conference, Boulder, Colorado.

Chang, K.G., Meegoda, N.J., and Khera, R.P. (1995). "Centrifugal Modeling of Underground Storage Tanks", to be presented at the 74th Annual Meeting of Transportation Research Board.

Meegoda, N.J. and Chang, K.G. (1994). "Modeling Viscoelastic Behaviors of Hot Mix Asphalt Using Discrete Element Method", ASCE Specialty Conference in Material Engineering, San Diego, November, pp. 804 - 811.

Meegoda, N.J., and Chang, K.G. (1993). "A Novel Approach to Develop a Performance Based Test for Rutting of Asphalt Concrete," Proceedings of ASCE Specialty Conference, Airport Pavement Innovations, (Edited by Jim W. Hall, Jr.), Theory to Practice, on September 8 - 10, pp. 126-140.

- Chang, K.G., and Meegoda, N.J. (1993). "Simulation of the Behavior of Asphalt Concrete Using Discrete Element Methods," Proceedings, The Second International Conference on Discrete Element Methods, Massachusetts Institute of Technology, Boston, MA, March 18 - 19, pp. 437 - 448.
- Chang, K.G., and Hsu, N.S. (1989). "Introduction to A Standardized System for Evaluating Groundwater Pollution Potential --- DRASTIC", Taiwan Water Conservancy, ISSN 0492 - 1550, No. 4, Vol. 137, June.
- Wu, S., Chang, K.G., Hsu, N.S. , and Chang, J.K. (1989). "A Study of Strategies for Groundwater Contamination Protection with Case Studies", ROC EPA, Taipei, Taiwan.

This dissertation is dedicated to my parents
Hai-Sung Chang and Lan-In Lan

ACKNOWLEDGMENTS

I would like to express my appreciation to my advisor, Dr. Nanumu J. Meegoda for his guidance and advice throughout the past five precious years of my life. Special thanks are also due to members of advisory committee for their valuable advice and suggestions.

I am grateful forever to my parents for their love and to my wife Wendy, whose patience and encouragement has made this success possible.

I finally thank my friend Dave Washington, for his help and support. I am also indebted to my friends (and their families), Lily Meegoda, Cliff Heath, Geoff Rowe, Nona Rutter, Dawn and Bill for their unselfish friendship.

TABLE OF CONTENTS

Chapter	Page
1.0 OVERVIEW	1
1.1 HMA as a Pavement Material	1
1.2 New Specifications from SHRP Asphalt Research Program	2
1.3 The Needs for Better Understanding of HMA.....	3
1.4 The Scope of this Dissertation	4
1.5 Organization of this Dissertation.....	5
1.5.1 Part I: Material Formulation (Chapter 2).....	5
1.5.2 Part II: Numerical Simulation (Chapters 3 and 4).....	6
2.0 MATERIAL FORMULATION	7
2.1 Introduction	7
2.2 Design Methods of Asphalt Concrete	8
2.3 Microscopic Modeling.....	10
2.4 Modeling of Asphalt Cement	16
2.5 Constitutive Laws for the Elements - under Monotonic Loading.....	20
2.5.1 Maxwell Element.....	20
2.5.2 Kelvin-Voigt Element.....	21
2.5.3 Burgers' Element.....	22
2.5.4 Simulations of Constant Strain-rate Tests	26
2.6 Constitutive Laws for the Elements under Cyclic Loading	28
3.0 NUMERICAL SIMULATION - ISOTHERMAL CASES	36

TABLE OF CONTENTS (Continued)

Chapter	Page
3.1 Introduction	36
3.1.1 Viscoelastic Behavior and Discrete Characteristics of Hot Mixed Asphalt	36
3.2 Discrete Element Methods.....	36
3.3 A Model based on A Discrete Element Method for <i>HMA</i>	37
3.3.1 Adaptation of TRUBAL Program to Model HMA.....	37
3.3.2 Material Models of Asphalt Binder and Aggregates	38
3.3.3 Contacts.....	40
3.3.4 Computation Procedure in <i>ASBAL</i>	41
3.3.5 Force-Displacement Laws and Separation Criteria for Particles in <i>ASFORD</i> Subroutine	44
3.3.6 Simulation of Mechanical Behavior of HMA.....	48
3.4 Numerical Simulation of <i>HMA</i> using the <i>ASBAL</i> Program	49
3.4.1 Input Parameters	50
3.5 Results	54
3.5.1 The 150-particle Simulation.....	54
3.5.2 The 512-particle Simulation.....	64
4.0 NUMERICAL SIMULATION - TEMPERATURE EFFECTS	68
4.1 Introduction	68
4.2 Characterizing Rheological Properties of Asphalt Binder at Different Temperature	69

TABLE OF CONTENTS (Continued)

Chapter	Page
4.2.1 Van der Poel's Nomograph	69
4.2.2 SHRP Specification for Asphalt Binder.....	69
4.3 Obtaining Input Parameters at Different Temperatures for ASBAL.....	70
4.3.1 The Characteristic Parameters for Binders	70
4.3.2 SHRP Core Binder - AAB-1 (Tank)	71
4.3.3 Estimating the Dynamic Complex Modulus and Phase Angle using SHRP Equations.....	72
4.3.4 Shift Factors and Construction of Master Curves at Different Temperatures.....	74
4.3.5 Back-calculation of Input Parameters for Burgers' Element from The Master Curves	76
4.3.6 Other Parameters.....	79
4.4 ASBAL Simulation of HMA at Different Temperatures.....	80
4.4.1 Simulation of Unconfined Compression Tests	80
4.4.2 Simulation of Constant-P Tests.....	83
5.0 SUMMARY AND CONCLUSIONS	87
5.1 Material Formulation.....	87
5.2 Numerical Simulation	88
APPENDIX A CONTACT AREA OF TWO-ASPHALT COATED PARTICLES..	91
APPENDIX B ASFORD SUBROUTINE.....	96

TABLE OF CONTENTS **(Continued)**

Chapter	Page
APPENDIX C USERS' MANUAL FOR ASBAL.....	107
APPENDIX D SAMPLE INPUT FILES FOR ASBAL	121
APPENDIX E METHOD OF MICROMECHANICAL LABORATORY TESTS FOR HMA	138
APPENDIX F TIME-TEMPERATURE SUPERPOSITION THEOREM FOR ASPHALT	153
APPENDIX G OBTAINING PARAMETERS OF TWO-PARALLEL- MAXWELL ELEMENT FROM SHRP BINDER AAB-1 (TANK) MASTER CURVES	167
APPENDIX H CONVERSION BETWEEN TWO-PARALLEL-MAXWELL MODEL AND BURGER' MODEL	174
REFERENCES	177

LIST OF TABLES

Table	Page
2.1 Input Parameters for Constitutive Equations	26
2.2 Complex Moduli for Linear Viscoelastic Elements	28
2.3 Parameters for Calculating the Complex Moduli.....	32
3.1 Micro-parameters at Different Stages of Simulation (150-particle)	55
4.1 The Shift Factors Based on Time-Temperature Superposition	76
4.2 Linear Viscoelastic Parameters for the SHRP Binder (AAB-1, Tank)	78
4.3 Input Parameters for Asphalt and Particle Properties at Different Temperatures	79

LIST OF FIGURES

Figure	Page
2.1 Micromechanical System of HMA.....	11
2.2 Process of Re-constructing HMA using Micromechanics.....	13
2.3 Linking the Microscopic Parameters and Macroscopic Behavior	17
2.4 Response of Maxwell Element	29
2.5 Response of Kelvin Element.....	30
2.6 Response of Burgers' Element	31
2.7 Laboratory Test Data for an Asphalt Binder (SHRP, AAB-1, Tank).....	33
2.8 Complex Moduli of Maxwell Element	34
2.9 Complex Moduli of Kelvin Element	34
2.10 Complex Moduli of Burgers' Element	35
3.1 Basic Response of Burgers' Element.....	39
3.2 Contact Classification	42
3.3 Flowchart of ASBAL Program.....	43
3.4 Diagram of Coordinate System in DEM	44
3.5 150-particle Simulation (1 of 4)	55
3.6 150-particle Simulation (2 of 4)	56
3.7 150-particle Simulation (3 of 4)	56
3.8 150-particle Simulation (4 of 4)	57
3.9 A Snapshot of a Simulated HMA Assembly After Compaction.....	58

LIST OF FIGURES (Continued)

Figure	Page
3.10 Aggregate Particle Movement in a Simulated HMA (Stage 1)	58
3.11 Aggregate Particle Movement in a Simulated HMA (Stage 2)	59
3.12 Aggregate Particle Movement in a Simulated HMA (Stage 3)	59
3.13 Aggregate Particle Movement in a Simulated HMA (Stage 4)	60
3.14 Aggregate Particle Movement in a Simulated HMA (Stage 5)	60
3.15 Max. Relative Displacement and Max. Incremental Rotation at Different Stages	61
3.16 Principal Stress and Contact Sliding at Different Stages.....	62
3.17 Effects of Asphalt Binder Thickness (1 of 2)	62
3.18 Effects of Asphalt Binder Thickness (2 of 2)	63
3.19 Compression vs. Extension Tests (1 of 2).....	63
3.20 Compression vs. Extension Tests (2 of 2).....	64
3.21 Simulation of a Laboratory Test (1 of 3)	65
3.22 Simulation of a Laboratory Test (2 of 3)	66
3.23 Simulation of a Laboratory Test (3 of 3)	67
4.1 Typical Master Curve for Asphalt Binder with Characteristic Parameters	71
4.2 Master Curve of SHRP Binder (AAB-1, Tank) at 25°C.....	74
4.3 Master Curves of SHRP Binder (AAB-1, Tank) at Different Temperatures	77
4.4 Simulation of Unconfined Compression Tests (1 of 5).....	81
4.5 Simulation of Unconfined Compression Tests (2 of 5).....	81

LIST OF FIGURES
(Continued)

Figure	Page
4.6 Simulation of Unconfined Compression Tests (3 of 5).....	82
4.7 Simulation of Unconfined Compression Tests (4 of 5).....	82
4.8 Simulation of Unconfined Compression Tests (5 of 5).....	83
4.9 Simulation of Constant-P Tests (1 of 5)	84
4.10 Simulation of Constant-P Tests (2 of 5)	85
4.11 Simulation of Constant-P Tests (3 of 5)	85
4.12 Simulation of Constant-P Tests (4 of 5)	86
4.13 Simulation of Constant-P Tests (5 of 5)	86

CHAPTER 1

OVERVIEW

1.1 HMA as a Pavement Material

Asphalt concrete or Hot Mix Asphalt (HMA) is a composite material used in road pavements. There are more than 2.2 million miles of engineered roads in the United States that are covered with HMA. In addition, concrete pavement restoration often includes HMA overlay. Annual expenditure on construction and maintenance of these asphalt pavements is more than \$80 billion. Improvement in specification tests and design procedures for HMA can potentially save millions of dollars and reduce traffic problems associated with lane closures. The National Research Council of Transportation Research Board has estimated that improving the durability of roads and bridges by a single percentage over a 20-year period would yield a saving of \$10 billion to \$30 billion. Even though the use of HMA can be traced back to 1860s, the behavior of HMA is not well understood. In addition, the behavior of HMA is influenced by variables such as project size, production rate, and transportation and construction variables (e.g. segregation, temperature, routing of transportation, etc.).

If HMA is not adequately designed and constructed, common HMA problems such as rutting, fatigue cracking, raveling, etc., can jeopardize the performance of asphalt pavement. The current mix design methods (e.g. Marshall and Hveem) do not consider fundamental engineering properties of compacted HMA subjected to actual traffic loads. Furthermore, the current tests are not performance-based tests and, hence, the designed pavement based on the current methods might result in pre-mature failures.

1.2 New Specifications from SHRP Asphalt Research Program

The Strategic Highway Research Program (SHRP) conducted an extensive research over a period of five years to develop performance based test methods for HMA. This research costing \$50 million lasted between October 1987 and March 1993. Now the Federal Highway Administration (FHWA) is implementing SHRP research products. Out of 130 SHRP products, only the well-developed products will be adopted by the highway agency and the industry.

The major SHRP product for asphalt is SUPERPAVE (SUPERPAVE, 1994). It attempts to integrate all the SHRP asphalt research from the binder to mix designs. SUPERPAVE is a design system to construct asphalt pavements that will last longer without rutting and cracking. This system includes:

- Performance-based specifications for asphalt binder and mixes,
- Accelerated tests to estimate the expected performance of different asphalt binders and mixes,
- A comprehensive and user-friendly mix design system for the new specifications.

The impact of the new specification on the Federal/State Departments of Transportation as well as the highway/airfield pavement industries is revolutionary. However, some fundamental factors such as anisotropic and discrete nature of HMA are not considered in SHRP research. Some of fundamental issues are discussed in the following section.

1.3 The Needs for Better Understanding of HMA

HMA consists of compacted granular aggregates (about 85% by volume) coated with viscoelastic asphalt cement. The predictive phenomenological models have limited success in explaining the mechanisms, origin, and propagation of pavement distress. Considerable movement and rotation of aggregates under repeated heavy traffic loads have been observed. Even though the effects of binding characteristics and the behavior of HMA were studied by SHRP, there were no attempts to include the discrete nature of HMA in tests for specifications and in designs.

HMA is a heterogeneous, history-dependent composite material. The properties of aggregates and asphalt cement along with their interface make the HMA a composite material with complicated stress-strain behavior. Most researchers have studied the properties of HMA using either physical tests combined with constitutive models. In those attempts HMA is considered as elastic, viscoelastic, plastic or viscoelastic-plastic material. Numerical methods such as finite difference, finite element or boundary element techniques have been used to study the performance of HMA. HMA is a composite material with individual movement of particles and, hence the above modeling techniques may over-simplify the heterogeneous, discrete behavior of HMA. Therefore, it is considered difficult to completely explain or predict the phenomena of rutting and fatigue cracking as well as the movement of granular particles within HMA using macroscopic models.

Even though the SHRP program investigated the fundamental properties of HMA and its components, they are not included in design of HMA. The SUPERPAVE mix

design system currently uses empirical performance-based aggregate properties in its specifications. A microscopic study of the HMA to include fundamental material properties to predict the macroscopic behavior of HMA can bridge this gap. The microscopic behaviors of asphalt binder can be studied using a spring-dashpot system. The displacement of asphalt coated aggregates due to applied loads can be computed by a microscopic model that considers the mechanics of particulate materials.

1.4 The Scope of this Dissertation

In this dissertation, the microscopic behaviors of components of HMA are studied to develop the material formulation that is used in a micromechanical model for HMA. This micromechanical model is based on Discrete Element Method (DEM). The model simulated the mechanical behavior of HMA.

The HMA is then treated as an assembly of asphalt coated aggregates. Each contact (either aggregate-asphalt-aggregate or aggregate-aggregate) is represented by springs and Burgers' elements in normal and tangential directions at contact. Prediction of macroscopic behaviors of HMA using micromechanics is achieved by an averaging process (i.e. by summing up the all the particle interactions). Similarly, by knowing the macro parameters such as strain and stress one could obtain the microscopic parameters such as number of contacts through a process called localization.

TRUBAL program, a microscopic model for soil based on DEM, was modified to include the asphalt binder. The resulting program termed ASBAL was used to simulate idealized HMA and to study the mechanical behavior of HMA using microscopic input

parameters. Then, the ASBAL program was validated by simulating and comparing with results of a carefully conducted laboratory test with x-ray tomography.

1.5 Organization of this Dissertation

This dissertation includes two sections: Part I, Material Formulation (Chapter 2) and Part II, Numerical Simulations (Chapters 3 and 4). Chapter 5 is a Summary and Conclusions.

1.5.1 Part I: Material Formulation (Chapter 2)

In Part I, micromechanics of components of hot mix asphalt is investigated and the material formulation is made to be used in a micromechanical model. Microscopic properties of the components of hot mix asphalt, i.e. aggregate and asphalt binder, are discussed in details. The behavior of basic viscoelastic elements such Maxwell, Kelvin, and Burgers' are derived. By comparing with the performance of asphalt binder the most appropriate linear viscoelastic element, Burgers' element, is selected to be used in a micromechanical model.

1.5.2 Part II: Numerical Simulation (Chapters 3 and 4)

TRUBAL, a model based on Discrete Element Methods (DEM), was modified to simulate HMA. The Burgers' element was included to account for asphalt binder in HMA. This model simulated a carefully conducted physical test with x-ray tomography. The comparison of simulation with physical tests demonstrates the ability of this model to study the discrete nature of HMA. The influence of microscopic parameters on

macroscopic behavior is studied by changing the physical values of microscopic parameters (asphalt binder thickness, aggregate particle, and asphalt-particle interface, etc.). The effects of temperature on the physical behavior of HMA are studied by using the results of a SHRP binder, AAB-1 (Tank) at different temperatures.

CHAPTER 2

MATERIAL FORMULATION

2.1 Introduction

Hot Mixed Asphalt (*HMA*) or Asphalt Concrete (*AC*), a mixture made of aggregates (about 85% by volume) and asphalt binder, is a heterogeneous, particulate, and composite material. Currently, design of *HMA* is based on continuum theories (e.g. linear elastic theories) or semi-empirical methods (e.g. design charts or monographs). By treating the asphalt-cemented granular assemblies as a homogeneous material, the above method can not account for the discrete nature of *HMA* and the interactions of *HMA* components explicitly. Therefore, the recurring pavement problems such as rutting, thermal cracking and fatigue can not be accounted explicitly by this continuum approach.

The Strategic Highway Research Program (SHRP) of the US Department of Transportation recently investigated the fundamental properties of *HMA* and its components, but the material investigation (such as: the role of aggregate contacts on the *HMA* performance) is not included in the design of *HMA*. Though a performance-based asphalt binder specification and *SUPER-PAVE* (Asphalt Institute, 1994), a mix design system, were developed by *SHRP*, the basic mechanics of materials is not the basis for this performance-based specification for *HMA*. The author is proposing to bridge the above gap by studying the micromechanical behavior of *HMA* and by including fundamental material properties to performance-based specification for design and construction of *HMA*. The microscopic behavior of *HMA* was modeled in an earlier attempt using a spring-dashpot system (Hookean spring for aggregates and Kelvin element for asphalt

binder) to simulate the mechanical deformation of *HMA*. (Chang and Meegoda, 1993). Meegoda and Chang, 1993, showed that aggregates were displaced and rutting or permanent deformation occurred due to applied loads. The above model was refined in this research to include the ability of the binder to simulate all the possible loading and environmental conditions.

2.2 Design Methods of Asphalt Concrete

Macroscopic approaches were used in design of *HMA* traditionally. The following methods are examples of such attempts: multi-layer elastic theories (e.g. *ELSYM* program by Ahlborn, 1972), multi-layer elastic systems with non-linear soil models (e.g. *PADAL* program by Tam and Brown, 1988), and macroscopic viscoelastic models used by the *SHRP* program and *FEM* pavement programs such as *PACE* program (SWK(PE), Inc., 1994) and 3-D Dynamic FEM (White et al., 1995). All the above methods, with increased complexities, were mainly developed for structural analysis of *HMA* pavements. The fundamental viscoelastic properties of *HMA* were still considered macroscopically, i.e., the *HMA* is treated as a homogeneous elastic/viscoelastic material although it is a discrete heterogeneous material.

Linear viscoelastic elements are used to model *HMA*, but it is incorrect to apply linear viscoelastic models to explain the macroscopic behavior of *HMA*. The aggregate contacts are ignored when *HMA* is modeled as a single linear viscoelastic material. The inability of macroscopic linear viscoelastic models to simulate the behavior of *HMA* at engineering stress/strain levels limits their use in mechanical analysis (Pagen, 1972; Alavi,

1992). This is the reason for limited applicability of the time-temperature equivalence and superposition theories (Ward, 1983) for *HMA* test data. Even though the time-temperature superposition theory is successfully applied to the asphalt cement (Anderson et al., 1994), the complex mechanical behavior of *HMA* can not be captured by a few springs and dashpots. Therefore, to understand the mechanical behavior of *HMA* one should look at the contributing factors:

- *Properties of Components*: They include properties of aggregate (e.g. sizes, shapes, and modulus, etc.), properties of asphalt binder (e.g. grading, modulus, steady-state viscosity, cohesion, and asphalt modifier or additives, etc.), and the asphalt-aggregate interactions (adhesion and absorption, etc.).
- *Changes in Internal Structure*: e.g. The numbers of contacts and their distribution, the packing of asphalt coated aggregates (gradation of aggregates and type of compaction), degree of compaction (i.e. air void content), and content of asphalt binder.
- *Loading History*: the performance of *HMA* is sensitive to the loading history, such as: magnitude or frequency of loading, duration of loading cycles - including the rest periods, etc.
- *Environmental Factors*: Daily and seasonal temperature variations may affect the rutting rates and fatigue lives of *HMA*. The presence of moisture may affect the adhesive failure and cohesive failure and may cause stripping.

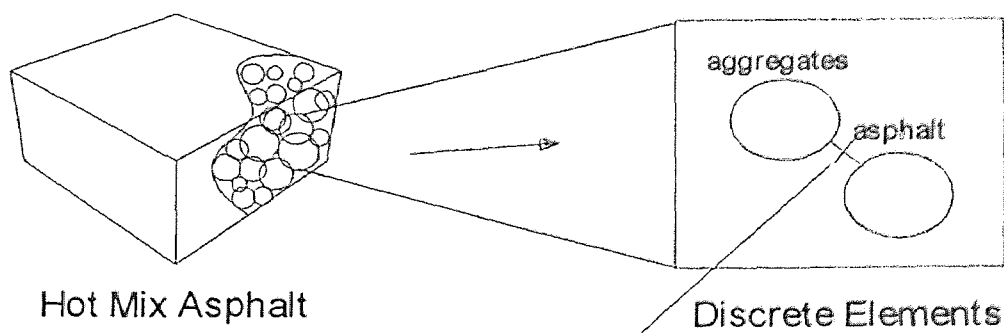
The above factors play active roles in the mechanical behavior of *HMA*. Therefore, one should include all the above factors to predict the behavior and

performance of asphalt concrete pavement. The only logical way is to use the micromechanics of asphalt concrete where all the above factors are included in the modeling. Then, it should be brought to the macroscale to be used in engineering designs.

2.3 Microscopic Modeling

The microscopic models consider the changes in internal structures, properties of components and interactions between aggregates and asphalt binder. Therefore, microscopic models of HMA can include most of the important factors that govern the performance of *HMA*. Microscopic models based on Discrete Element Method (DEM) (Cundall and Hart, 1990) can be adopted to study the behavior of *HMA*. Models based on DEM include fundamental theories such as: linear or non-linear contact laws at the microscopic level.

In this model *HMA* specimen is re-constructed with a given number of aggregates coated with asphalt cement. The asphalt cement is microscopically represented by two sets of viscoelastic elements in normal and tangential directions at each contact (see Figure 2.1). The number of viscoelastic elements for a given specimen depends on the number of asphalt-coated aggregate contacts. The aggregates in contact are represented by a mass with a moment of inertia and Hookean springs in the normal and tangential directions at each contact. Each contact is either an aggregate-asphalt-aggregate contact or an aggregate-aggregate contact.



represented by

Linear Viscoelastic Elements

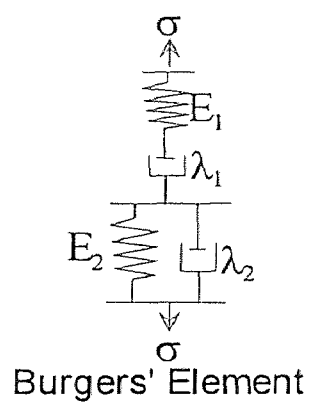
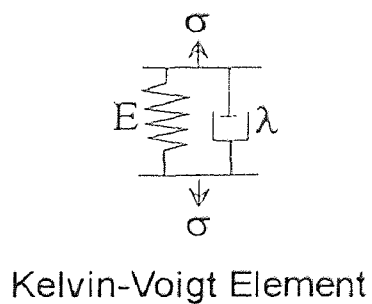
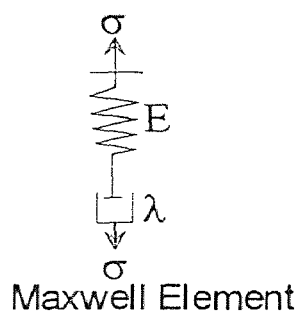


Figure 2.1 Micromechanical System of *HMA*

Mixing and compaction of *HMA* is simulated at a specific *VMA* (voids in mineral aggregates) with a random packing. *VMA* is defined as the volume of intra-granular void space between the aggregate particles of a compacted *HMA*. It includes the air voids and volume of the asphalt (Roberts et al., 1991). The specimen is compacted by applying a specific strain-rate from three global principal axes at the boundaries. Different methods of compaction, such as isotropic or uni-axial compaction can be applied. The compacted assemblage is then ready to be tested under different modes (see Figure 2.2).

Once an external force or displacement is applied during compaction or testing, the propagation of stress/strain will be initiated on the boundary and continued through the entire assemblage based on force-displacement laws and equations of motion. To eliminate the boundary effects, periodic spaces are used in this study. Thus, a repeated portion (i.e. periodic space) within a sample was extracted. All the elements or components are allowed to deform, move and rotate. Therefore, the energy dissipation through friction, contacts, and global damping can be described at a microscopic scale.

The movement of aggregates follows Newton's Second Law for and the movement includes displacement and rotation:

$$\sum_{n=1}^N (F_i)_n = \sum_{n=1}^N m(\ddot{x}_i)_n \quad (2.1)$$

$$\sum_{n=1}^N (M_i)_n = \sum_{n=1}^N I(\ddot{\theta}_i)_n \quad (2.2)$$

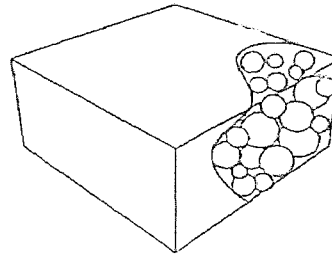
where F : microscopic contact force;

m : mass of aggregate particle;

\ddot{x} : displacement acceleration;

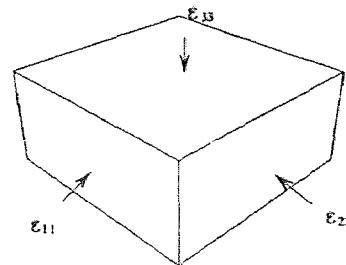
Generation of Particles

Randomly generate a specified number of particles with a specific gradation in a periodic space. Properties of the particles and the asphalt coating are assigned.



Compaction of Samples

The sample can be compacted by a strain-controlled boundary. Strain rates in the principal axes directions are specified. Isotropic or uniaxial compaction can be simulated.



Testing of Samples

Several tests can be simulated by a given set of strain rates, e.g. uniaxial test, biaxial test, simple shear test, etc. Loading/unloading and cyclic loading can also be simulated.

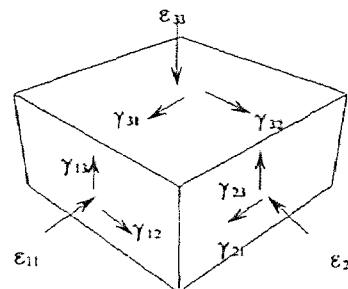


Figure 2.2 Process of Reconstructing *HMA* using Micromechanics

$\ddot{\theta}$: angular acceleration;

subscript i : 1 to 3 corresponding to three local axial directions;

subscript n : 1 to N corresponding to the number of contacts for a given aggregate particle.

The linear and angular accelerations are used to calculate particle displacement and rotation. The dynamic system of HMA is modeled using a quasi-static approach. The critical time-step is calculated using the mass and stiffness of two aggregate particles in contact. Fraction of the critical time-step is used in the numerical computations to model the actual particle assembly. Contact damping (operating on the relative velocities at the contacts) and/or global damping (operating on the absolute velocities of the aggregate particles) are used to ensure that the assembly is in a state of equilibrium at all time.

The contact force obeys the material models of the asphalt binder and aggregates (i.e. linear or non-linear elastic models for aggregates and linear viscoelastic models for asphalt binder).

$$\Delta F_j^p = f^p(\Delta u) \quad (2.3)$$

$$\Delta F_j^a = f^a(\Delta u) \quad (2.4)$$

where ΔF : incremental contact force;

$f^p(\Delta u)$: material models of aggregate particles, either linear elastic spring or Hertz-Mindlin (non-linear elastic) contact laws (Mindlin, 1949);

$f^a(\Delta u)$: linear viscoelastic models such as: Maxwell, Kelvin, or Burgers models;

Δu : linear or angular displacement;

subscript j : in normal or shear direction at the contact;

M : angular momentum;

I : moment of inertia of aggregate particle;

superscripts p or a : “ p ” for particles and “ a ” for asphalt binder.

Any widely accepted failure criteria for material (such as Mohr-Coulomb or Cap models) can be used to model the failure of bonding between components. In this research maximum shear force at contacts is calculated using Mohr-Coulomb failure criteria (Cundall and Strack, 1979):

$$F_s^{\max} = F_n \tan(\phi) + C_m A_{ct} \quad (2.5)$$

where F_n : normal force at the contact;

ϕ : angle of internal friction for the contact;

C_m : cohesion or adhesion of the material at the contact;

subscript m : asphalt-aggregate-asphalt contact or aggregate-aggregate contact;

A_{ct} : contact area.

Once the shear force exceeds the maximum shear force, the slide occurs and the stresses on the yield surfaces can be corrected by multiplying an adjustment factor, such as (Cundall and Hart, 1990):

$$(F_s)_{i(\text{new})} = (F_s)_{i(\text{old})} \times \frac{F_s^{\max}}{|F_s|} \quad (2.6)$$

where $(F_s)_i$: the components of shear force in principal axis directions and

$$|F_s| = \sqrt{\sum (F_s)_{i(\text{old})}^2};$$

subscript i : 1 to 3 for the three principal axes.

The force on each particle can be resolved into three directions of the global coordination and added to compute global stresses, i.e., macroscopic stresses. This is how the models based on DEM bring the micro-scale behavior to working, engineering or macroscale. This process is termed averaging process (Cambou, 1993). On the other hand, for a given global stress or strain level program is capable of providing the contact forces and movements for each particle, i.e., knowing the macro-parameters one can obtain the micromechanical behavior. This is termed the localization process (Cambou, 1993). Figure 2.3 illustrated the averaging and localization processes.

This model is capable of simulating an assembly of particles with different sizes, shapes, and surface properties. A given gradation of particles can be packed randomly to reproduce the real *HMA*. This micromechanical model also has the potential to be used to develop/validate the performance-based tests and incorporate into finite element analysis.

To implement the modeling one should properly characterize the components. Since the TRUBAL model based on DEM is capable of modeling the behavior of a granular packing only the asphalt cement should be completely characterized and included.

The material formulation obtained in this research will be used in Chapter 3: Numerical Simulation to simulate the behavior of *HMA* using this microscopic model.

2.4 Modeling of Asphalt Cement

The asphalt coating (about 5% of the diameter of the aggregate particle) on each particle can be described mathematically by using a linear viscoelastic element.

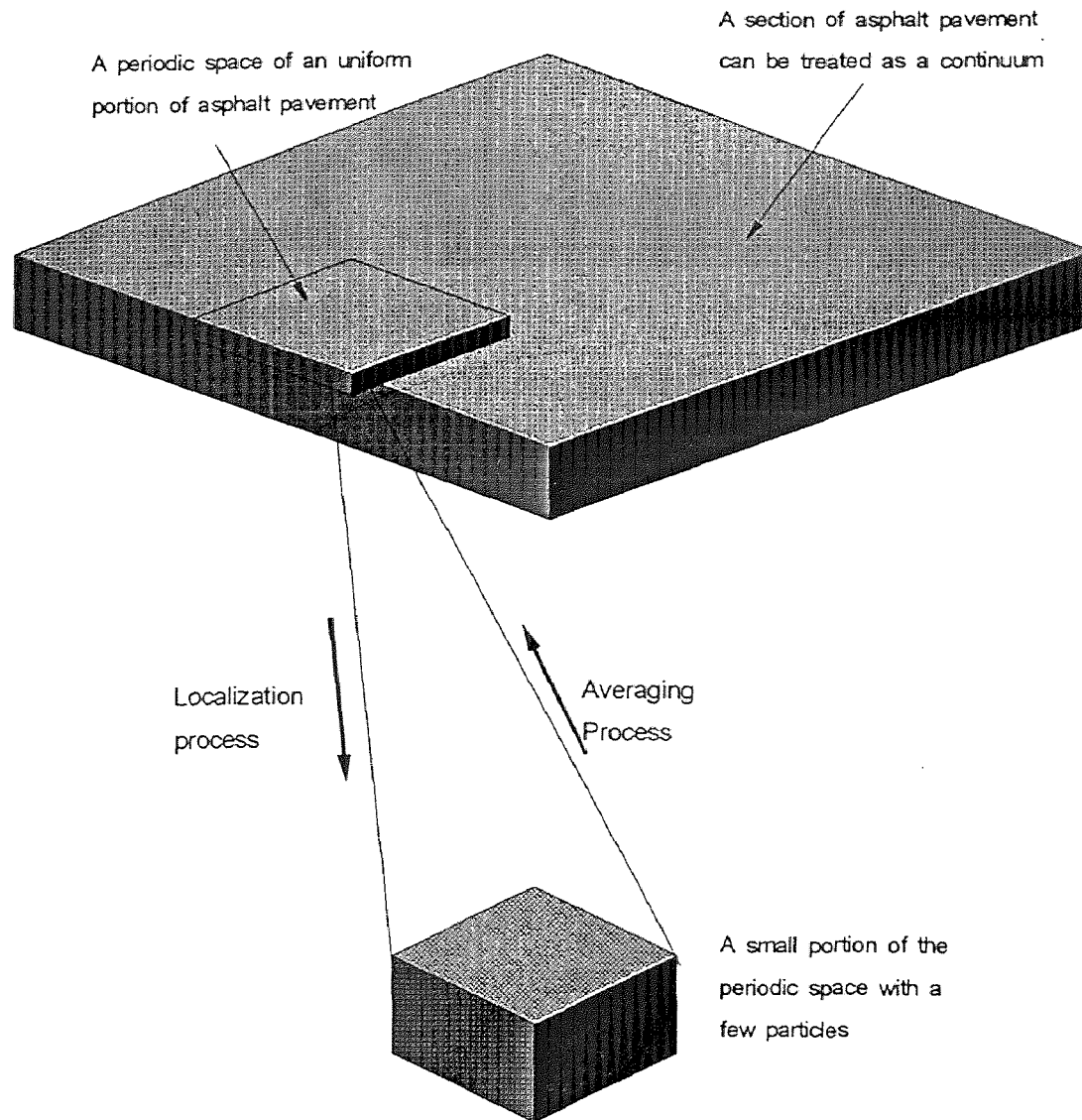


Figure 2.3 Linking the Microscopic Parameters and Macroscopic Behavior

Asphalt binder contains organic molecules that vary from non-polar saturated hydrocarbons to polar aromatic ring structures. In the past, the following laboratory tests were used to classify and index asphalt cement:

1. Penetration (at 25 °C),
2. Absolute viscosity (at 60 °C);
3. Ring-and-ball softening point temperature;
4. kinematics viscosity (at 135 °C);
5. Thin-film oven test (*TFOT*) residue.

Use of additives to asphalt binder forming stable bonds and cross-links in chemical structure requires additional tests.

The new SHRP specification for asphalt binder is based on linearity and thermo-simplicity of viscoelastic theories. Linearity holds only if stress is proportional to strain (or strain-rate) at the given time when the linear superposition principle is valid. Thermo-simplicity holds when time-temperature superposition is valid and the master curve for a specific binder can be constructed by shifting dynamic shear test data to a common temperature. Therefore, the proposed parameters for classifying an asphalt binder include: complex modulus, steady-state viscosity, cross-over frequency (the frequency when storage modulus equal to loss modulus), and rheological index (which is related to relaxation spectrum) (Chritensen and Anderson, 1992; Bashia, et al., 1992).

The SHRP program recommended: 1) the use of dynamic shear rheometer to characterize asphalt binder within a wide range of temperatures/loading frequencies; 2) the use of bending beam rheometer to characterize the low temperature rheology of asphalt

binder, 3) the use of direct tension tester to measure the failure strain for asphalt binders; 4) the use of both Rolling Thin-Film Oven Test (RTFOT) and Pressure Aging Vessel (PAV) tests to characterize the aging of asphalt binder. These tests simulate binder aging during mixing and five-year field aging, respectively. SHRP researchers believe that the above tests are adequate to evaluate rutting, fatigue cracking, and low temperature cracking of asphalt binder.

Results from the above tests provided very useful information for microscopic modeling of asphalt concrete. It was also brought to the attention of the author that choice of viscoelastic element for asphalt cement in the DEM-based models should be based on in-depth analysis of the behavior of elements rather than the arbitrary selection of viscoelastic element (i.e., it is incorrect to arbitrarily adopt Kelvin element for DEM modeling of HMA, [Chang and Meegoda, 1993]). Therefore, an in-depth analysis of the following basic viscoelastic elements was performed to select the suitable viscoelastic element for this research. The following basic viscoelastic elements were considered: Maxwell, Kelvin-Voigt, and Burgers' elements.

From the rheology point of view, all materials exhibit some forms of solidity and liquidity. Therefore, it is appropriate to use the combinations of linear solid elements (i.e. springs) and viscous elements (dashpots) to represent mechanical properties of a material. The linear theory of viscoelasticity mathematically describe the behavior of material responses under various stresses conditions. By introducing the above theory to a wide spectrum of stresses Findley, et al., 1976 solved the wave propagation problems and showed reasonable agreements with physical experiments.

In the following sections, the basic responses of linear viscoelastic elements (Maxwell elements, Kelvin-Voigt elements, and Burgers' elements) are derived and compared. These are the simplest linear viscoelastic elements that can reasonably describe the viscoelastic responses of asphalt binders. The basic response of linear viscoelastic elements consists of: instantaneous elasticity, creep under constant stress, stress relaxation under constant strain, instantaneous recovery, delayed recovery, permanent set or plastic deformation. Then, complex moduli of linear viscoelastic elements were obtained (Findley et al., 1976) and compared with laboratory test data to select the appropriate element to be used to represent asphalt binder in the subsequent discrete element model.

The ability of viscoelastic elements to simulate the creep test and relaxation test results makes the elements properly represent viscoelastic materials. The ability of the viscoelastic elements to simulate tests under oscillating or sinusoidal for a wide range of loading rates further validate the applicability of those elements.

2.5 Constitutive Laws for the Elements - under Monotonic Loading

2.5.1 Maxwell Element

Maxwell element is a two-component model consisted of a linear spring and a viscous dashpot in series. Maxwell element shows linear creep and instant recovery under constant stress tests and exponential relaxation under constant strain tests. The stress-strain relationship for Maxwell element is given below. Figure 2.1 shows that the total strain rate is the sum of strain-rate from the dashpot and spring.

$$\dot{\varepsilon} = \frac{\dot{\sigma}}{E} + \frac{\sigma}{\lambda} \quad (2.7)$$

where ε : strain of element,

σ : stress of element,

E: Young's modulus of a Hookean elastic spring,

λ : viscosity of a Newtonian viscous dashpot.

For constant strain-rate tests, the above equation can be expressed as:

$$\dot{\sigma} + \frac{E}{\lambda} \sigma = E \dot{\varepsilon}_o H(t) \quad (2.8)$$

where $\dot{\varepsilon}_o$: A value of constant strain-rate;

$H(t)$: Unit step function or Heaviside unit function.

By taking the Laplace transform of equation (2.8) and we get:

$$\left(s \hat{\sigma}(s) - \sigma(0) \right) + \frac{E}{\lambda} \hat{\sigma}(s) = \frac{E \dot{\varepsilon}_o}{s} \quad (2.9)$$

or

$$\hat{\sigma}(s) = \lambda \dot{\varepsilon}_o \left(\frac{1}{s} - \frac{1}{s + E/\lambda} \right) + \sigma(0) \frac{1}{s + E/\lambda} \quad (2.10)$$

Inverse Laplace transform of (4.4) and the expression of stress can be obtained as:

$$\sigma(t) = \lambda \dot{\varepsilon}_o \left(1 - e^{-\frac{E}{\lambda} t} \right) + \sigma(0) e^{-\frac{E}{\lambda} t} \quad (2.10)$$

Differentiating (2.11):

$$d\sigma(t) = \left[\lambda \dot{\varepsilon}_o - \sigma(0) \right] \frac{E}{\lambda} e^{-\frac{E}{\lambda} t} dt \quad (2.12)$$

Equation (2.12) can be used in numerical simulations. Please note that the stress at $t = \lambda/E$ (i.e. relaxation time) is expressed as:

$$\sigma(t) = \lambda \dot{\varepsilon}_o (1 - e^{-1}) + \sigma(0) e^{-1} \quad (2.13)$$

2.5.2 Kelvin-Voigt Element

Kelvin-Voigt element is also a two-component model consisting a linear spring and viscous dashpot in parallel. Kelvin element shows exponential creep and recovery but no exponential relaxation. The stress-strain relationship of Kelvin-Voigt element is given below. Figure 2.1 shows that the total stress is the sum of stresses from the dashpot and spring.

$$\sigma = E\varepsilon + \lambda\dot{\varepsilon} \quad (2.14)$$

For constant strain-rate tests, equation (2.14) becomes:

$$\sigma = E\dot{\varepsilon}_o H(t)t + \lambda\dot{\varepsilon}_o H(t) \quad (2.15)$$

or (take $t = t_+$)

$$\sigma(t_+) = \dot{\varepsilon}_o (Et + \lambda) \quad (2.16)$$

Therefore, the initial value of stress is:

$$\sigma(0_+) = \dot{\varepsilon}_o \lambda \quad (2.17)$$

and the stress at $t = \lambda/E$:

$$\sigma(t) = 2\dot{\varepsilon}_o \lambda \quad (2.18)$$

Differentiating equation (2.18) we get:

$$d\sigma(t) = \dot{\varepsilon}_o E dt \quad (2.19)$$

Please note that the stress increment is a constant during a constant strain-rate test.

The stress increment will be zero if it is a constant strain test (i.e. strain-rate is zero).

2.5.3 Burgers' Element

Burgers' element is a four-component model consisting of a Maxwell element and Kelvin

element in series. Burgers' element is capable of showing complicated behavior under constant stress tests: instant strain, exponential creep, instant recovery and delayed exponential recovery. Creep response of Burgers' element is the sum of the responses for Maxwell and Kelvin elements. Relaxation behavior of Burgers' element is complicated and hence makes it a powerful model to simulate the complicated linear viscoelastic phenomena. Detailed derivation of the equations for the above relationships can be found in Findley, et al. (1976). The stress-strain relationship of Burgers' element is given below.

$$\sigma + \left(\frac{\lambda_1}{E_1} + \frac{\lambda_1}{E_2} + \frac{\lambda_2}{E_2} \right) \dot{\sigma} + \frac{\lambda_1 \lambda_2}{E_1 E_2} \ddot{\sigma} = \lambda_1 \dot{\epsilon} + \frac{\lambda_1 \lambda_2}{E_2} \ddot{\epsilon} \quad (2.20)$$

For constant strain-rate tests, first order and second order differentiation of strain are:

$$\begin{aligned} \dot{\epsilon} &= \dot{\epsilon}_0 H(t) \\ \ddot{\epsilon} &= \dot{\epsilon}_0 \delta(t) \end{aligned}$$

where $\delta(t)$: Unit Impulse or Dirac Delta function (Dirac Delta function is the derivative of unit step function and it is highly singular).

Therefore, equation (2.20) can be re-written as:

$$\sigma + p_1 \dot{\sigma} + p_2 \ddot{\sigma} = q_1 \dot{\epsilon}_0 H(t) + q_2 \dot{\epsilon}_0 \delta(t) \quad (2.21)$$

where $p_1 = \frac{\lambda_1}{E_1} + \frac{\lambda_1}{E_2} + \frac{\lambda_2}{E_2}$

$$p_2 = \frac{\lambda_1 \lambda_2}{E_1 E_2}$$

$$q_1 = \lambda_1$$

$$q_2 = \frac{\lambda_1 \lambda_2}{E_2}$$

Take Laplace transform of equation (2.21) and we get:

$$\hat{\sigma}(s) + p_1(s\hat{\sigma}(s) - \sigma(0)) + p_2\left(s^2\hat{\sigma}(s) - s\sigma(0) - \frac{d\sigma(0)}{dt}\right) = q_1\dot{\varepsilon}_o \frac{1}{s} + q_2\dot{\varepsilon}_o \quad (2.22)$$

Solve for $\hat{\sigma}(s)$ and drop $d\sigma(0)/dt$ (since $\sigma(0)$ is a constant) in equation (2.22):

$$\hat{\sigma}(s) = [p_1\sigma(0) + q_2\dot{\varepsilon}_o] \frac{1}{1 + p_1s + p_2s^2} + p_2\sigma(0) \frac{s}{1 + p_1s + p_2s^2} + q_1\dot{\varepsilon}_o \frac{1}{s(1 + p_1s + p_2s^2)} \quad (2.23)$$

The denominator in the first right term can be simplified as:

$$\begin{aligned} 1 + p_1s + p_2s^2 &= p_2\left(s^2 + \frac{p_1}{p_2}s + \frac{1}{p_2}\right) \\ &= p_2\left[\left(s + \frac{p_1}{2p_2}\right)^2 - \left(\frac{p_1^2}{4p_2^2} - \frac{1}{p_2}\right)\right] \\ &= p_2\left[\left(s + \frac{p_1}{2p_2}\right)^2 - \left(\frac{\sqrt{p_1^2 - 4p_2}}{2p_2}\right)\right] \\ &= p_2\left(s + \frac{p_1 + A}{2p_2}\right)\left(s + \frac{p_1 - A}{2p_2}\right) \\ &= p_2(s + r_1)(s + r_2) \end{aligned} \quad (2.24)$$

$$A = \sqrt{p_1^2 - 4p_2}$$

where $r_1 = \frac{p_1 + A}{2p_2}$

$$r_2 = \frac{p_1 - A}{2p_2}$$

Thus, equation (2.23) becomes:

$$\hat{\sigma}(s) = \frac{[p_1\sigma(0) + q_2\dot{\varepsilon}_o]}{p_2} \frac{1}{(s + r_1)(s + r_2)} + \frac{p_1\sigma(0)}{p_2} \frac{s}{(s + r_1)(s + r_2)} + \frac{q_1\dot{\varepsilon}_o}{p_2} \frac{1}{s(s + r_1)(s + r_2)} \quad (2.25)$$

Taking partial fraction of the right third term in equation (2.25),

$$\frac{1}{s(s + r_1)(s + r_2)} = \frac{a}{s} + \frac{b}{s + r_1} + \frac{c}{s + r_2} \quad (2.26)$$

Solving for a, b, and c:

$$\frac{1}{s(s+r_1)(s+r_2)} = \frac{1}{r_1 r_2 s} + \frac{1}{r_1(r_1-r_2)(s+r_1)} - \frac{1}{r_2(r_1-r_2)(s+r_2)} \quad (2.27)$$

Therefore, equation (4.20) can be further simplified:

$$\begin{aligned} \hat{\sigma}(s) = & \frac{p_1 \sigma(0) + q_2 \dot{\varepsilon}_o}{p_2(r_2 - r_1)} \frac{(r_2 - r_1)}{(s+r_1)(s+r_2)} \\ & + \frac{p_2 \sigma(0)}{p_2(r_1 - r_2)} \frac{(r_1 - r_2)s}{(s+r_1)(s+r_2)} \\ & + \frac{q_1 \dot{\varepsilon}_o}{p_2} \left[\frac{1}{r_1 r_2} \frac{1}{s} + \frac{1}{r_1(r_1 - r_2)} \frac{1}{s+r_1} - \frac{1}{r_2(r_1 - r_2)} \frac{1}{s+r_2} \right] \end{aligned} \quad (2.28)$$

Taking inverse Laplace transform of equation (2.28), we get:

$$\begin{aligned} \sigma(t) = & \frac{p_1 \sigma(0) + q_2 \dot{\varepsilon}_o}{p_2(r_2 - r_1)} (e^{-r_1 t} - e^{-r_2 t}) \\ & + \frac{p_2 \sigma(0)}{p_2(r_1 - r_2)} (r_1 e^{-r_1 t} - r_2 e^{-r_2 t}) \\ & + \frac{q_1 \dot{\varepsilon}_o}{p_2} \left[\frac{1}{r_1 r_2} + \frac{1}{r_1(r_1 - r_2)} e^{-r_1 t} - \frac{1}{r_2(r_1 - r_2)} e^{-r_2 t} \right] \end{aligned} \quad (2.29)$$

or

$$\begin{aligned} \sigma(t) = & \frac{q_1 \dot{\varepsilon}_o}{p_2 r_1 r_2} + \left[\frac{\sigma(0)(p_2 r_1^2 - p_1 r_1) + \dot{\varepsilon}_o(q_1 - q_2 r_1)}{p_2 r_1(r_1 - r_2)} \right] e^{-r_1 t} \\ & + \left[\frac{\sigma(0)(p_1 r_2 - p_2 r_2^2) + \dot{\varepsilon}_o(q_2 r_2 - q_1)}{p_2 r_2(r_1 - r_2)} \right] e^{-r_2 t} \end{aligned} \quad (2.30)$$

Further simplification yields:

$$\sigma(t) = \alpha + \beta e^{-r_1 t} + \gamma e^{-r_2 t} \quad (2.31)$$

where $A = \sqrt{p_1^2 - 4p_2}$, $r_1 = \frac{p_1 + A}{2p_2}$, $r_2 = \frac{p_1 - A}{2p_2}$

$$\alpha = \frac{q_1 \dot{\epsilon}_o}{p_2 r_1 r_2}$$

$$\beta = \frac{\sigma(0)(p_2 r_1^2 - p_1 r_1) + \dot{\epsilon}_o(q_1 - q_2 r_1)}{p_2 r_1(r_1 - r_2)}$$

$$\gamma = \frac{\sigma(0)(p_1 r_2 - p_2 r_2^2) + \dot{\epsilon}_o(q_2 r_2 - q_1)}{p_2 r_2(r_1 - r_2)}$$

Differentiating equation (2.31) stress increment is obtained as:

$$d\sigma(t) = -\beta r_1 e^{-r_1 t} dt - \gamma r_2 e^{-r_2 t} dt \quad (2.32)$$

2.5.4 Simulations of Constant Strain-rate Tests

In order to check the behavior of each element under constant strain-rate, series of numerical calculations were made by assigning reasonable and constant values to the input parameters of each element. The numerical values of these parameters are listed in Table 2.1. The stress values are computed based on above derivations and are plotted in Figures 2.4, 2.5 and 2.6.

Table 2.1 Input Parameters for Constitutive Equations

Elements	E ₁ (Pa)*	E ₂ (Pa)*	λ ₁ (Pa-s)**	λ ₂ (Pa-s)**	T _{rx1} (sec) ^o	T _{rx2} (sec) ^o
Maxwell (1)	1E8	-	1E9	-	10	-
Maxwell (2)	1E8	-	1E10	-	100	-
Maxwell (3)	1E8	-	1E11	-	1000	-
Kelvin (1)	1E8	-	1E9	-	10	-
Kelvin (2)	1E8	-	1E10	-	100	-
Kelvin (3)	1E8	-	1E11	-	1000	-
Burgers' (1)	1E12	1E8	1E9	1E8	0.001	1
Burgers' (2)	1E12	1E8	1E10	1E8	0.01	1
Burgers' (3)	1E12	1E8	1E11	1E8	0.1	1

* modulus of linear spring.

** coefficient of viscosity.

^o relaxation time (T_{rx} = λ/E).

The strain rates at different stages during numerical calculations are:

- 0.1 % per second from 0 to 60 sec (loading),
- zero from 60 to 90 sec (rest period I or constant strain),
- 0.1% per second from 90 to 150 sec (un-loading),
- zero from 150 to 180 sec (rest period II of constant strain),
- 0.2 % per second from 180 to 200 sec (greater re-loading rate),
- 0.2 % per second from 200 to 220 sec (sudden un-loading),
- zero from 220 to 250 sec (rest period III or constant strain),
- 0.1% per second from 250 to 300 sec (unloading to tensile strain).

Three cases were considered for each element corresponding to the high (case 1), normal (case 2), and low temperatures (case 3). For the three cases increasing relaxation times (T_{rx}) were selected to represent high to low temperature values. The results for these cases were shown in Figures 2.4 to 2.6. Please note that the Burgers' element T_{rx2} values were kept constant as contribution from T_{rx2} values to final response was minimal.

At normal temperature, Maxwell element exhibited decreased stress rate with time (Figure 2.4). During the three rest periods, the relaxation rates also decreased with time. As seen in Figure 2.4a, Maxwell element showed viscous flow at high temperature and achieved a critical stress level. While in Figure 2.4c Maxwell element is approximately elastic at low temperatures, relaxation was not significant during the second and third rest periods.

Stress and strain were almost in phase for Kelvin element for all three temperatures without any relaxation (Figures 2.5). The Burgers' element (Figures 2.6) showed a

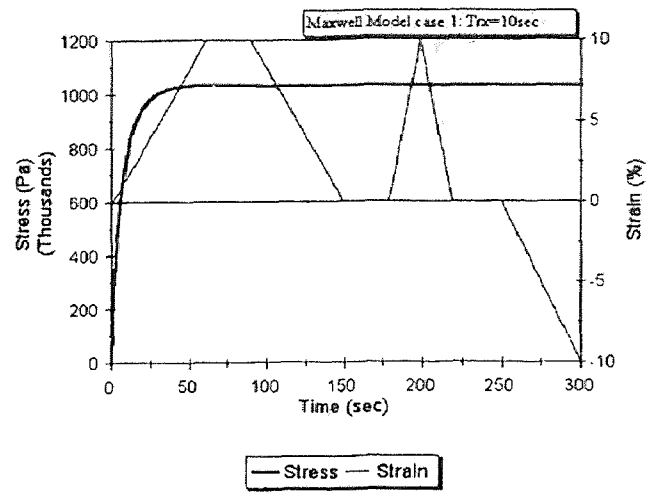
similar trend as that for Maxwell element except for lag times for stresses (especially at low temperature as seen in Figure 2.6c). Thus, Maxwell and Burgers' elements can exhibit typical rheological behavior of asphalt binder under constant strain-rate tests and Kelvin element can not describe relaxation. Therefore, Kelvin element should not be used to represent asphalt binder in any models of HMA.

2.6 Constitutive Laws for the Elements under Cyclic Loading

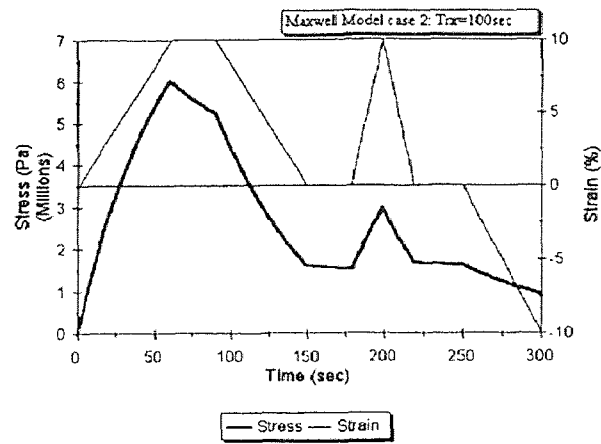
Complex modulus and phase angle for oscillating or sinusoidal loads can be calculated for the viscoelastic elements for the a range of loading frequencies. Complex modulus consists of the real part (storage modulus) and the imaginary part (loss modulus) at a given frequency. Phase angle is defined as the arc-tangent value of (loss modulus/storage modulus). The tangent value of phase angle is called the energy loss by viscous flow. Table 2.2 shows expressions of complex moduli and phase angles for the three viscoelastic elements considered in this research (Findley et al., 1976).

Table 2.2 Complex Moduli for Linear Viscoelastic Elements

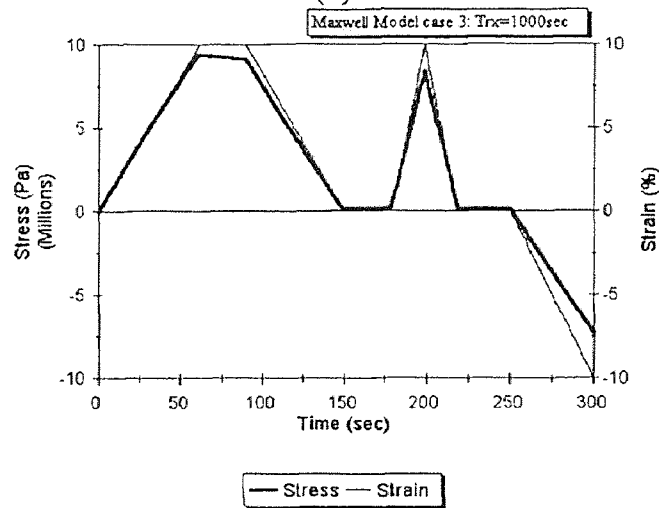
Elements	Complex Moduli or E^*	
	Real Part or E_r	Imaginary Part or E_i
Maxwell	$\frac{\lambda^2 \omega^2 / K}{1 + \lambda^2 \omega^2 / K^2}$	$\frac{\lambda \omega}{1 + \lambda^2 \omega^2 / K^2}$
Kelvin	K	$\lambda \omega$
Burgers'	$\frac{p_1 q_1 \omega^2 - q_2 \omega^2 (1 - p_2 \omega^2)}{p_1^2 \omega^2 + (1 - p_2 \omega^2)^2}$	$\frac{[p_1 q_1 \omega^2 + q_1 (1 - p_2 \omega^2)] \omega}{p_1^2 \omega^2 + (1 - p_2 \omega^2)^2}$



(a)

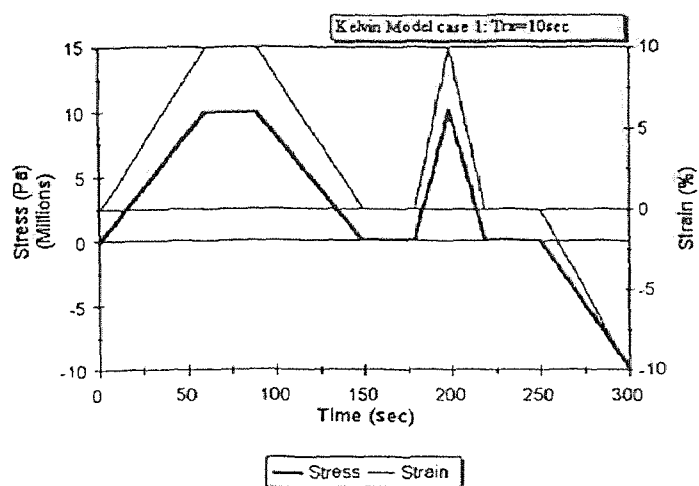


(b)

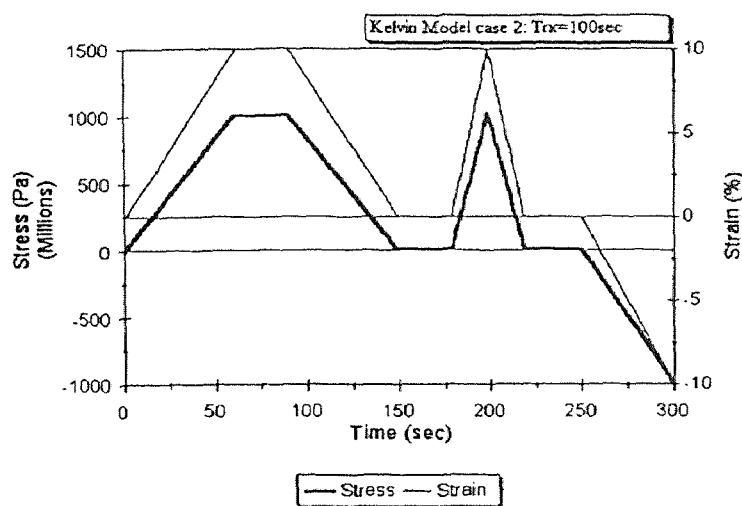


(c)

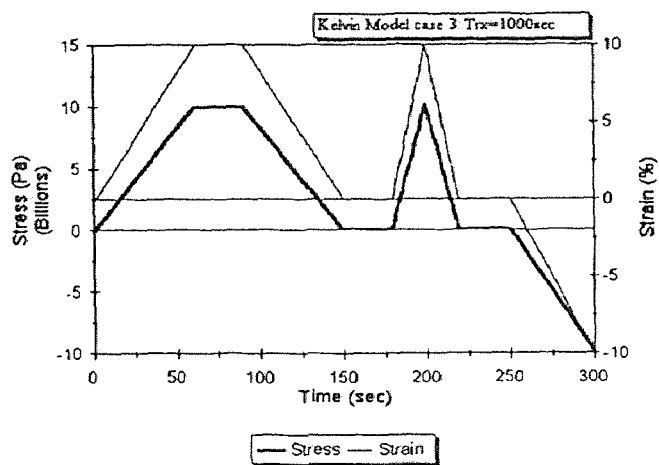
Figure 2.4 Response of Maxwell Element



(a)

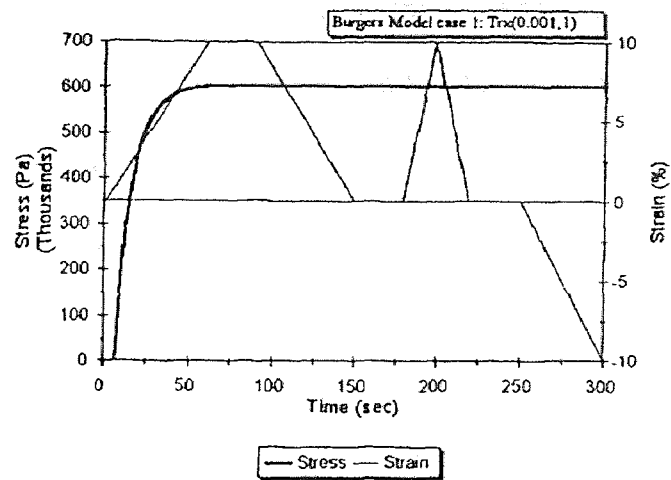


(b)

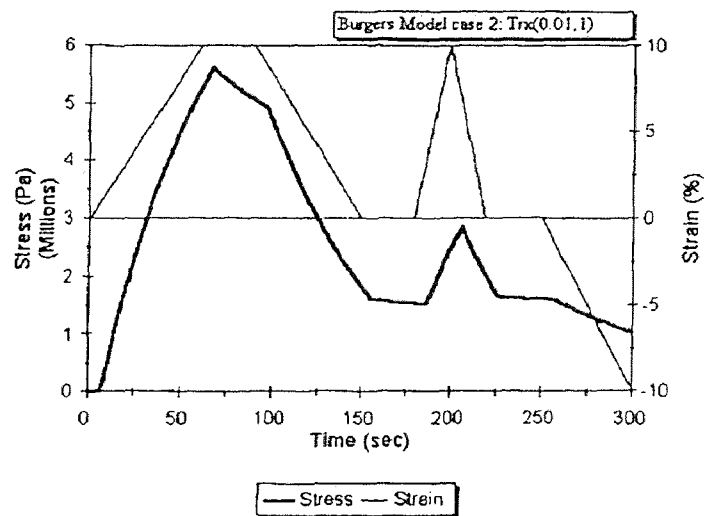


(c)

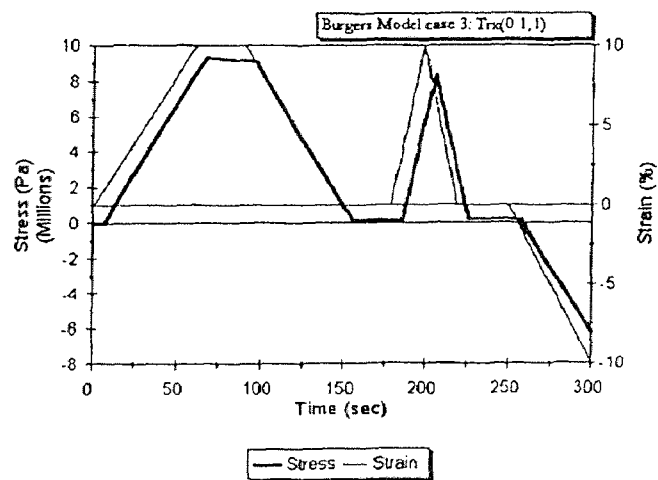
Figure 2.5 Response of Kelvin-Voigt Element



(a)



(b)



(c)

Figure 2.6 Response of Burgers' Element

The “Master Curve” that is used to characterize asphalt binder can be constructed by performing oscillating tests (such as: *SHRP*’s Dynamic Rheometer test) for a wide range of loading frequencies at different temperatures. The resulting complex moduli and phase angles (versus temperatures) can be shifted horizontally to the right or the left of the reference temperature (such as: glass transition temperature) by multiplying suitable shift factors (e.g. obtained from the William-Landel-Ferry equation based on time-temperature superposition theory). Therefore, the curves at different temperatures form a single continuous curve, “Master Curve”, covering the behavior of asphalt binder over a wide range of loading frequencies or temperatures. Figure 2.7 shows a master curve, the laboratory test data from Christensen and Anderson (1992) for a *SHRP* core asphalt binder, AAB-1 (tank). The “core” asphalt binders are those used in *SHRP* research program that include various asphalt types. “Tank” asphalt is the un-aged or fresh asphalt without aging.

Table 2.3 shows the input parameters for the three elements. Those input parameters were used to calculate the theoretical complex moduli for a given frequency for all three elements.

Table 2.3 Parameters for Calculating the Complex Moduli

Elements	E_1 (Pa)	E_2 (Pa)	λ_1 (Pa-s)	λ_2 (Pa-s)	$T_{\alpha 1}$ (sec)	$T_{\alpha 2}$ (sec)
Maxwell	1E9	-	1E7	-	0.01	-
Kelvin	1E8	-	1E6	-	0.01	-
Burgers’	1E9	1E5	1E7	1E5	0.01	1

Figures 2.8, 2.9 and 2.10 show the calculated complex moduli for linear viscoelastic elements: Maxwell, Kelvin, and Burgers' respectively. By comparing the above figures, it can be clearly seen that Maxwell and Burgers' elements are capable of describing trends of the asphalt binder reasonably well. However, Burgers' element can match the values of complex modulus and phase angle values within the working frequency range. The input parameters for Maxwell and Burgers' elements can be back-calculated by fitting the frequency sweep test data. These back-calculated material parameters, then, can be used in micromechanical analysis to model the asphalt binder in a composite system of *HMA*. The material formulation in this chapter will be included in the next chapter to develop the DEM model for HMA.

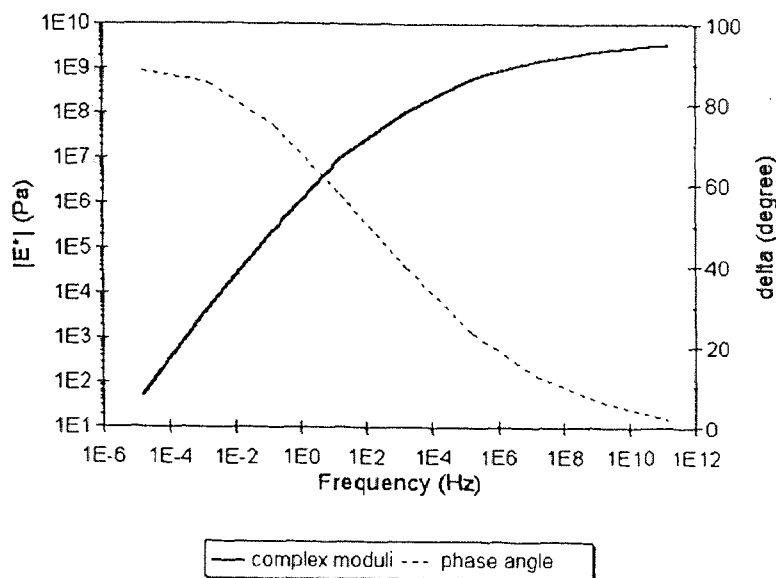


Figure 2.7 Laboratory Test data for Asphalt Binder
(Christensen and Anderson, 1992)

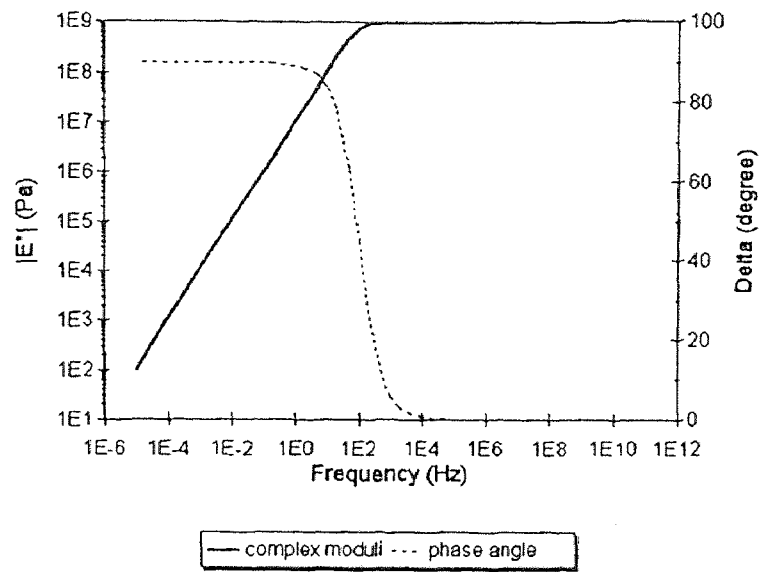


Figure 2.8 Complex Moduli of Maxwell Element

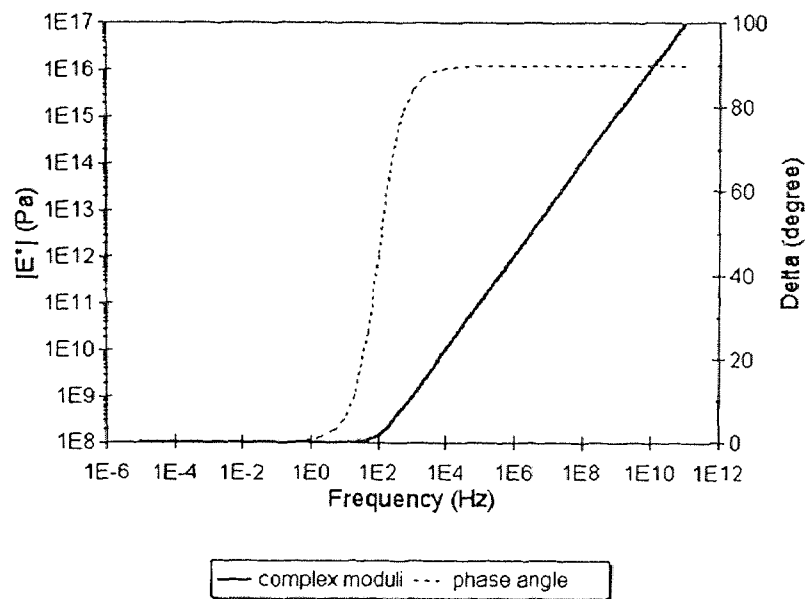


Figure 2.9 Complex Moduli of Kelvin-Voigt Element

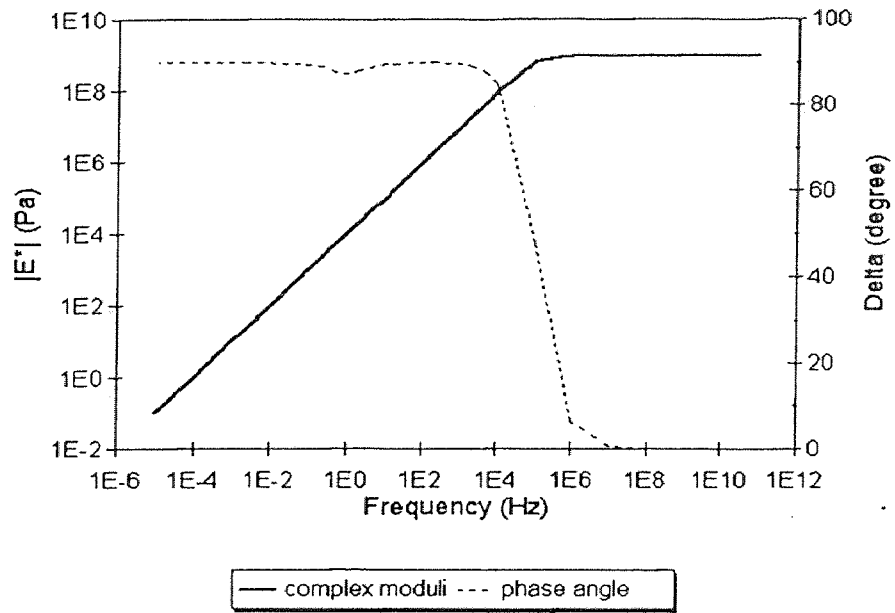


Figure 2.10 Complex Moduli of Burgers' Element

CHAPTER 3

NUMERICAL SIMULATION - ISOTHERMAL CASES

3.1 Introduction

3.1.1 Viscoelastic Behavior and Discrete Characteristics of Hot Mixed Asphalt

In Chapter 2 of Micromechanics of Hot Mix Asphalt, the author described the material formulation of components in *HMA*. This chapter describes the development of a model based on a discrete element method (*DEM*) to simulate *HMA*. Discrete element method, among microscopic models, reconstructs the materials with certain internal structure and specific geometry. Discrete element method forms a bridge between the microscopic variables and macroscopic responses. The reconstructed geometric structure can simulate the continuum stress and strain of a material by capturing the potential fields of particle dynamics.

3.2 Discrete Element Methods

DEM was applied to number of problems, such as: failure analysis of materials, mechanical behavior of granular media, mechanical modeling of fractured and jointed systems, fluids and granular material flow, fracture networks, and the development of macroscopic constitutive laws from discrete microscopic models.

Discrete Element Models can be used to model dynamic or quasi-static systems. The granular flow problems are truly dynamic where time-dependent particle motions are of interest. Modeling of asphalt concrete can be considered as quasi-static problems. The individual particles (or blocks) were modeled as rigid or deformable. In 2-D case,

circular, elliptical and polygonal shapes of particles may be used. In 3-D case, spherical, ellipsoidal, or polyhedral solids may be used. The deformable solid particles were modeled using finite difference or finite element methods.

Equation of motion for each particle is expressed as:

$$M\ddot{x} + D\dot{x} + R(x) = F \quad (3.1)$$

where \ddot{x}, \dot{x}, x : linear acceleration, velocity, and displacement vectors respectively;

M : mass;

D : damping;

R : internal restoring force;

F : external force.

For a slow variation of the stresses with time, the system can be treated as quasi-static and the inertia terms may be dropped. The restoring forces and contact forces for all the particles can be summed up to obtain the macroscopic stresses of the assemblies.

3.3 A Model based on A Discrete Element Method for *HMA*

3.3.1 Adaptation of TRUBAL Program to Model HMA

The microscopic model, *TRUBAL (version 1.51)*, was selected because of the following reasons (Cundall, 1989):

1. It meets the two criteria of *DEM* definition that allows finite displacements and rotations of discrete bodies and recognizes new contacts automatically;
2. It uses an explicit, time-marching method to solve the equations of motion directly and uses the deformable bodies and soft contacts.

The modified *TRUBAL* program (termed “ASBAL” as it models Aphalt concrete using a modified truBAL program) included the pore-springs and dashpots to include the second phase, asphalt cement. The asphalt binder between coated particles was represented by a set of Burgers’ elements to consider viscoelasticity of asphalt cement. Aggregate particles are assumed as elastic.

3.3.2 Material Models of Asphalt Binder and Aggregates

Material models used in ASBAL programs are: (a) viscoelastic element for asphalt binder; and (b) linear or nonlinear spring for aggregates.

Aggregates can be represented by either Hookean spring or Hertz-Mindlin contacts (non-linear elastic). In *ASBAL*, Hookean springs were used to represent aggregate contacts.

Burgers’ element was selected (see Chapter 2: Material Formulation) as the proper viscoelastic element for asphalt binder. Burgers’ element can simulate instantaneous strain, viscoelastic response, instantaneous recovery, and permanent strain under constant stress tests of asphalt binders (see Figure 3.1). The stress-strain relationship for Burgers’ element for constant strain-rate tests (the displacements in normal and tangential directions are represented by n and s respectively) is expressed as:

$$\sigma + p_1 \dot{\sigma} + p_2 \ddot{\sigma} = q_1 \dot{\epsilon}_0 H(t) + q_2 \dot{\epsilon}_0 \delta(t) \quad (3.2)$$

$$\text{where } p_1 = \frac{\lambda_1}{E_1} + \frac{\lambda_1}{E_2} + \frac{\lambda_2}{E_2}, \quad p_2 = \frac{\lambda_1 \lambda_2}{E_1 E_2}$$

$$q_1 = \lambda_1, \quad q_2 = \frac{\lambda_1 \lambda_2}{E_2}$$

$H(t)$: Step function.

$\delta(t)$: Unit Impulse or Dirac Delta function

E_i : modulus of springs in Burgers' element ($i: 1,2$),

λ_i : viscosity of dashpots in Burgers' element ($i: 1,2$).

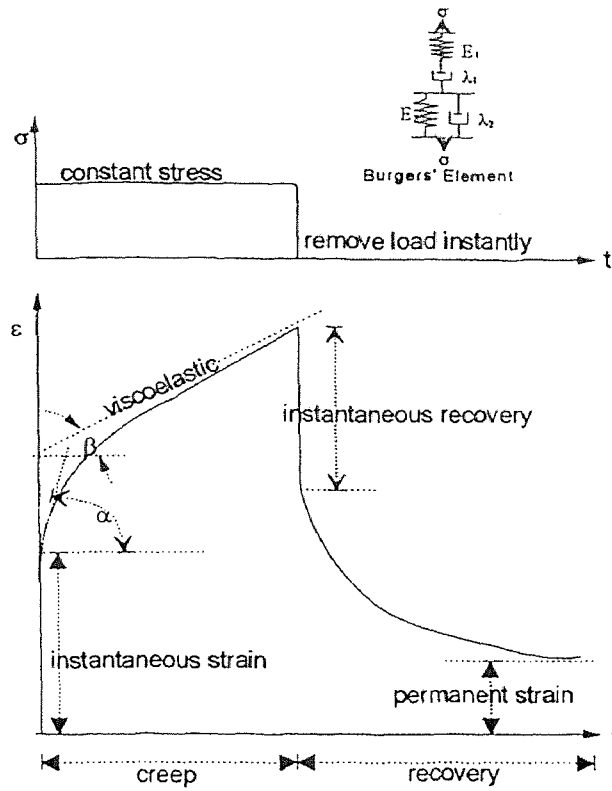


Figure 3.1 Basic Response of Burgers' Element

By applying Laplace Transform and rearranging the terms of equation (3.2) we get:

$$\sigma(t) = \alpha + \beta e^{-\tau_1 t} + \gamma e^{-\tau_2 t} \quad (3.3)$$

where:

$$A = \sqrt{p_1^2 - 4p_2}, \quad r_1 = \frac{p_1 + A}{2p_2}, \quad r_2 = \frac{p_1 - A}{2p_2}$$

$$\alpha = \frac{q_1 \dot{\epsilon}_o}{p_2 r_1 r_2}$$

$$\beta = \frac{\sigma(0)(p_2 r_1^2 - p_1 r_1) + \dot{\epsilon}_o(q_1 - q_2 r_1)}{p_2 r_1(r_1 - r_2)}$$

$$\gamma = \frac{\sigma(0)(p_1 r_2 - p_2 r_2^2) + \dot{\epsilon}_o(q_2 r_2 - q_1)}{p_2 r_2(r_1 - r_2)}$$

Differentiating the above equation, the stress increment was obtained as:

$$d\sigma(t) = -\beta r_1 e^{-r_1 t} dt - \gamma r_2 e^{-r_2 t} dt \quad (3.4)$$

3.3.3 Contacts

Figure 3.2 shows how the contacts are formed and broken as particles move relative to each other. In this modeling effort two types of contacts are used: Type I contacts and Type II contacts. Type I contacts include particle contacts and particle contacts with asphalt binder. Type II contacts consider only the particle contacts through asphalt cement in between.

Type I Contacts

Type I contacts or compound contacts occur when aggregates are in contact. At this stage, the linear springs are activated to account for particle contacts and the Burgers' elements are activated to account for asphalt coating. This is applicable to both normal

and tangential directions. The Mohr-Coulomb friction law was used to calculate limiting resisting forces that prevent particle rotations. The friction force is a compounded item containing both particle-particle and asphalt-particle frictions. The granular particle-particle contact cohesion is zero. The cohesion of asphalt layer is assumed as the adhesion between asphalt and aggregates where cohesion is a constant. The coefficient of internal friction of viscoelastic asphalt is zero and that of granular aggregate is assumed between 1 and 0.7.

Type II Contacts

Type II contacts or particle-asphalt-particle contacts occur when particles are not in contact but the distance between them is less than L_{min} (L_{min} is two times of asphalt thickness). Type II contacts produce no contribution to particle contacts. Burgers' elements are activated to model asphalt binder for this contact type. The limiting resisting forces that prevent particle rotation will be from the adhesion between particle and asphalt cement.

3.3.4 Computation Procedure in ASBAL

There are six major routines in ASBAL program. The flow chart is shown in Figure 3.3.

1. *Assembly generation (GEN routine)*

Randomly generates aggregates in a periodic space. Asphalt binder is included.

2. *Cycle calculation (CYCLE routine)*

Cycle through *MOTION*, *CONTACT*, *ASFORD* routines under a servo control mode.

3. Aggregate motion (*MOTION* routine)

Calculates motions of asphalt-coated aggregates based on Newton's Second Law.

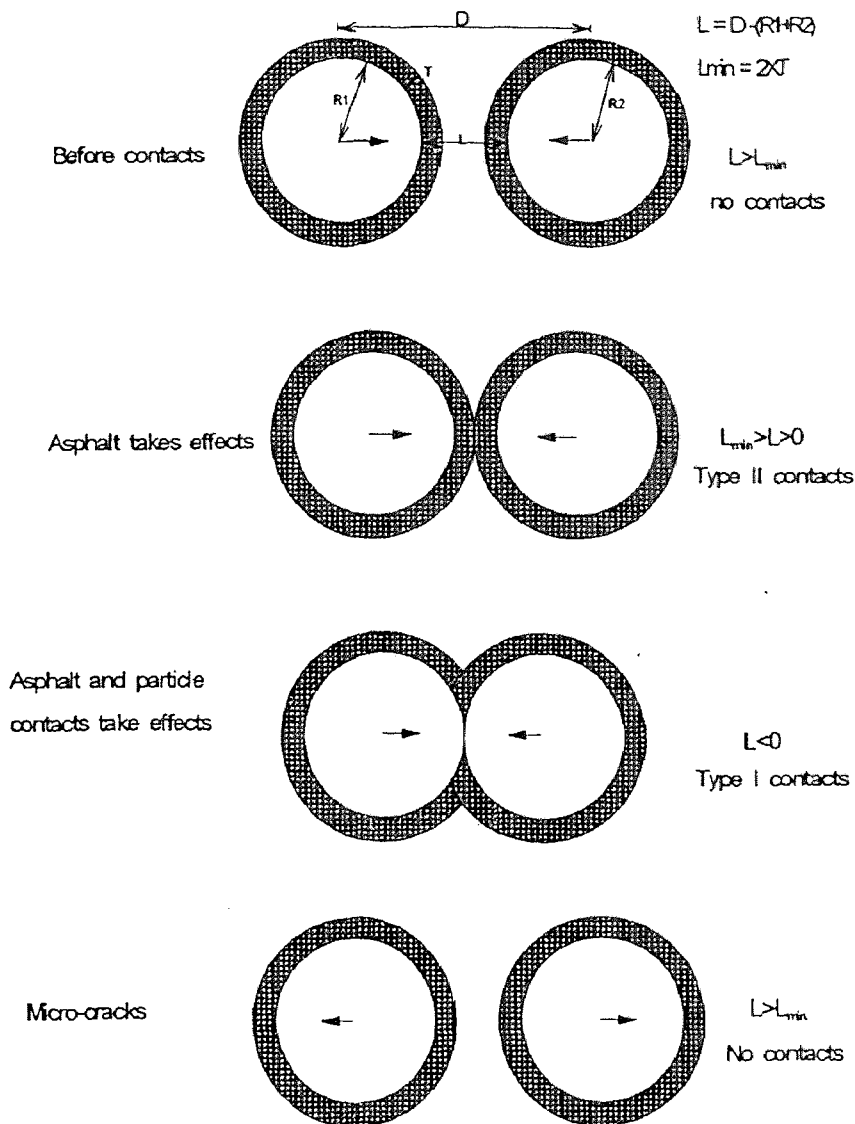


Figure 3.2 Contact Classification

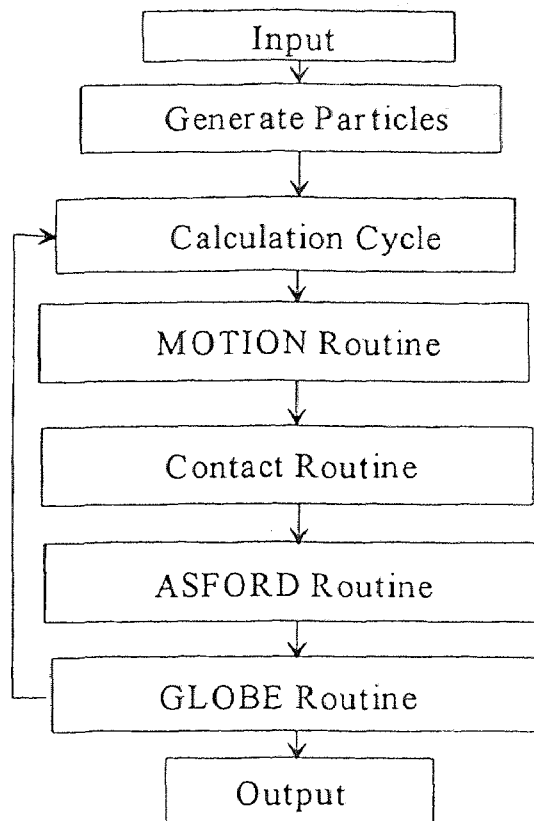


Figure 3.3 Flowchart of ASBAL Program

4. *Detection and update of contact (CONTACT routine, that includes REBOX, SEARCH, BBTEST, and UPDATE routines)*

Checks the contacts within each “box” of the periodic space and update contacts.

5. *Force-displacement calculation (ASFORD routine)*

Apply material models to calculate the contacts forces and moments based on the calculated stress tensors.

6. *Summation of particle stresses to compute global stresses (GLOBE routine)*

Vectorially add all the particle forces in the three global stress directions to compute the macroscopic stress tensor.

3.3.5 Force-Displacement Laws and Separation Criteria for Particles in *ASFORD* Subroutine

The following calculations are performed in subroutine *ASFORD*. Figure 3.4 shows two spheres centered at positions x_i and y_i have radii R_x and R_y respectively, where $x_i = (x_1, x_2, x_3)$ and $y_i = (y_1, y_2, y_3)$. The translational and angular velocities of center of mass for sphere X are \dot{x} and $\dot{\theta}_x$; for sphere Y are \dot{y} and $\dot{\theta}_y$. If counterclockwise the angular velocity is positive. Two components of unit vectors, e_i and t_i ($i = 1, 2, 3$) are introduced normal and tangential to the vector from position x to y . D can be defined as the distance between the centers of two spheres and e_i can be obtained by:

$$e_i = \frac{y_i - x_i}{D} \quad (3.5)$$

where subscript i represents that for specific calculation cycle.

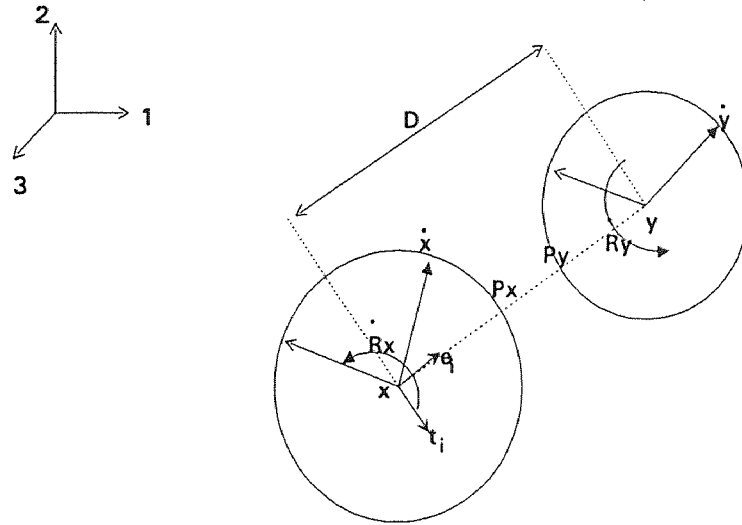


Figure 3.4 Diagram of Coordinate System in DEM

The unit vector, t_i , can be obtained by rotating e_i clockwise by 90° . Consider the two points P_x and P_y that are generated by intersecting the surfaces of spheres x and y by the line \overline{xy} . Therefore, the relative velocity of P_y with respect to P_x is:

$$\dot{\mathbf{X}} = (\dot{x}_i - \dot{y}_i) - (\dot{\theta}_x R_x - \dot{\theta}_y R_y) t_i \quad (3.6)$$

\dot{n} and \dot{s} are respectively the normal and tangential components of relative velocity along e_i and t_i :

$$\begin{aligned} \dot{n} &= \dot{\mathbf{X}} e_i = (\dot{x}_i - \dot{y}_i) e_i \\ \dot{s} &= \dot{\mathbf{X}} t_i = (\dot{x}_i - \dot{y}_i) t_i - (\dot{\theta}_x R_x + \dot{\theta}_y R_y) \end{aligned} \quad (3.7)$$

The respective displacements in both normal (Δn) and tangential (Δs) directions after time interval (Δt) are:

$$\begin{aligned} \Delta n &= \dot{n} \Delta t = (\dot{x}_i - \dot{y}_i) e_i \Delta t \\ \Delta s &= \dot{s} \Delta t = \left\{ (\dot{x}_i - \dot{y}_i) t_i - (\dot{\theta}_x R_x + \dot{\theta}_y R_y) \right\} \Delta t \end{aligned} \quad (3.8)$$

The force displacement laws are then applied to the following three possible cases to compute the incremental particle forces of the aggregates based on the relative motions.

The distance between points P_x and P_y (see Figure 3.4) is defined as $L = D - (R_x + R_y)$. The minimum distance for asphalt to get in effect is L_{min} , which is twice of thickness of asphalt binder.

(I) Case a: $L > L_{min}$ or No Contact

There is no contribution from asphalt cement nor from aggregate. Calculation of interaction forces is skipped during this time interval.

(ii) Case b: $L_{min} > L > 0$ (Type II contacts)

There is a contribution from asphalt cement contacts but not from aggregate-aggregate contacts. The Burgers' elements are activated to calculate the incremental particle force after each time step (a session of constant speed displacement) in normal (ΔF_n) and tangential (ΔF_s) directions:

$$\Delta F_n = \left(\alpha + \beta e^{-\eta_1 t} + \gamma e^{-\eta_2 t} \right)_{d=n} \times A_{ct} \quad (3.9)$$

$$\Delta F_s = \left(\alpha + \beta e^{-\eta_1 t} + \gamma e^{-\eta_2 t} \right)_{d=s} \times A_{ct} \quad (3.10)$$

where A_{ct} : the particle-asphalt-particle contact area (see Appendix A):

$$A_{ct} = \pi \frac{\left(\frac{L_{min}}{2} \right)^4 + 8(r_1 + r_2) \left(\frac{L_{min}}{2} \right)^3 + 4(r_1^2 + r_2^2 + 5r_1 r_2) \left(\frac{L_{min}}{2} \right)^2 + 8r_1 r_2 (r_1 + r_2) \left(\frac{L_{min}}{2} \right)}{4 \left(r_1 + r_2 + \frac{L_{min}}{2} \right)^2}$$

r_1 and r_2 are radii of particles 1 and 2 respectively,

subscript (n or s): denotes normal or shear force at the contact.

The maximum shear force, $(F_s)_{max}$, was obtained from Mohr-Coulomb failure criteria:

$$(F_s)_{max} = F_n \tan \phi_\mu^A + C^A A_{ct} = F_n \mu^A + C^A A_{ct} \quad (3.11)$$

where ϕ_μ^A : the friction angle of asphalt cement contacts;

C^A : the cohesion of asphalt cement;

μ^A : the coefficient of friction at asphalt cement contacts.

If the computed shear force is greater than the maximum shear force, the shear force will be adjusted by multiplying it by a factor described in Chapter 2.

(iii) Case c: $L < 0$ (Type I contacts)

The aggregate-aggregate contacts occur and the combined effects of asphalt cement and the aggregates in contact have contributed to the contact force. The contact forces are:

$$\Delta F_n = k_n^p \Delta n + \left(\alpha + \beta e^{-\tau_1} + \gamma e^{-\tau_2} \right)_{d=n} \times A_{ct} \quad (3.12)$$

$$\Delta F_s = k_s^p \Delta s + \left(\alpha + \beta e^{-\tau_1} + \gamma e^{-\tau_2} \right)_{d=s} \times A_{ct} \quad (3.13)$$

where k_n^p and k_s^p are the normal and shear stiffnesses of aggregates.

The maximum shear force, $(F_s)_{max}$, is defined as:

$$(F_s)_{max} = F_n \tan \phi_\mu^p + C^p A_{ct}' + F_n \tan \phi_\mu^A + C^A A_{ct} = F_n \mu^p + C^p A_{ct}' + F_n \mu^A + C^A A_{ct} \quad (3.14)$$

where ϕ_μ^p : the smaller value of the inter-particle friction angles;

C^p : the smaller cohesion of aggregates (usually assumed to be zero);

μ^p : the smaller coefficient of friction of aggregates;

A_{ct}' : particle-particle or dry contact area (see Appendix A):

$$A_{ct}' = \pi \frac{2(r_1^2 + r_2^2)D^2 - D^4 - (r_1^2 - r_2^2)^2}{4D^2}$$

where D is the distance between centroids of two particles.

The adjustment of shear force at failure plane is performed in the same manner as in the earlier case.

The incremental forces (ΔF_s and ΔF_n), computed from one of the above three cases are for a given contact in local directions. These incremental forces will be resolved into components in the global directions of 1, 2, and 3. The sum of these forces acting on sphere A results in $\sum F_{A(1)}$, $\sum F_{A(2)}$, and $\sum F_{A(3)}$. The sum of resultant moment acting

sphere A is $\sum M_{(A)} = \sum F_S R_A$. The resultant forces and moment will be used as input to the subroutine *MOTION* to calculate the new translational and angular accelerations. The calculation cycles will continue until it reach a specified number of cycles.

3.3.6 Simulation of Mechanical Behavior of HMA

There are three major steps in simulation of mechanical behavior of HMA:

1. Generation of aggregate particles and asphalt;
2. Compaction of the specimen;
3. Testing of specimen.

Generation of Aggregates and asphalt: A specified number of aggregate particle with different sizes is randomly generated within a periodic space. Properties of aggregates and asphalt (including the thickness of asphalt coating) are assigned. No gravitational force is specified. Since this is a loose packing, no aggregate-aggregate contacts are expected. Meegoda and Chang (1993) generated a NJ I-6 mix for subsequent testing using three sizes.

Compaction of the specimen: The generated HMA specimen is compacted by applying a given strain-rate at the boundaries of periodic space. The compaction can be either isotropic or anisotropic. At the end of compaction, the loose packing will become a densely packed specimen where many asphalt-coated particles are in contacts. The

compaction is continued until a given *VMA* (voids in mineral asphalt) value and residual stress values are reached.

Testing of Specimen: The compacted specimen is ready to be tested. The ASBAL program can simulate either strain or stress controlled tests, but all the tests in this research are strain-controlled. Uniaxial tests (with or without confining pressures), biaxial tests, triaxial tests, and simple shear tests can be simulated. Cyclic loading can be also simulated. Loading rates for cyclic tests are restricted to maintain quasi-static condition. Output data include: detailed status of particle assemblies after a specified calculation cycle; and graphic snapshots of this specimen.

3.4 Numerical Simulation of *HMA* using the *ASBAL* Program

For the numerical simulations two different particle packings were used. The first was an assembly of 150 particles with 100 particles having 10 mm diameter and 50 particles with 15 mm diameter. For this simulation, an initial size of periodic space was a $200 \times 200 \times 200$ mm³ cube. The periodic space was further divided into 27 identical cubical boxes (i.e. $66.67 \times 66.67 \times 66.67$ mm³) to enhance the numerical efficiency and, to facilitate contacts detection and update. 150 particles of two sizes were generated randomly in a periodic space. Micro-parameters (such as particle motions, coordination numbers, and sliding, etc.) were recorded at different stages during the simulation (including pre-failure and post-failure stages) and sensitivity tests were performed. The latter simulation of a laboratory test (Lee and Dass, 1993) was used to validate the ASBAL program. For this

simulation with 512 particles, an initial periodic space of size $50 \times 50 \times 100 \text{ mm}^3$ was used. This periodic space was further divided into 16 equivalent boxes with a dimension of $25 \times 25 \times 25 \text{ mm}^3$. Five hundred and twelve particles of one size (6 mm in diameter) were generated randomly inside the periodic space.

Lee and Dass (1993) (see Appendix E) used a relatively large assembly (3,650 borosilicate glass beads with a size of 6 mm) to eliminate boundary effects and to obtain more representative data. The specific gravity of glass beads was 2.23 and that of the asphalt binder (AC-30) was 1.03. The sample had a dimension of 76.2 mm (3 inch) in diameter and 146 mm (5.75 inch) in height. By weight, the sample contained 92% (920.5 g) glass beads and 8% (77.7 g) asphalt. By volume, the sample contained 60% glass beads (VMA, 40%). The asphalt binder thicknesses ranged from 0.0 to 0.4 mm with a peak occurrence at 0.2 mm (from X-ray tomography).

3.4.1 Input Parameters

The microscopic parameters that represent fundamental physical properties were assigned to a *DEM*. However, some input parameters were estimated due to lack of laboratory test data. Input data consisted of the following:-

1. Properties of aggregate particles
2. Properties of asphalt binder
3. Initial condition
4. Loading path

3.4.1.1 Properties of Aggregates Particles

The normal stiffness of particle was estimated as 2×10^8 Pa-mm (Ting, 1989, stated that the normal elastic stiffness for granite cylinders ranged from 10^8 to 10^{10} Pa-mm). The shear stiffness of particles was assumed as 1×10^8 Pa-mm (Mindlin, 1949, stated that the ratio of shear modulus to normal stiffnesses ranged from 1/2 and 1 for elastic bodies in contact with elliptical contact areas). Density for the particles was assumed as 1.00 g/cm^3 . There is no local cohesion at particle-particle contacts (i.e. cohesionless). Coefficient of friction between aggregates was assumed as 1 (i.e. the angle of local friction is 45°) to simulate particle-particle interlock.

For glass beads, a normal stiffness of 2.5×10^8 Pa-mm and a shear stiffnesses of 1.25×10^8 Pa-mm were used. The density of glass beads was 2.23 g/cm^3 . Local coefficient of friction for glass beads ranged from 0.577 to 1 (i.e. internal friction angle is from 30° to 45°). Hence used a local coefficient of friction of 0.7 (i.e. internal friction angle of 35°). Local cohesion parameter of glass beads was assumed to be zero.

3.4.1.2 Properties of Asphalt Cement

For the 150-particle simulation, the input parameters for Burgers' element were estimated ($K_{1n}=2 \times 10^6$ Pa, $\lambda_{1n}=2 \times 10^5$ Pa-s, $K_{2n}=2 \times 10^4$ Pa, $\lambda_{2n}=2 \times 10^2$ Pa-s, $K_{1s}=2 \times 10^6$ Pa, $\lambda_{1s}=2 \times 10^5$ Pa-s, $K_{2s}=2 \times 10^4$ Pa, $\lambda_{2s}=2 \times 10^2$ Pa-s) to simulate a certain type of asphalt binder. The friction coefficient for asphalt-asphalt contacts was assumed as zero while the cohesion for asphalt cement was assumed as 1×10^5 Pa. There was limited information on the physical properties of aggregate-binder interface. However, the SHRP research

(Huang, 1993) suggested that the failure of aggregate-binder bonding is governed by cohesion failure (failure in asphalt binder) instead of adhesion failure (failure at aggregate-binder boundary). Peltonen (1992) showed that the adhesion of bitumen onto the hydrophilic silicate but showed no correlation to physical properties. The thickness of asphalt binder, L_{\min} was assumed to be 0.4 mm (i.e. asphalt binder thickness was 0.2 mm).

For the 512-particle simulation with AC-30 asphalt cement, input parameters for Burgers' elements were back-calculated from the master curve ($K_{1n}=2 \times 10^9$ Pa, $\lambda_{1n}=2 \times 10^7$ Pa-s, $K_{2n}=2 \times 10^5$ Pa, $\lambda_{2n}=2 \times 10^5$ Pa-s, $K_{1s}=2 \times 10^9$ Pa, $\lambda_{1s}=2 \times 10^7$ Pa-s, $K_{2s}=2 \times 10^5$ Pa, $\lambda_{2s}=2 \times 10^5$ Pa-s). The master curve for this asphalt binder was given in Chapter 2. The master curve describes the complex modulus and loss tangent of the asphalt binder (based on Boltzmann Superposition theorem) for a given range of loading frequencies or temperatures. The local cohesion of asphalt binder (AC-30) was estimated as 1×10^5 Pa based on laboratory tests. The maximum shear strength of AC-30 was 1×10^5 Pa. X-ray Tomography measurement for the laboratory tests (Lee and Dass, 1993) showed asphalt binder thickness of 0.2 mm. Hence, L_{\min} was assumed to be equal to 0.4 mm.

3.4.1.3 Initial Conditions for the Tests

150-particle simulation: Once the specimen was generated, the cubic space (i.e. the sample mixture) was compacted at isotropic strain-rates (ranging from 0.02 to 0.005 % per second). After 5000 calculation cycles, the compaction was completed and the sample was reduced to a size of 118.78 mm \times 118.78 mm \times 118.78 mm. The VMA value at this

stage was 33%. The overlap rate was allowed to vary within a small range (e.g. overlap rate was under 0.1 %).

512-particle simulation: The specimen was compacted by isotropic strain rates until it was approximately 35 mm × 35 mm × 76 mm (similar shape as that of the laboratory specimen of Lee and Dass, 1993). At the end of compaction it had a VMA value of 38%.

3.4.1.4 Loading Paths

The constant strain-rate tests were simulated in this research. For the 150-particle simulation, constant P (average principal stress) tests were performed. The theoretical time step was calculated from $2\sqrt{m_{\min} / k_n}$, where m_{\min} is the minimum mass of the particles and k_n is the normal stiffness of particle spring. The time-step was 0.05 times (or 1/20) of the theoretical time-step to achieve numerical stability. Thus, the time-step for one calculation cycle was 1.4472×10^{-2} seconds.

For the 512-particle tests, global principal strain-rates were specified to match the volumetric strains of laboratory tests. The time-step was 3.1762×10^{-3} seconds.

Global damping coefficient for both simulations was assumed to be 0.5 at 0.25 Hz as suggested by Cundall (1988). These values were determined through several simulations to maintain the numerical stability.

3.5 Results

3.5.1 150-particle Simulation

Macroscopic Behavior

The stress-strain curve for the 150-particle simulation is shown in Figure 3.5. Stages 1 to 3 are pre-failure stages and Stages 4 and 5 are post-failure stages. Maximum deviatoric stress occurred between Stages 3 and 4. The variation of volumetric strain with axial strain is shown in Figure 3.6. The specimen dilated as observed in the HMA laboratory tests.

Microscopic Parameter

The plot of VMA and coordination number with axial strain (see Figure 3.7) shows that VMA increased from 33.0 % to 35.7 % while coordination number decreased from 7.3 to 5.75 with a “cross-over” deviatoric strain of about 5.5%. The plot of number of contacts with axial strain (see Figure 3.8) shows that asphalt contacts (Type I contacts) increased until 3 % deviatoric strain then decreased while fluctuating until the sample failed. The total number of contacts decreased as observed in changes of coordination number. From the above graphs one can conclude that the “strength” of a HMA sample is solely governed by the number of contacts.

Important information about the simulation for the five stages of 150-particle simulation are shown in Table 3.1. Graphical snapshots of the sample were taken during the simulation with the view point set at the Z-direction for visualization. The compacted HMA assembly shown in Figure 3.9 is a two-dimensional representation of a three-

Table 3.1 Micro-parameters at Different Stages of Simulation
(150-particle simulation)

Simulation Stages	1	2	3	4	5
Calculation Cycle	5,000	8,000	11,000	13,000	18,400
Max. Relative Displacement (mm/200 cycles)	0.3425	0.1328	0.5438	0.4928	0.8363
Max. Incremental Rotation (degree/200 cycles)	1.926	2.416	3.21	2.506	3.691
VMA	0.335	0.337	0.343	0.345	0.391
Coordination number	6.987	6.627	6.28	6.00	5.747
Principal stress (Z- direction) (kPa)	207	325	365	362	354
Sliding	0.021	0.062	0.100	0.109	0.118
Deviatoric stress (kPa)	1.8	179	248	242	234
Deviatoric strain (%)	0	2.89	5.79	7.72	12.92

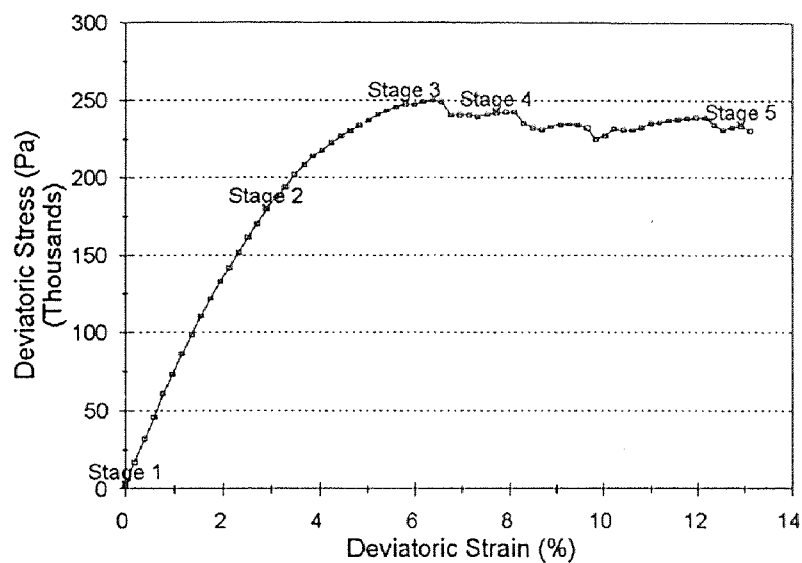


Figure 3.5 150-Particle Simulation (1 of 4)

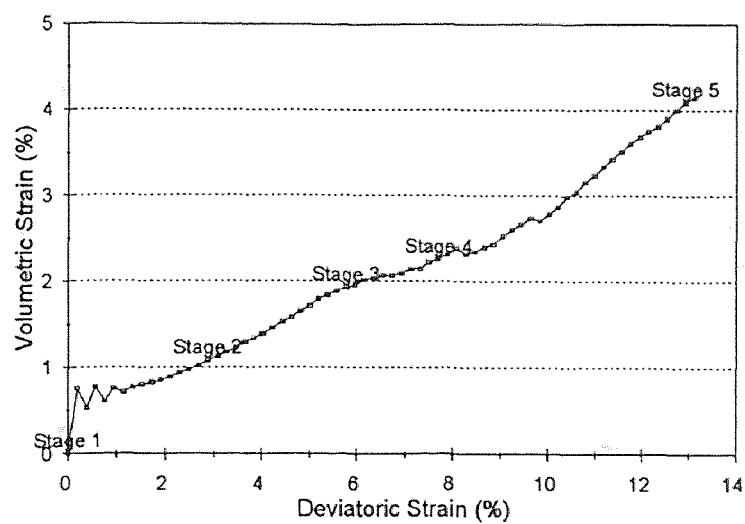


Figure 3.6 150-Particle Simulation (2 of 4)

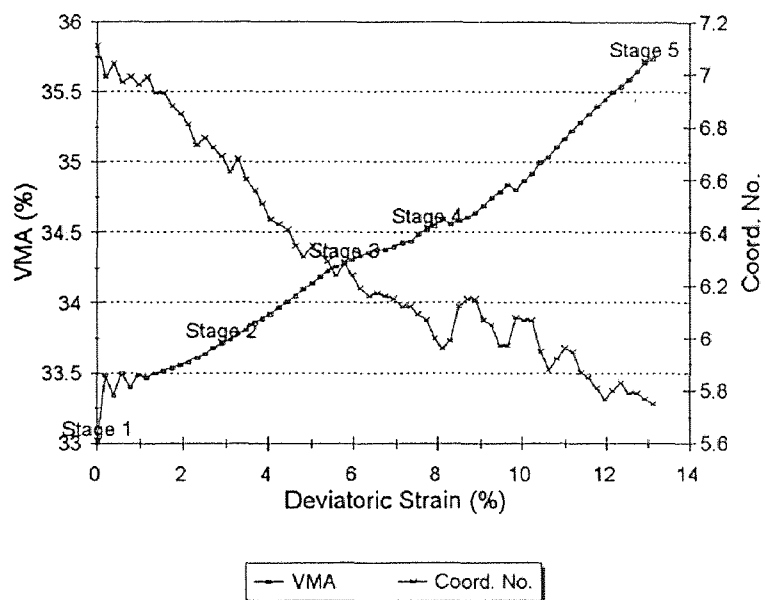


Figure 3.7 150-Particle Simulation (3 of 4)

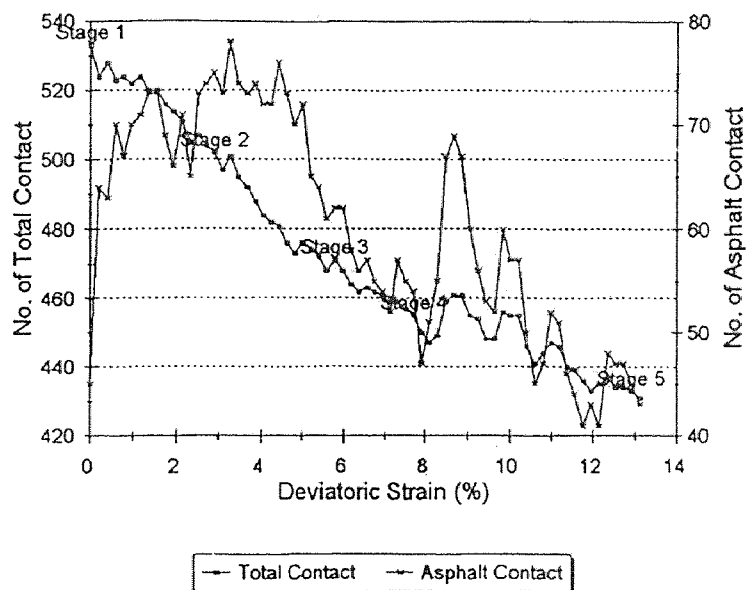


Figure 3.8 150-Particle Simulation (4 of 4)

dimensional sample. Figures 3.10 through 3.14 show the relative movements and incremental rotations of aggregate particles at each stage. From Figures 3.10 through 3.14, it indicates that particle displacement and rotations increased as the deviatoric strain increased. The maximum incremental rotation increased from Stages 1 to 3, remained constant at stage 4 and then increased to its maximum value at stage 5 (Figure 3.15). This implies that the assembly reached its maximum strength at Stage 3 before failure by rearranging its packing structure to generate the maximum interlock. After failure there was particle rotation along the central region where the failure occurred. The sliding at the contacts for various stages follow a similar trend as the principal stress in the Z direction for the five stages (Figure 3.16). It indicates that the local maximum shear stresses at the contacts are in phase with the macroscopic principal stress.

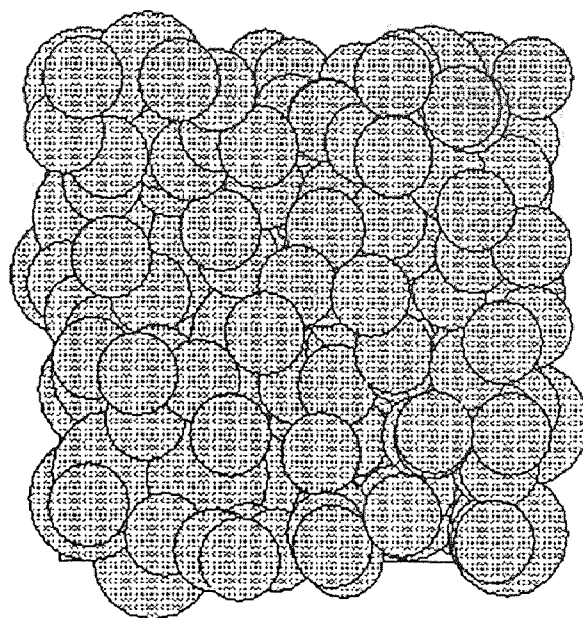


Figure 3.9 A Snapshot of a Simulated HMA Assembly After Compaction

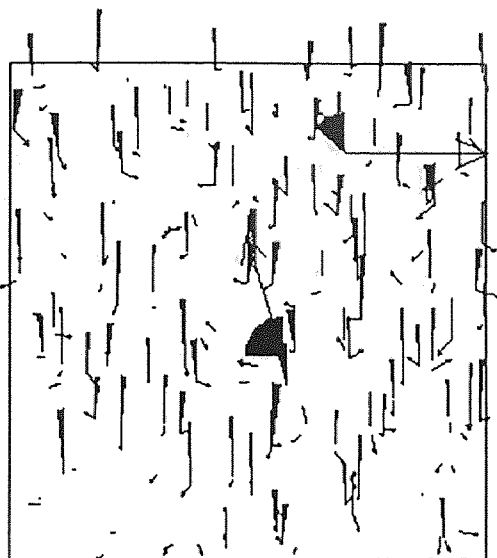


Figure 3.10 Aggregate Particle Movement in a Simulated HMA (Stage 1)

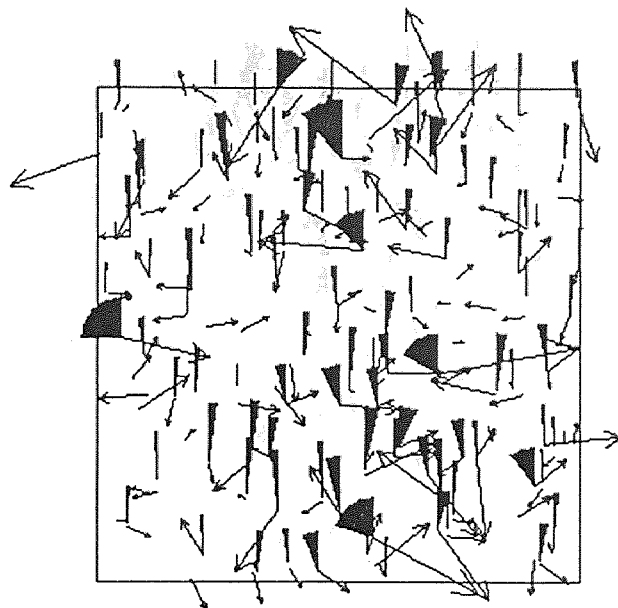


Figure 3.11 Aggregate Particle Movement in a Simulated HMA (Stage 2)

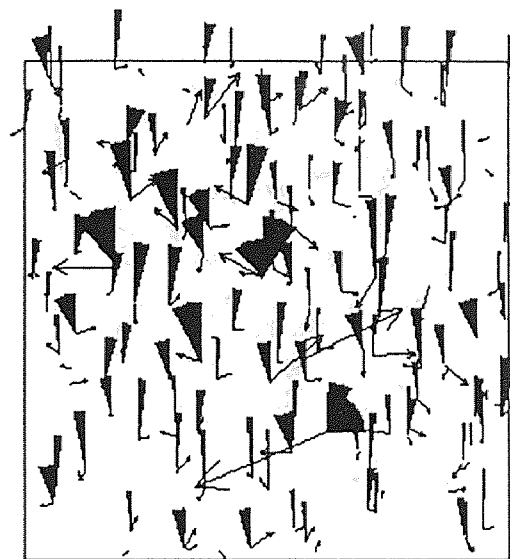


Figure 3.12 Aggregate Particle Movement in a Simulated HMA (Stage 3)

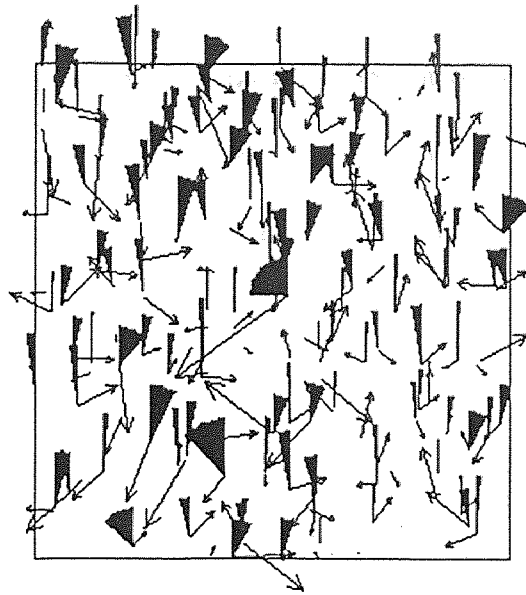


Figure 3.13 Aggregate Particle Movement in a Simulated HMA (Stage 4)

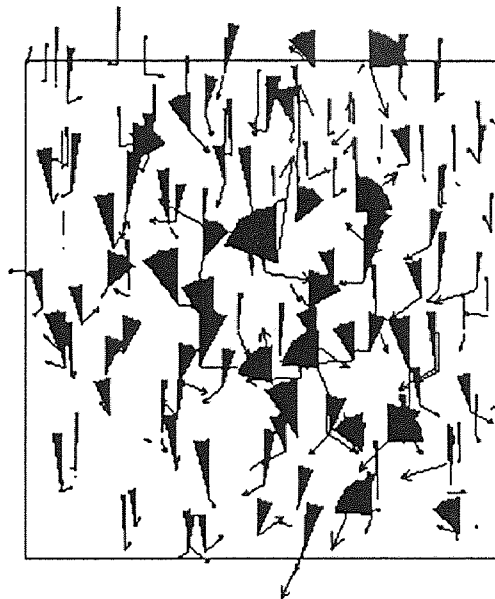


Figure 3.14 Aggregate Particle Movement in a Simulated HMA (Stage 5)

3.5.1.1 Sensitivity Tests

To investigate the influence of asphalt binder thickness on the stress-strain behavior (under constant P test) the asphalt binder thickness was varied from 0.1 mm to 0.4 mm (i.e. L_{\min} varied from 0.2 to 0.8 mm). Results of this simulation are shown in Figures 3.17 and 3.18. Those two figures indicate that the asphalt binder thickness has nominal contribution to the strength of HMA under constant P tests. This may due to the dense packing of the aggregate particles and aggregate interlocks and contacts contribute to the majority of the HMA strength for constant P tests.

Figures 3.19 and 3.20 show the compression and extension test results. The maximum deviatoric stress under compression test is 50 kPa higher than that under extension test (both are constant P tests). Figure 3.20 also shows that the variations in volumetric strain for the compression test and the extension test are quite different.

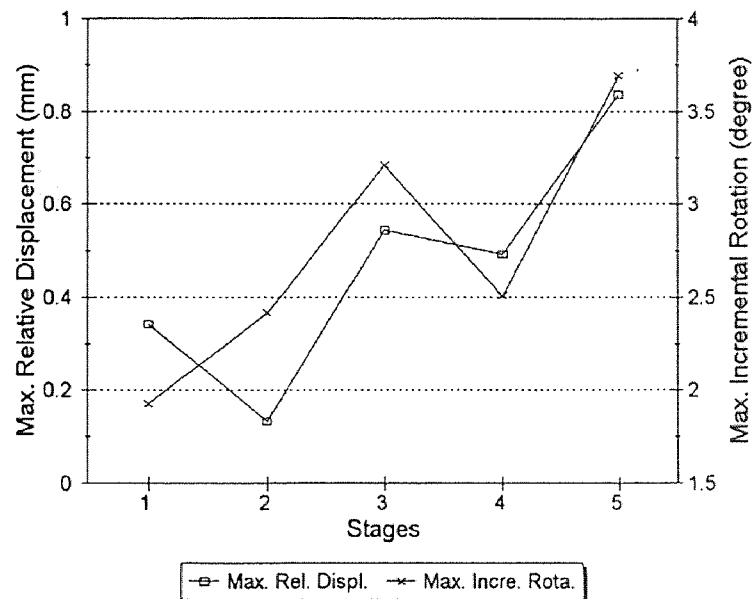


Figure 3.15 Max. Relative Displacement and Max. Incremental Rotation at Different Stages

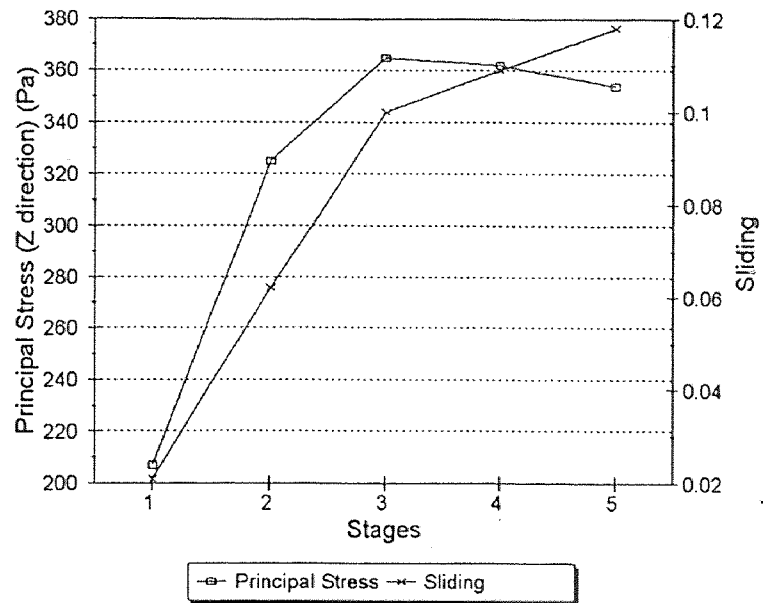


Figure 3.16 Principal Stress and Contact Sliding at Different Stages

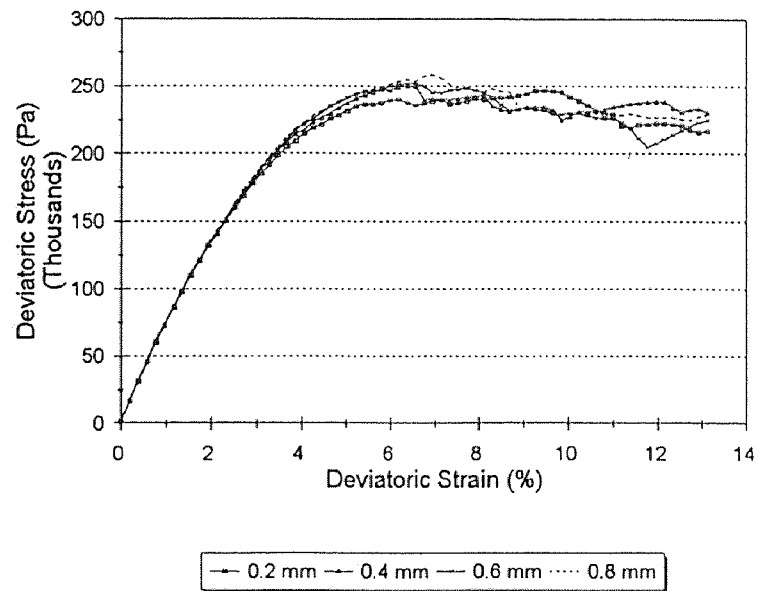


Figure 3.17 Effects of Asphalt Binder Thickness (1 of 2)

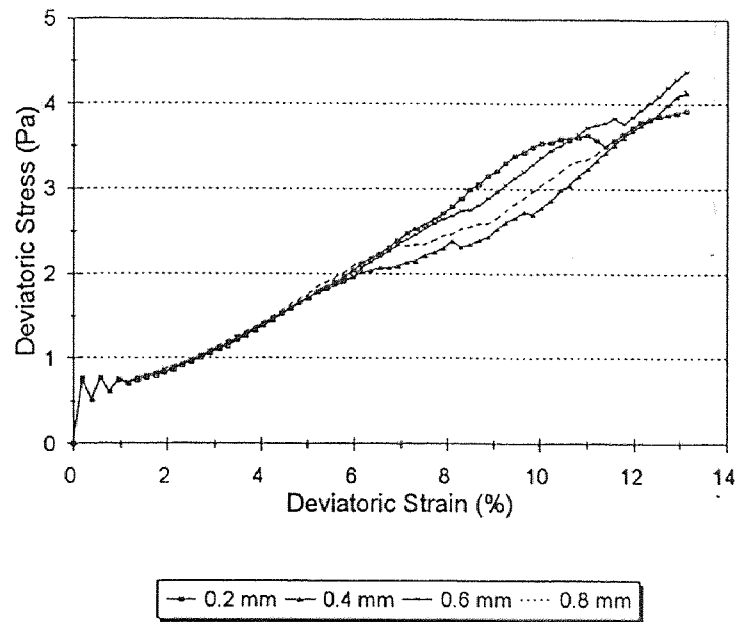


Figure 3.18 Effects of Asphalt Binder Thickness (2 of 2)

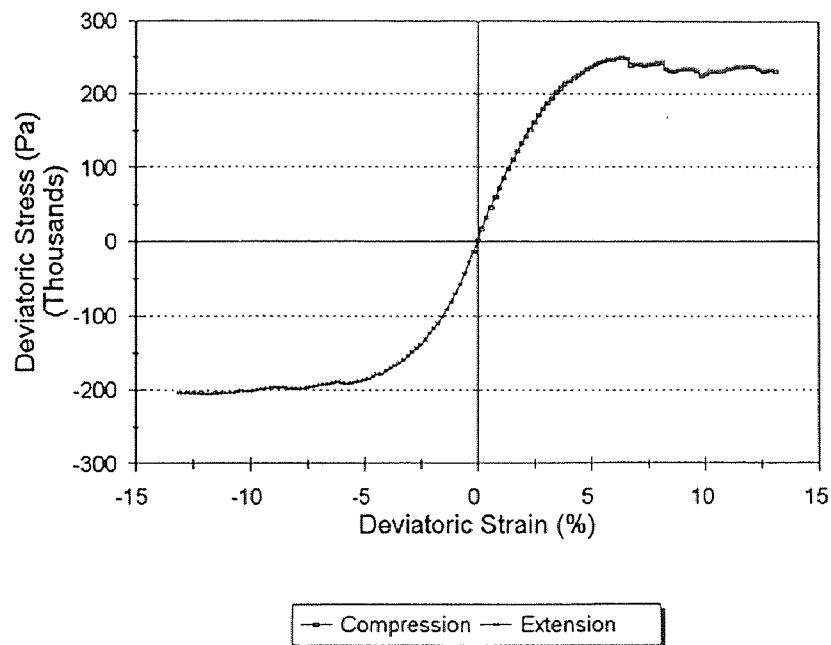


Figure 3.19 Compression Vs. Extension Tests (1 of 2)

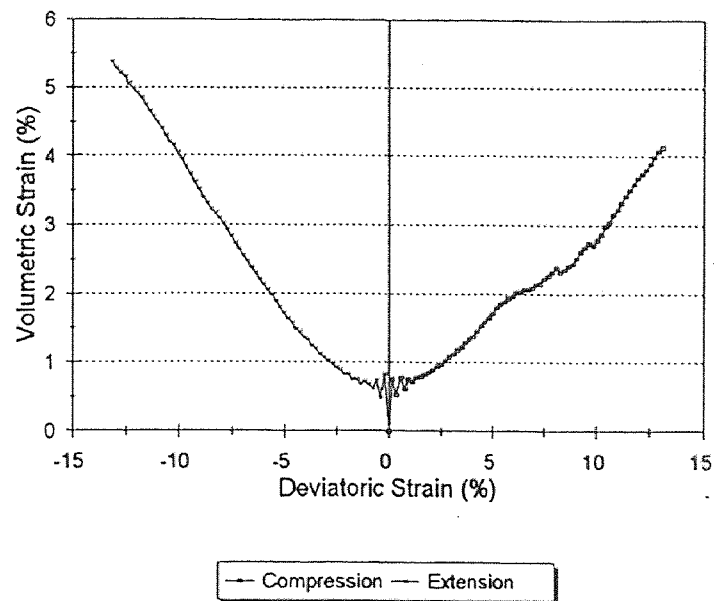


Figure 3.19 Compression Vs. Extension Tests (2 of 2)

3.5.2 The 512-particle Simulation

Macroscopic Behavior

The global stress-strain behavior of the 512-particle simulation is shown in Figure 3.21. The ASBAL simulated the residual stress at the beginning of the laboratory test. The residual stress (about 25 kPa) was caused by the compaction of the sample. The simulation showed close-to-linear stress-strain behavior of the laboratory test upto an axial strain value of 7.5% and the specimen failed after axial strain value of 8%. The post-peak behavior of laboratory test result was also successfully simulated by the ASBAL. The yield stress was around 350 kPa and initial modulus was approximately 4.2 MPa under the simulated loading. Since the testing temperature and loading rate were not available (Lee

and Dass, 1993), the standard laboratory testing temperature of 20°C (68°F), and maximum global strain rate of 0.001 (1/sec) were assumed for the simulation.

The global volumetric strain during the simulation was controlled to match that in the laboratory as shown in Figure 3.22. The simulated *VMA* values increased from 0.38 to 0.40 while the laboratory measured HMA values increased from 0.38 to 0.39. The slight difference (0.01, or 1%) in VMA values at the end of test (when the sample failed) may be due to the precision of laboratory measurement and the change in the shape of sample after failure.

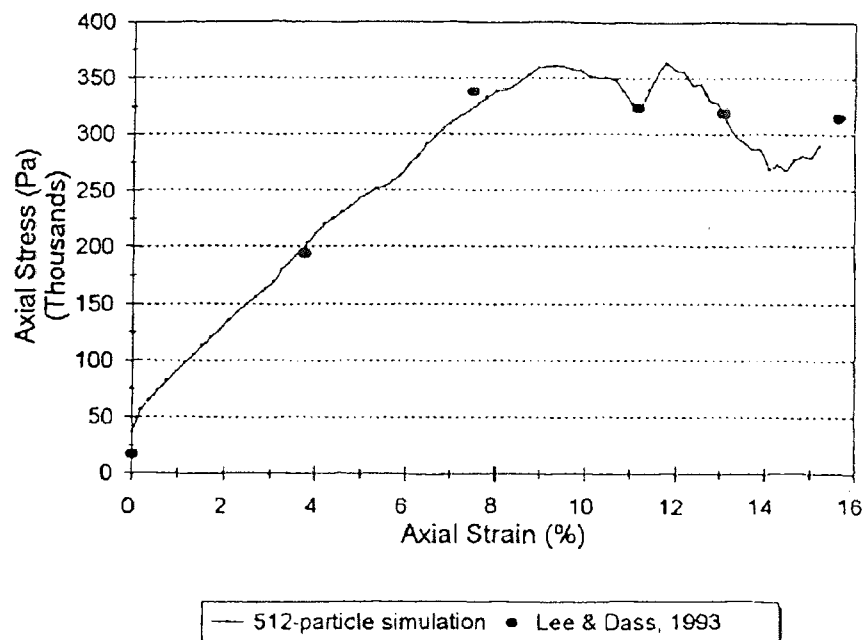


Figure 3.21 Simulation of A Laboratory Test (1 of 3)

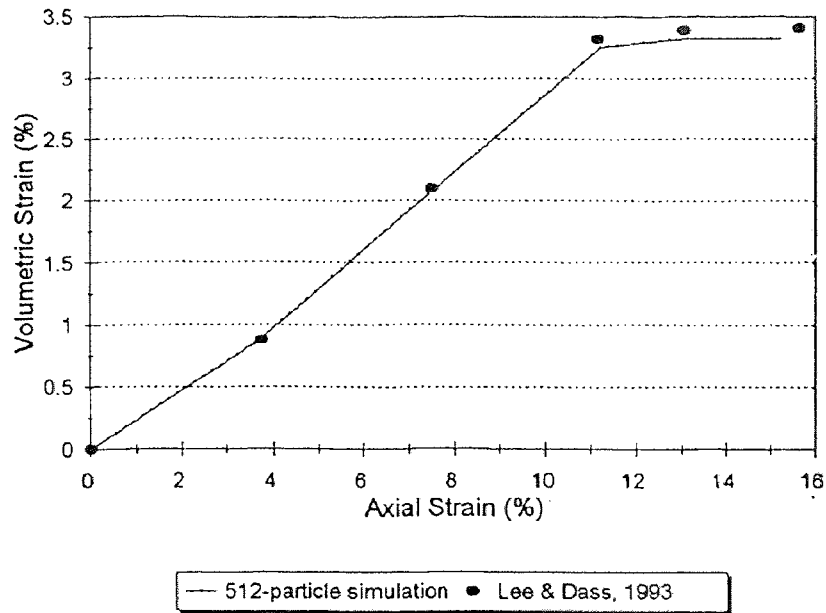


Figure 3.22 Simulation of A Laboratory Test (2 of 3)

Microscopic Structures during the Simulation

The coordination number for the laboratory test data increased from 8.32 to 8.91. However, the effective coordination number reduced from 4.8 to 4.28. The effective coordination number was calculated based on the assumption that contact forces occurred only when the thickness asphalt binder was less or equal to 0.3 mm. For the simulation, the coordination number increased significantly at the initial stage of the test then fluctuated between 7 and 7.5 during the rest of the simulation (Figure 3.23). For the simulation without asphalt binder, the coordination numbers varied between 3.6 and 4.8 which is approximately the same range that reported in Lee and Dass (1993). This implies that the effective coordination numbers reported in Lee and Dass (1993) gives that of dry

contacts only (Type I contacts) rather than the total contacts (Type I and Type II contacts).

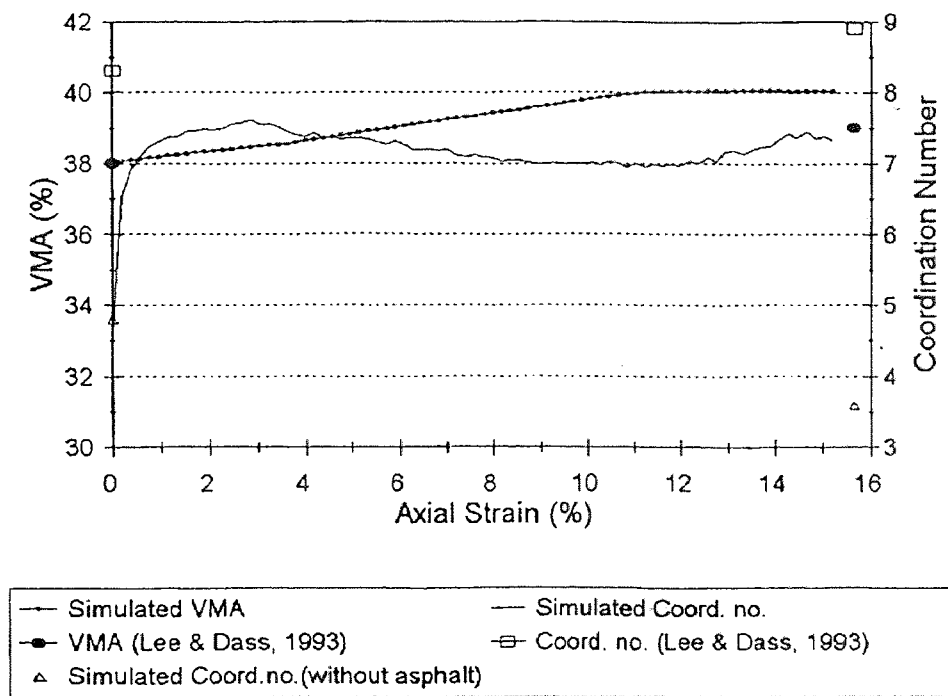


Figure 3.23 Simulation of A Laboratory Test (3 of 3)

The next chapter describes an attempt to simulate the behavior of HMA at different temperatures.

CHAPTER 4

NUMERICAL SIMULATION - TEMPERATURE EFFECTS

4.1 Introduction

Asphalt pavement surfaces are “black” and are good absorbers of radiation. The top asphalt layer is cold in the morning, hot during midday, and cool down in the evening. The bottom of asphalt layer may have an approximately constant temperature during the day or during different seasons (depending on the thickness) but vary during the year. Since HMA is thermally sensitive, the performance and distress of HMA are a function of temperature.

Thermal cracks occur when the thermal stresses exceed the tensile strength of the material. The behavior of pavement materials due to thermal expansion or contractions was studied by Williamson, (1972). A temperature drop of 22°C to -18°C can induce a thermal stress of 22 MPa on HMA (Williamson, 1972). The coefficients of thermal expansion for aggregates and asphalt cement are approximately 4×10^{-6} 1/°C for quartzite pebble and 600×10^{-6} 1/°C for asphalt cement above glassy temperature. Therefore, asphalt binder is more susceptible to thermal effects.

In this chapter, the mechanical behavior of HMA due to change in temperature is investigated. The master curves of asphalt binder from SHRP research at different temperatures were used in this research. The Burgers' element parameters of springs and dashpots were back-calculated at different temperatures from master curves. The resulting Burgers' parameters and other properties of asphalt and aggregate were used to simulate the mechanical behavior of HMA.

4.2 Characterizing Rheological Properties of Asphalt Binder at Different Temperature

4.2.1 Van der Poel's Nomograph

The thermal properties of asphalt binder were described first by Van der Poel (1954). Van der Poel developed a nomograph to estimate the asphalt stiffness over a wide range of temperatures and loading times for a variety of asphalt binder. This nomograph was constructed from penetration test and viscosity tests at different temperatures. Van der Poel's nomograph is still widely used for pavement design and analysis.

4.2.2 SHRP Specification for Asphalt Binder

The SHRP program proposed specifications to characterize asphalt binder. Here it was assumed and verified that the asphalt binder is a thermally simple material. Therefore, linear viscoelastic theory and time-temperature superposition theory are valid for asphalt binders (Anderson, et al. 1994). The SHRP specification for asphalt binder assumes that asphalt binders reach a constant stiffness at very low temperatures and exhibit Newtonian behavior at high temperatures.

From medium to high temperatures, the dynamic shear modulus can characterize asphalt binder. The dynamic shear rheometer, a device to measure dynamic shear modulus, consists of parallel plates between which the asphalt binder is tested using sinusoidal shear loading. This test can measure dynamic complex modulus values of asphalt binder from 10 MPa to 1 kPa. At low temperatures the bending beam rheometer can characterize asphalt binder. The bending beam rheometer is a simple flexural creep

test where an asphalt beam is loaded at mid-span for 240 sec. The dynamic shear rheometer and the bending beam rheometer tests measure the same properties of asphalt binders at high and low temperatures. The time-temperature superposition produces a master curve for a specific asphalt binder (see Appendix F).

4.3 Obtaining Input Parameters at Different Temperatures for ASBAL

4.3.1 The Characteristic Parameters for Binders

The characteristic parameters of the master curve for a specific asphalt binder consist of the following (Anderson, et al., 1994):

- The glassy modulus, G_g^* : the value of complex modulus at low temperature and high loading frequency. For most asphalt, this shear glassy modulus is approximately 10^3 MPa.
- The steady state viscosity, η_o : the steady-state viscosity is that when the asphalt binder behaves like a Newtonian fluid. The limit of steady-state viscosity occurs at a phase angle of 90° .
- The cross over frequency, ω_c : Cross-over frequency is the loading frequency at which the loss modulus is equal to the storage modulus, thus, phase angle is 45° .
- The rheological index, R : The rheological index is defined as $[G_g^* - G^*(\omega_c)]$ where $G^*(\omega_c)$ is the modulus at cross-over frequency.

Figure 4.1 shows the relationship between the above parameters.

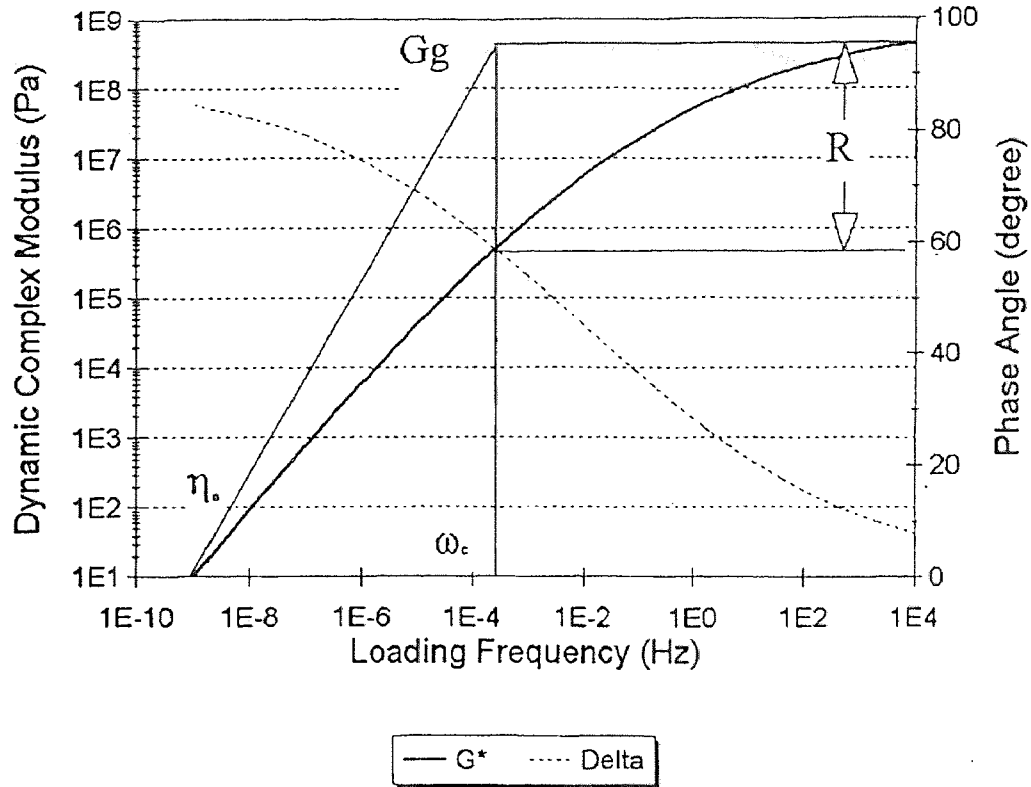


Figure 4.1 Typical Master Curve for Asphalt Binder with Characteristic Parameters

4.3.2 SHRP Core Binder - AAB-1 (Tank)

SHRP test results are used to calculate the thermal effects on HMA. The properties of SHRP binder AAB-1 (Tank) are as follows (Anderson et al., 1994):

- The defining temperature is -11.6°C
- The glassy temperature is -13.9°C
- The glassy modulus is $8.91 \times 10^8 \text{ Pa}$
- The cross-over frequency is 0.010715 rad/sec
- The rheologic index is 1.76

- The limiting temperatures for resistance to low temperature cracking were obtained by restrained tension tests: the temperature at 200 MPa loading for 2 hours is -28°C; the temperature at $G^* = 67$ MPa at 10 rad/sec is -4 °C.

4.3.3 Estimating the Dynamic Complex Modulus and Phase Angle using SHRP Equations

The relationship of dynamic complex shear modulus and shear modulus:

$$|G^*(\omega)| = \frac{|\tau(\omega)|}{|\gamma(\omega)|} \quad (4.1)$$

$$G^*(\omega) = G'(\omega) + iG''(\omega) \quad (4.2)$$

$$G'(\omega) = |G^*(\omega)| \cos \delta \quad (4.3)$$

$$G''(\omega) = |G^*(\omega)| \sin \delta \quad (4.4)$$

where

$G^*(\omega)$: dynamic complex modulus (Pa)

$|\tau(\omega)|$: absolute magnitude of the dynamic shear stress response (Pa),

$|\gamma(\omega)|$: absolute magnitude of the applied dynamic shear strain,

G' : dynamic storage modulus,

G'' : dynamic loss modulus,

δ : phase angle defined as: $\tan^{-1}(G''/G')$.

The dynamic complex shear modulus can be converted to dynamic complex linear elastic modulus without significant error by assuming asphalt binder to be incompressible (i.e. Poisson's ratio is 0.5) (Christensen and Anderson, 1993):

$$E^*(\omega) = 3 \times G^*(\omega) \quad (4.5)$$

where

E^* : dynamic complex linear modulus.

The dynamic modulus at the reference temperature of 25°C for SHRP binders can be expressed by (Anderson et al., 1994):

$$G^*(\omega) = G_g \times \left[1 + \left(\frac{\omega_c}{\omega} \right)^{\log(2)/R} \right]^{-R/\log(2)} \quad (4.6)$$

where

$G^*(\omega)$: the shear dynamic complex modulus, (Pa)

G_g : the shear glassy modulus, (Pa)

ω_c : the cross-over frequency, (rad/sec)

ω : the reduced loading frequency, (rad/sec)

R : the rheological index (0.81 if viscous flow is approached).

Please note that the loading frequency rad/sec can be converted to Hertz (cycle/sec) by multiplying 2π .

The phase angle for SHRP binders can be obtained by:

$$\delta = \frac{90}{1 + \left(\frac{\omega}{\omega_c} \right)^{\log(2)/R}} \quad (4.7)$$

where δ : delta or the phase angle, (degrees).

Once the dynamic complex modulus and phase angle values are obtained for different loading frequencies, the master curve for the asphalt binder at a given temperature can be calculated. Figure 4.2 shows that the master curve for SHRP binder

AAB-1 (Tank) at 25°C. Figure 4.2 shows that the dynamic complex modulus approaches the glassy modulus at very high loading frequency and it behaves like a Newtonian fluid at very low loading frequency.

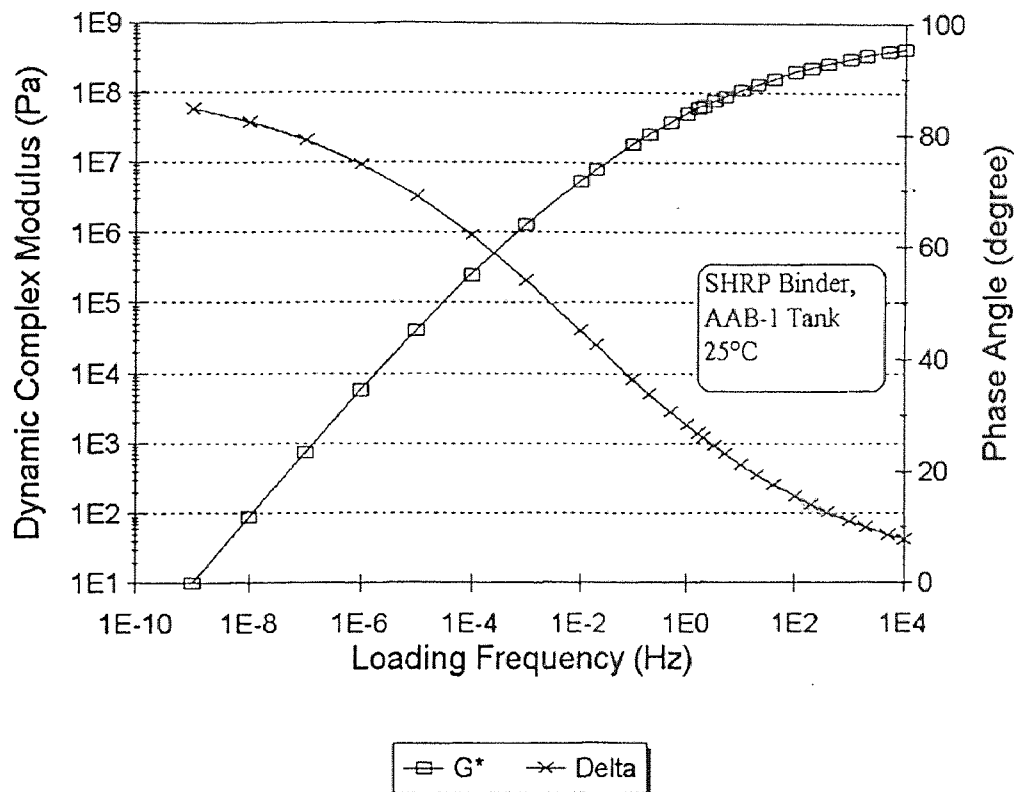


Figure 4.2 The Master Curve of SHRP Binder (AAB-1, Tank) at 25°C

4.3.4 Shift Factors and Construction of Master Curves at Different Temperatures

In order to obtain the master curve at different temperatures, Time-Temperature Superposition can be applied and shift factors can be computed at desired temperatures. Master curves for characterizing asphalt binders can be produced by shifting the data curves at different temperatures to the reference temperature (see Appendix F) . The shift

factors can be calculated from the Arrhenius equation or the William-Landel-Ferry equation for temperature values below and above the defining temperature (T_d).

The Arrhenius equation is expressed as:

$$\log\left(\frac{a(T)}{a(T_d)}\right) = 2.303 \times \frac{E_a}{R_g} \times \left(\frac{1}{T} - \frac{1}{T_d}\right) \quad (4.8)$$

where

$a(T)/a(T_d)$: the shift factor relative to the defining temperature,

E_a : the activation energy for flow below T_d (≈ 261 KJ/mol.),

R_g : the ideal gas constant (8.34 J/mol.-°K).

The WLF equation (William-Landel-Ferry) is expressed as:

$$\log\left(\frac{a(T)}{a(T_d)}\right) = -C_1 \frac{(T - T_d)}{(C_2 + T - T_d)} \quad (4.9)$$

where

C_1 : empirically determined constant (19 for SHRP binders),

C_2 : empirically determined constant (92 for SHRP binders),

The defining temperature for SHRP asphalt binder (Tank, TFOT, or PAV) determined from the above equations has a precision of $\pm 3^\circ\text{C}$ based on pooled variances and a 95 % confidence interval.

The shift factors for different temperatures (5, 15, 25, 35 °C) with respect to T_d and 25°C are listed in Table 4.1. Please note that shift factors are with referenced to 25°C as the master curve is known at this temperature. The master curves at other temperatures can be obtained by horizontally shifting the master curve at 25°C (i.e. by

calculating the new frequencies at desired temperatures). Figure 4.3 shows the master curves of SHRP binder, AAB-1 (Tank), at temperatures 5, 15, 25, and 35 °C.

Table 4.1 The Shift Factors based on Time-Temperature Superposition (SHRP Binder, AAB-1, Tank)

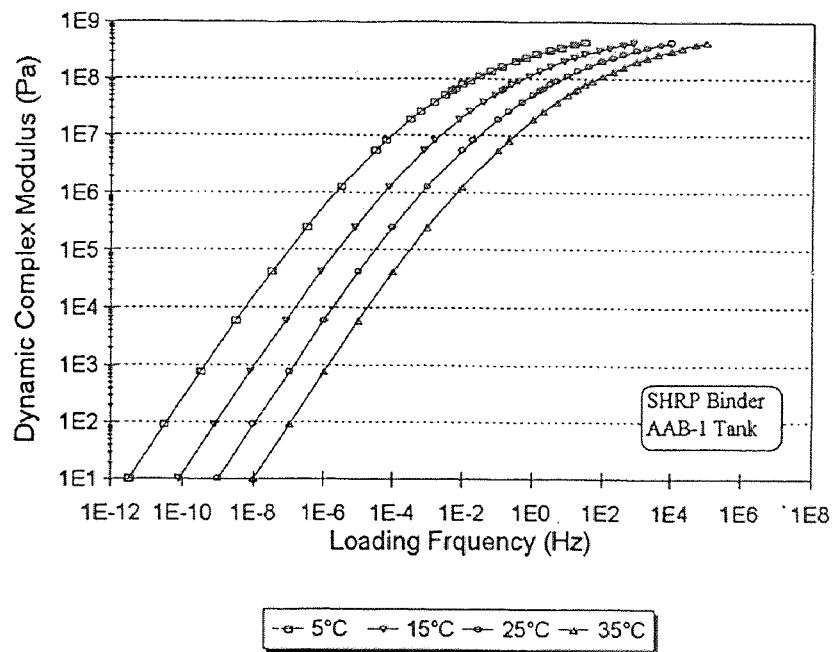
	Shift Factors at Different Temperature			
Temperatures (°C)	5	15	25	35
Referenced to 25°C	2.5	1.1	0.0	-1.0

4.3.5 Back-calculation of Input Parameters for Burgers' Element from The Master Curves

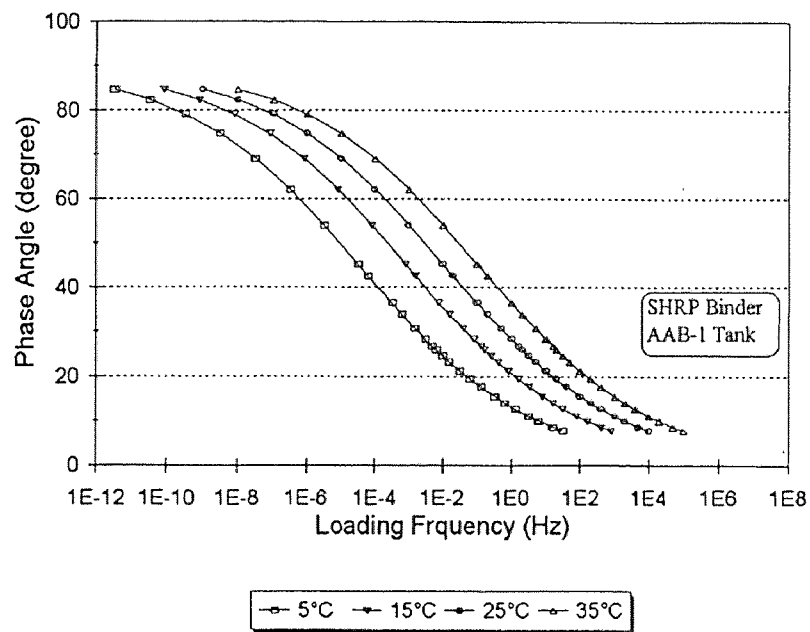
Once the master curves are available, the input parameters in Burgers' element can be computed by curve fitting techniques. The PACE program (SWK(PE), Inc., 1994) uses multiple linear regression to fit master curves into linear viscoelastic elements (Two-Parallel-Maxwell). The detailed outputs of the fitted parameters (E_i , V_i , E_{ii} , V_{ii}) are shown in Appendix G.

From the two-parallel-Maxwell elements the input parameters for the Burgers' element can be calculated. The conversion equations between the above two are presented as follows (the details of derivation are presented in Appendix H):

$$\begin{aligned}
 E_1 &= A \\
 V_1 &= B/D \\
 E_2 &= \frac{AB^2}{ABC - A^2D - B^2} \\
 V_2 &= \frac{A^2B}{ABC - A^2D - B^2}
 \end{aligned} \tag{8.10}$$



(a)



(b)

Figure 4.3 Master Curves of SHRP Binder, AAB-1 (Tank) at Different Temperatures

and

$$\begin{aligned}
 A &= E_i + E_{ii} \\
 B &= E_i E_{ii} \left(\frac{1}{V_i} + \frac{1}{V_{ii}} \right) \\
 C &= \frac{E_i}{V_i} + \frac{E_{ii}}{V_{ii}} \\
 D &= \frac{E_i E_{ii}}{V_i V_{ii}}
 \end{aligned} \tag{8.11}$$

where

E_1, V_1, E_2, V_2 : parameters for Burgers' model (subscript 1 for the Maxwell unit, subscript 2 for the Kelvin unit),

E_i, V_i, E_{ii}, V_{ii} : parameters for Two-Parallel-Maxwell model.

The fitted input parameters for Two-Parallel-Maxwell element and the converted input parameters for Burgers' element (E_1, V_1, E_2, V_2) at the desired temperatures (i.e. 5, 15, 25, 35 °C) are shown in Table 4.2.

Table 4.2 Linear Viscoelastic Parameters for the SHRP Binder (AAB-1, Tank)

Temperature (°C)	5	15	25	35
Two-Parallel-Maxwell Element				
E_i (Pa)	1.8E9	9.3E8	4.3E8	1.7E8
V_i (Pa-s)	1.4E9	4.0E8	1.2E8	3.3E7
E_{ii} (Pa)	6.7E7	6.0E8	4.4E8	2.7E8
V_{ii} (Pa-s)	1.3E7	9.9E6	6.4E6	3.4E6
Burgers' Element				
E_1 (Pa)	1.9E9	1.5E9	8.7E8	4.4E8
V_1 (Pa-s)	1.4E9	4.1E8	1.3E8	3.6E7
E_2 (Pa)	9.5E10	2.7E9	1.0E9	3.8E8
V_2 (Pa-s)	1.8E10	7.2E7	2.9E7	1.1E7

4.3.6 Other Parameters

The numerical values for other parameters of asphalt binder such as L_{\min} (two times of the asphalt coating thickness) and cohesion are shown in Table 4.3. L_{\min} was calculated from the thermal expansion coefficient which is 200×10^{-6} ($1/^{\circ}\text{C}$) and 600×10^{-6} ($1/^{\circ}\text{C}$) below T_g and above T_g respectively. At higher temperature due to thermal expansion L_{\min} should increase but due to low viscosity the thickness is reduced. Since the author does not have physical information about L_{\min} at different temperatures, a value of 0.4 mm for L_{\min} was used in all the simulations. Cohesion of asphalt was estimated by upgrading/down-grading one order of magnitude when decreasing/increasing every 10°C . Asphalt penetration values show similar behavior.

Using thermal expansion coefficient (14.4×10^{-6} $1/^{\circ}\text{C}$) for quartzite pebble, radii of aggregate particles at different temperatures were calculated and shown in Table 4.3.

Table 4.3 Input Parameters for Asphalt and Particle Properties at Different Temperatures

Temperature ($^{\circ}\text{C}$)	5	15	25	35
Other Asphalt Properties				
Cohesion (Pa)	1E7	1E6	1E5	1E4
Particle Properties				
size 1 radius (mm)	9.99971	9.99986	10.00000	10.00050
size 2 radius (mm)	14.99971	14.99986	15.00000	15.00050

4.4 ASBAL Simulation of HMA at Different Temperatures

4.4.1 Simulation of Unconfined Compression Tests

The unconfined compression tests show the temperature susceptibility of HMA. ASBAL program was run with appropriate parameters corresponding to the following temperatures: 5, 15, 25, and 35 °C. Each simulation had 150 aggregate particles of two sizes (see Table 4.3). Friction coefficient for particle-particle contacts was 0.7. The normal and tangential stiffnesses were 2×10^8 Pa-mm and 1×10^8 Pa-mm respectively. Numerical values of asphalt binder at different temperatures (Tables 4.2 and 4.3) were used in this simulation. The global axial strain-rate was 0.001 (1/sec). Lateral stress was made equal to zero to simulate unconfined compression tests.

Macroscopic Behavior

Figure 4.4 shows the variation of deviatoric stresses with axial strain for different temperatures. It follows the trend of higher strength at low temperatures. Maximum deviatoric strengths were 165, 125, 100, and 90 MPa for 5, 15, 25, 35 °C, respectively.

The pre-failure and post-failure stages show non-linear behavior. However, there is no significant deviation of volumetric strain at different temperatures (Figure 4.5).

Microscopic Behavior

Figures 4.6, 4.7, and 4.8 show the variation of coordination numbers, number of asphalt contacts, and number of dry contacts (particle-particle) respectively with deviatoric strain. Coordination number is the average number of contacts (asphalt contacts plus dry

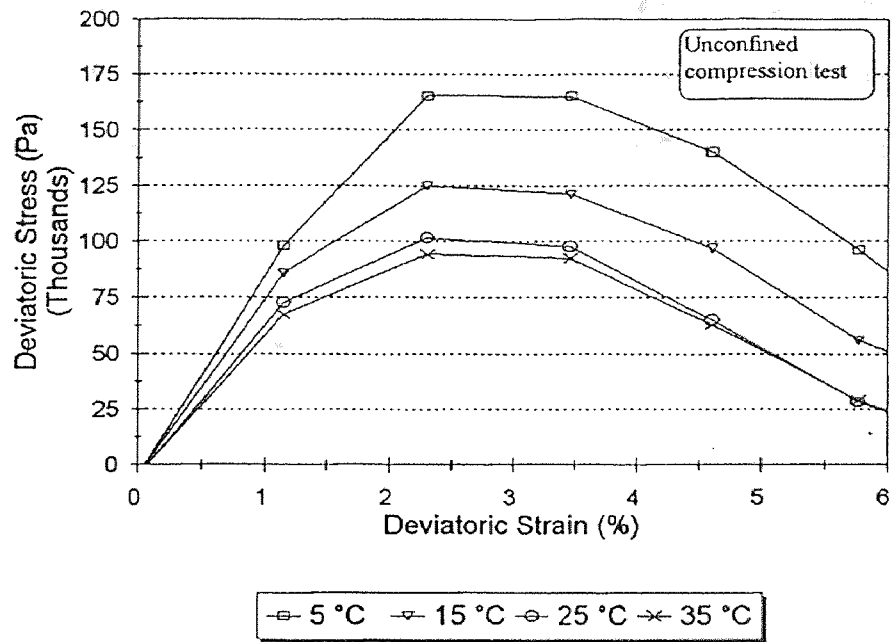


Figure 4.4 Simulation of Unconfined Compression Tests (1 of 5)

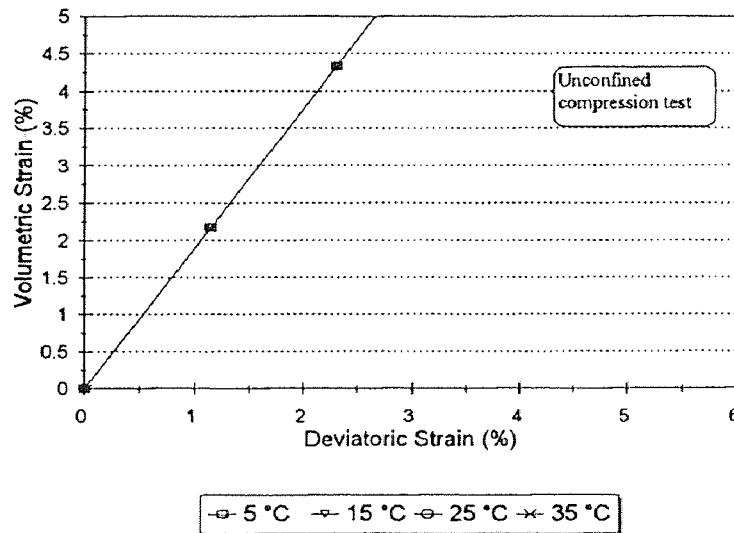


Figure 4.5 Simulation of Unconfined Compression Tests (2 of 5)

contacts) per particle. Figure 4.6 shows that the coordination number decreased for all four temperatures. Similar trend was observed for changes of dry contacts (see Figure 4.7). The variation of number of asphalt contacts with deviatoric strain varied for different temperatures (Figure 4.8). This behavior is reflected in changes of internal structures.

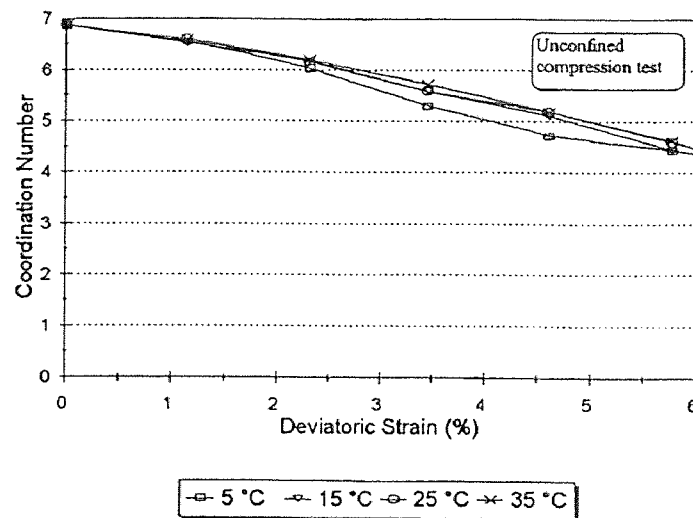


Figure 4.6 Simulation of Unconfined Compression Tests (3 of 5)

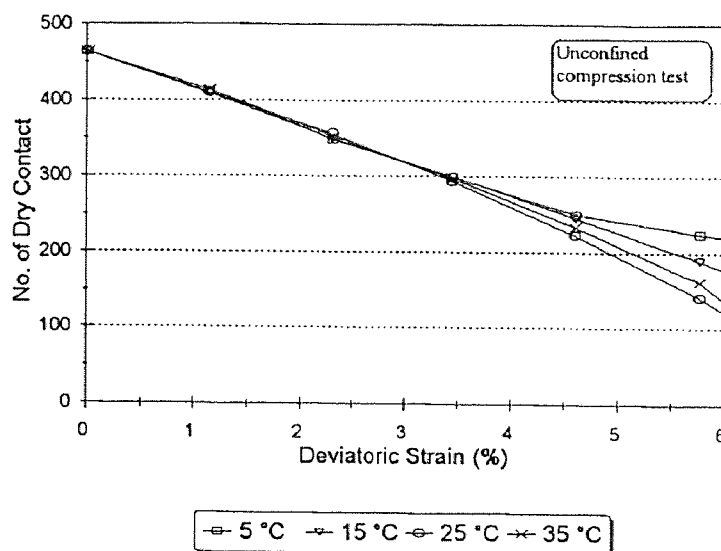


Figure 4.7 Simulation of Unconfined Compression Tests (4 of 5)

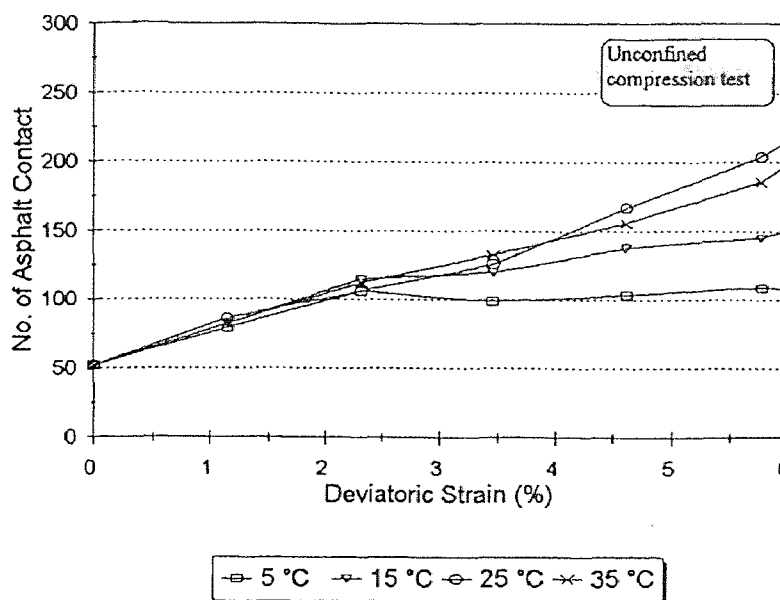


Figure 4.8 Simulation of Unconfined Compression Tests (5 of 5)

4.4.2 Simulation of Constant-P Tests

Simulation of constant-P (average stress) tests were performed with an average confining pressure of 300 kPa. The rest of input parameters were the same as these for the unconfined compression tests.

Macroscopic Behavior

Figure 4.9 shows the variation of deviatoric stresses with axial strain at different temperatures of constant-P tests. It shows a similar trend as those for unconfined compression tests. Maximum deviatoric stresses are 450, 340, 300, and 280 kPa for 5, 15, 25, 35 °C, respectively.

Figures 4.10 shows that volumetric strains increased as deviatoric strains increased, i.e. the specimens dilated during the simulation as observed in the laboratory

tests. There is a “cross-over” deviatoric strain at 3% when the volumetric strains were the same for four temperatures. Beyond the cross-over deviatoric strain, volumetric strain values increased at high rate at lower temperatures.

Microscopic Behavior

Figure 4.11 shows that coordination number decreased at all temperatures with the increase in deviatoric strain. While the dry contacts (see Figure 4.12) show a similar trend as in coordination numbers, the asphalt contacts fluctuated during the simulation (Figure 4.13). This is expected, as the coordination numbers are based on total contacts, and the dry contacts out-numbered the asphalt contacts.

The above simulation of HMA at different temperatures demonstrated the ability of ASBAL to simulate the influence of temperature on HMA. It also shows the ability for ASBAL to include new developments in fundamental research (such as: SHRP).

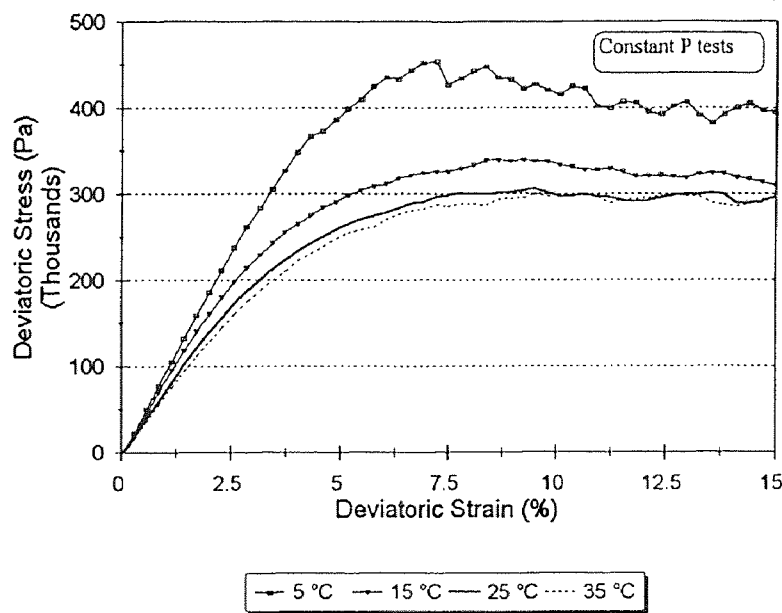


Figure 4.9 Simulation of Constant-P Tests (1 of 5)

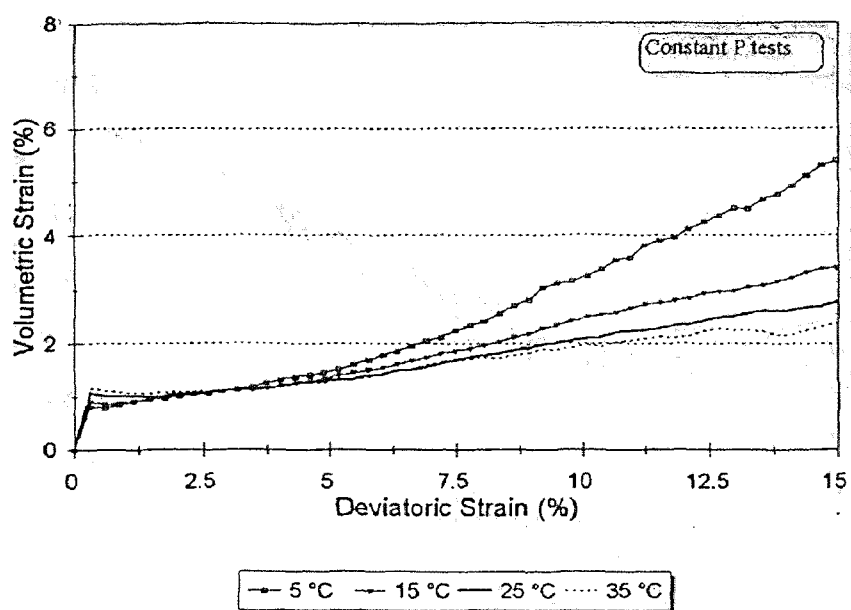


Figure 4.10 Simulation of Constant-P Tests (2 of 5)

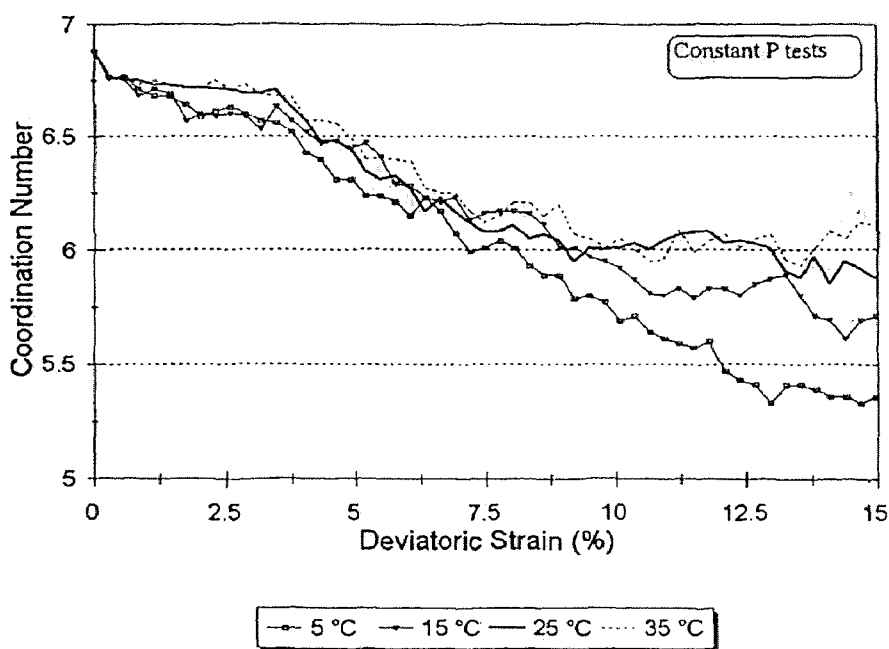


Figure 4.11 Simulation of Constant-P Tests (3 of 5)

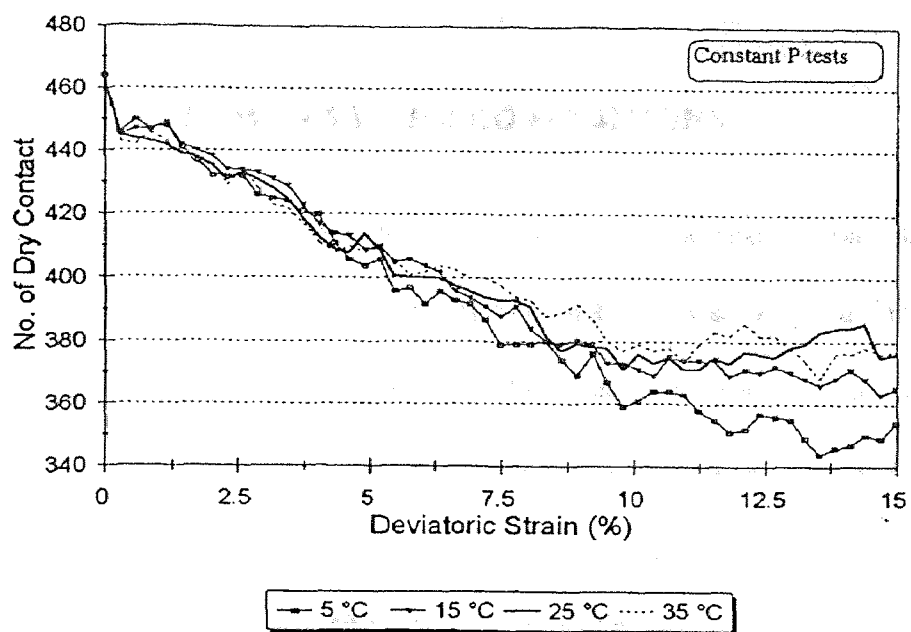


Figure 4.12 Simulation of Constant-P Tests (4 of 5)

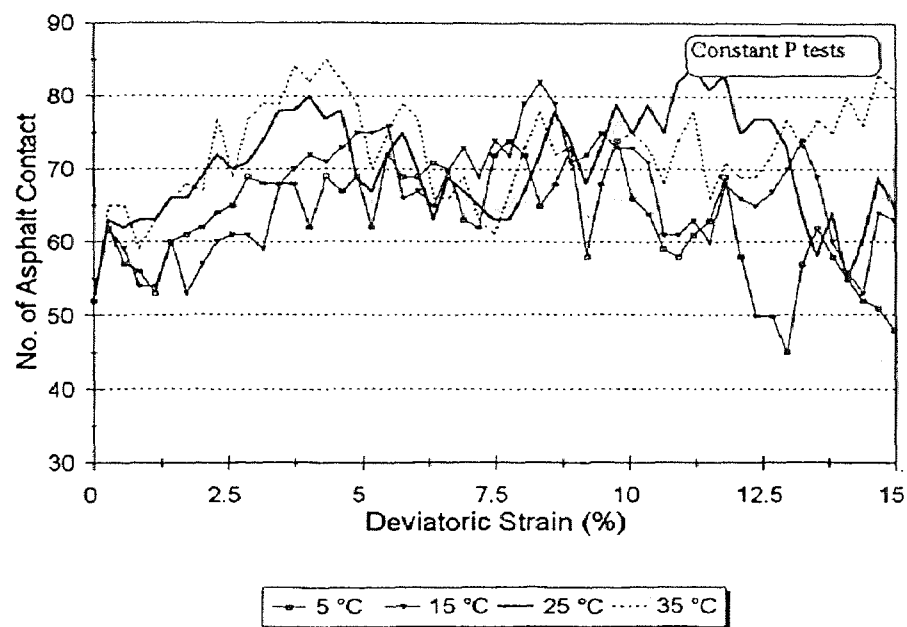


Figure 4.13 Simulation of Constant-P Tests (5 of 5)

CHAPTER 5

SUMMARY AND CONCLUSIONS

For the first time Discrete Element Method is applied to model the mechanical behavior of hot mix asphalt concrete. The discrete behavior of HMA was accounted for and modeled using a microscopic model based on DEM. The Material Formulation (Part I) is described in Chapters 2, and Numerical Simulations (Part II) are described in Chapters 3 and 4.

5.1 Material Formulation

Micromechanics of the components of hot mix asphalt concrete was investigated to model the HMA. A micromechanical model based on discrete element method, that could describe and account for the factors that contribute to the mechanical behavior of HMA, was selected. Basic mechanics of the model are described. The hot mix asphalt concrete is modeled here as an assembly of asphalt coated aggregates. The model was originally developed to model soil as an assembly of granular aggregate. The mechanical contributions of the asphalt binder are represented in this model with the aid of viscoelastic elements. Three basic viscoelastic elements were considered in detail, as probable candidates for inclusion in this model. Constitutive laws for Maxwell, Kelvin-Voigt, and Burgers' elements under monotonic loading were derived in order to observe the responses of each element under constant strain rate tests. The chosen element should be able to describe the instantaneous elasticity, creep under constant stress, stress relaxation under constant strain, instantaneous recovery, delayed recovery, permanent or plastic deformation of asphalt binder. Both the Maxwell and Burgers' element were able

to adequately describe the typical mechanical behavior of asphalt cement. Then the constitutive laws for all the elements under cyclic loading were obtained. For each element, the variation of complex modulus and phase angle with the frequency of cyclic loading was plotted. The Master Curve, developed by the Strategic Highway Research Program from dynamic shear rheometer and bending beam rheometer tests, was compared with the predictions from three elements. The Maxwell and Burgers' elements were able to predict the trends but only Burgers' element was able to match the measured master curve. Therefore, it was concluded that Burgers' element is the best element to describe the complete mechanical behavior of asphalt binders. The Burgers' element was, therefore, included in the model based on DEM to simulate the mechanical behavior of hot mix asphalt concrete.

5.2 Numerical Simulation

A description of discrete element method with special reference to TRUBAL was given elaborating how the particulate mechanics are accounted for in this method. The ASBAL program, developed in this research, is a modification of TRUBAL program to include the asphalt binder. Two types of contacts, aggregate-asphalt-aggregate and aggregate-aggregate contacts, were considered in this model. Then a detailed description of the development of ASBAL program is given where Burgers' elements were inserted to model the aggregate-asphalt-aggregate and part of aggregate-aggregate contacts. The Mohr-Coulomb failure criterion was retained and modified to account for separation of asphalt coated particles due to rotation. The mechanics of the ASBAL program was

elaborated with a flowchart and a list of steps needed to simulate mechanical tests for hot mix asphalt concrete. Two different assemblies were used to simulate the mechanical behavior of HMA. The first assembly consisted of 150 particles of two sizes and it was used to observe the ability of ASBAL to simulate the general mechanical behavior of HMA. The variation of macro or the stress-strain behavior and, snapshots and reports of microscopic parameters such as number of contacts, coordination number, rotation, particle movement were generated to investigate the ability of ASBAL to simulate the mechanical behavior of HMA. Furthermore, a sensitivity analysis was performed to determine the extent of influence of some of the key microscopic input parameters on the mechanical behavior of HMA. The second assembly consisted of 512 particles and it simulated a carefully conducted physical test with x-ray tomography results. The ASBAL program was able to simulate and match the physical experimental test results with 512 particles. This simulation highlighted accuracy of some of the assumptions made in presenting the physical results. The ability to match the physical experimental results validated the methodology and implementation associated with DEM modeling of HMA.

The susceptibility of asphalt concrete to variation in temperature was modeled by appropriately modifying the input parameters to ASBAL program. Time-temperature superposition theory was used to generate the master curve for asphalt binder at the different temperatures. Using the master curve, the input parameters for the Burgers' element were calculated at different temperatures. Using the input parameters, the unconfined compression tests and constant P tests were simulated with 150 particle assembly for four different temperatures. Unconfined compression test and constant-P

tests showed that the shear strength and the elastic modulus of HMA at higher temperatures are a fraction of those at lower temperatures. All the specimens irrespective of the temperature and testing method dilated with the applied load. Since the ASBAL can effectively model the influence of temperature on HMA, using ASBAL it will be feasible to understand the mechanism of rutting and to propose a performance-based test for rutting of HMA.

APPENDIX A
CONTACT AREA OF TWO ASPHALT -COATED PARTICLES

CONTACT AREA OF TWO ASPHALT -COATED PARTICLES

I. Particle-Asphalt-Particle Contact Area

The contact area of two asphalt-coated particles is considered as a circular shape. Since the asphalt layer is relatively thin (less than 3% of particle diameter), the contact area is taken at mid-way between the distances when Type II (particle-asphalt-particle) and Type I (particle-particle) contacts start (see Figure A.1). Therefore, the distance between the centroids of two asphalt-coated particles is expressed as:

$$\overline{P_a P_b} = \overline{O P_a} + \overline{O P_b} \quad (\text{A.1})$$

or

$$r_1 + r_2 + \frac{L_{\min}}{2} = \sqrt{\left(r_1 + \frac{L_{\min}}{2}\right)^2 - x^2} + \sqrt{\left(r_2 + \frac{L_{\min}}{2}\right)^2 - x^2} \quad (\text{A.2})$$

where r_1 : radius of particle a ,

r_2 : radius of particle b ,

L_{\min} : minimum distance between two particle surface when asphalt takes effect,

x : radius of contact area.

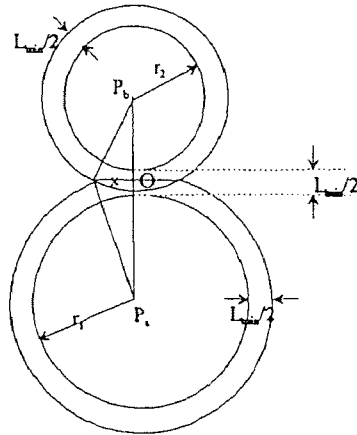


Figure A.1 Diagram of Particle-Asphalt-Particle Contact Area

Taking square of equation (A.2) yields:

$$\begin{aligned} & r_1^2 + r_2^2 + \left(\frac{L_{\min}}{2}\right)^2 + 2r_1\left(\frac{L_{\min}}{2}\right) + 2r_2\left(\frac{L_{\min}}{2}\right) + 2r_1r_2 \\ &= \left(r_1 + \frac{L_{\min}}{2}\right)^2 - x^2 + \left(r_2 + \frac{L_{\min}}{2}\right)^2 - x^2 + 2\sqrt{\left(r_1 + \frac{L_{\min}}{2}\right)^2 - x^2} \sqrt{\left(r_2 + \frac{L_{\min}}{2}\right)^2 - x^2} \end{aligned} \quad (\text{A.3})$$

Re-arranging equation (A.3):

$$2x^2 + 2r_1r_2 - \left(\frac{L_{\min}}{2}\right)^2 = 2\sqrt{\left(r_1 + \frac{L_{\min}}{2}\right)^2 - x^2} \sqrt{\left(r_2 + \frac{L_{\min}}{2}\right)^2 - x^2}. \quad (\text{A.4})$$

Taking square of equation (A.4):

$$\begin{aligned} & 4x^4 + 4\left[2r_1r_2 - \left(\frac{L_{\min}}{2}\right)^2\right]x^2 + \left[2r_1r_2 - \left(\frac{L_{\min}}{2}\right)^2\right]^2 \\ &= 4\left[\left(r_1 + \frac{L_{\min}}{2}\right)^2 - x^2\right]\left[\left(r_2 + \frac{L_{\min}}{2}\right)^2 - x^2\right] \end{aligned} \quad (\text{A.5})$$

R-arranging equation (A.5) yields:

$$\begin{aligned} & 4x^2\left[(r_1 + r_2)^2 + 2(r_1 + r_2)\left(\frac{L_{\min}}{2}\right) + \left(\frac{L_{\min}}{2}\right)^2\right] \\ &= 3\left(\frac{L_{\min}}{2}\right)^4 + 8(r_1 + r_2)\left(\frac{L_{\min}}{2}\right)^3 + 4(r_1^2 + 5r_1r_2 + r_2^2)\left(\frac{L_{\min}}{2}\right)^2 + 8r_1r_2(r_1 + r_2)\left(\frac{L_{\min}}{2}\right) \end{aligned} \quad (\text{A.6})$$

or

$$\begin{aligned} & 4x^2\left(r_1 + r_2 + \frac{L_{\min}}{2}\right)^2 \\ &= 3\left(\frac{L_{\min}}{2}\right)^4 + 8(r_1 + r_2)\left(\frac{L_{\min}}{2}\right)^3 + 4(r_1^2 + 5r_1r_2 + r_2^2)\left(\frac{L_{\min}}{2}\right)^2 + 8r_1r_2(r_1 + r_2)\left(\frac{L_{\min}}{2}\right) \end{aligned} \quad (\text{A.7})$$

Therefore,

$$x^2 = \frac{3\left(\frac{L_{\min}}{2}\right)^4 + 8(r_1 + r_2)\left(\frac{L_{\min}}{2}\right)^3 + 4(r_1^2 + 5r_1r_2 + r_2^2)\left(\frac{L_{\min}}{2}\right)^2 + 8r_1r_2(r_1 + r_2)\left(\frac{L_{\min}}{2}\right)}{4\left(r_1 + r_2 + \frac{L_{\min}}{2}\right)^2} \quad (\text{A.8})$$

The particle-asphalt-particle contact area (A_{ct}) is expressed by:

$$\begin{aligned} A_{ct} &= \pi \cdot x^2 \\ &= \pi \frac{3\left(\frac{L_{\min}}{2}\right)^4 + 8(r_1 + r_2)\left(\frac{L_{\min}}{2}\right)^3 + 4(r_1^2 + 5r_1r_2 + r_2^2)\left(\frac{L_{\min}}{2}\right)^2 + 8r_1r_2(r_1 + r_2)\left(\frac{L_{\min}}{2}\right)}{4\left(r_1 + r_2 + \frac{L_{\min}}{2}\right)^2} \quad (\text{A.9}) \end{aligned}$$

For a special case when one size of particle is used (i.e. $r_1 = r_2 = r$), the contact area is expressed as:

$$A_{ct} = \pi \frac{3\left(\frac{L_{\min}}{2}\right)^4 + 16r\left(\frac{L_{\min}}{2}\right)^3 + 28r^2\left(\frac{L_{\min}}{2}\right)^2 + 16r^3\left(\frac{L_{\min}}{2}\right)}{4\left(2r + \frac{L_{\min}}{2}\right)^2} \quad (\text{A.10})$$

II. Particle-Particle Contact Area

Even though cohesion of particle-particle contact is usually assumed to be zero, the following derivation of particle-particle contact area is presented for completeness. For particle-particle or dry contact, the radius of contact area is expressed as (see Figure A.2):

$$D = \sqrt{r_1^2 - y^2} + \sqrt{r_2^2 - y^2} \quad (\text{A.11})$$

where D : distance between centroids of particles A and B,

y : radius of particle-particle contact area.

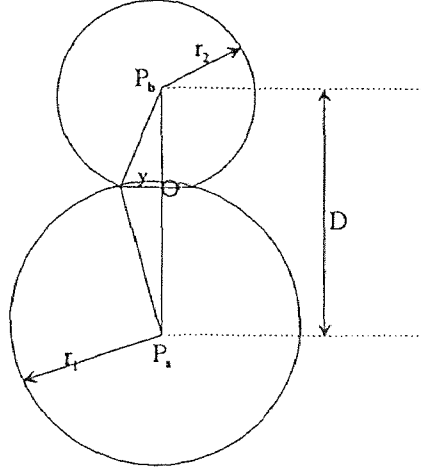


Figure A.2 Diagram of Particle-Particle Contact Area

Taking square of equation (A.11), we get:

$$D^2 = r_1^2 + r_2^2 - 2y^2 + 2\sqrt{r_1^2 - y^2}\sqrt{r_2^2 - y^2} \quad (\text{A.12})$$

Re-arranging equation (A.12) and taking square yields:

$$4y^4 + 4(D^2 - r_1^2 - r_2^2)y^2 + (D^2 - r_1^2 - r_2^2)^2 = 4[r_1^2 r_2^2 - (r_1^2 + r_2^2)y^2 + y^4] \quad (\text{A.13})$$

Simplifying equation (A.13) yields:

$$y^2 = \frac{2(r_1^2 + r_2^2)D^2 - D^4 - (r_1^2 - r_2^2)^2}{4D^2} \quad (\text{A.14})$$

Therefore, the particle-particle contact area (A_{cl}') is expressed as:

$$\begin{aligned} A_{cl}' &= \pi \cdot y^2 \\ &= \pi \frac{2(r_1^2 + r_2^2)D^2 - D^4 - (r_1^2 - r_2^2)^2}{4D^2} \end{aligned} \quad (\text{A.15})$$

For a special case when one size of particle is used (i.e. $r_1 = r_2 = r$), the particle-particle contact area is expressed as:

$$A_{cl}' = \pi \frac{4r^2 D^2 - D^4}{4D^2} \quad (\text{A.16})$$

APPENDIX B
ASFORD SUBROUTINE

```

      SUBROUTINE ASFORD (C,B1,B2)

C
C  3-D FORCE/DISPLACEMENT LAW
C  INCORPORATE THE EFFECT OF SECOND PHASE, ASPHALT
C  Decemeber, 1994
C  Using Bergers' Element to model asphalt
C  INPUT:
C      C: POINTER "IAD"
C      B1: ADDRESS "IAB1"
C      B2: ADDRESS "IAB2"
C  OUPUT:
C      STRESS TENSOR: SSAMPLE (K,I) K,I=1 TO 3
C
      SAVE
      INCLUDE 'asb3.inc'
      DIMENSION C(*),B1(*),B2(*)
      DIMENSION Z(3),RN(3),UDR(3),UND(3),TD(3),THDR(3),
      .          SD(3),TRS(3),TEMP(3),F(3),FZ(3)
      DOUBLE PRECISION dpb1(10),dpb2(10),dpz(3),ddel,dzm2,dzm,
      .          drdif,dra,drb,dxxm
C*
      DOUBLE PRECISION P1N,P2N,Q1N,Q2N,Q1S,Q2S,P1S,P2S,R1N,R1S,
      +          AN,AS,TT1N,TT2N,TT1S,TT2S,TEMP1N,TEMP2N,
      +          TEMP3n,TEMP1S,TEMP2S,TEMP3s,DSIGMAN,DSIGMAS,
      +          thk, t1, t2, tp1, tp2, Act, Actp
      COMMON /FRD/ RA,RB,FRIC,COHES,STIFN,STIFS,elnn,e2nn,elss,e2ss,
      +          edalnn,eda2nn,edalss,eda2ss
      COMMON /htzfrd/ ccnh,ccsh
C*
      DATA ak13 /0.3333333/

C  ----- START OF HERTZ SECTION -----
C      IF (hertz) then
C          do 2 i = 1,3
C              ddel      = del(i)
C              I3        = I+3
C              dpb1(i)   = b1(i)
C              dpb1(i3)  = b1(i3)
C              dpb2(i)   = b2(i)
C              dpb2(i3)  = b2(i3)

```

```

c          dpZ(I)  = dpB2(I) + dpB2(I3) - dpB1(I) - dpB1(I3)
C--- allow for periodic space ---
c          if (dABS(dpZ(I)) .gt. dDEL) then
c              dsxm  = dSIGN(xmax(i),dpZ(I))
c              dpZ(I) = dpZ(I) - dsxm
c              if (i .eq. 2) then
c                  dpz(1) = dpz(1) - dmod(xshear,xmax(1)) * dsxm
c                  if (dabs(dpz(1)) .gt. del(1)) then
c                      dpz(1) = dpz(1) - dsign(xmax(1),dpz(1))
c                  endif
c              endif
c          endif
c      2  continue
C
c      dZM2  = 0.0
c      dra   = ra
c      drb   = rb
c      DO 5 I=1,3
c          I6=I+6
c          z(i)  = dpz(i)
c          dZM2  = dZM2 + dpZ(I) * dpZ(I)
c          zm2   = dzm2
c          UDR(I) = B2(I6) - B1(I6)
C-----allow for grid motion-----
c          DO 3 J = 1,3
c              UDR(I) = UDR(I) + EDGRID(I,J) * dpZ(J)
c      3  CONTINUE
c      5  CONTINUE
C
c      dZM  = dSQRT(dZM2)
c      zm   = dzm
c      dRDIF = dZM - (dra + drb)
C*ORIGIANL      IF (dRDIF .ge. 0.0) GOTO 300
c      unorm = -drdif
c      rsum  = ra + rb
c      rdif  = drdif
C----- END OF HERTZ SECTION -----
C-----START OF LINEAR CONTACT LAW -----
c      else

```

```

DO 7 I=1,3
  I3 = I + 3
  Z(I) = B2(I) + B2(I3) - B1(I) - B1(I3)
C  ( allow for periodic space)
  IF (ABS(Z(I)) .gt. DEL(I)) then
    xmmm = xmax(i)
    sxm = sign(xmmm,z(i))
    Z(I) = Z(I) - sxm
    if (i .eq. 2) then
      z(1) = z(1) - dmod(xshear,xmax(1)) * sxm
      if (abs(z(1)) .gt. del(1)) then
        xmml = xmax(1)
        z(1) = z(1) - sign(xmml,z(1))
      endif
    endif
  endif
7 continue
  ZM2=0.0
  DO 10 I=1,3
    I6=I+6
    I3=I+3
C
    ZM2 = ZM2 + Z(I) * Z(I)
    UDR(I) = B2(I6) - B1(I6)
C  (allow for grid motion)
    DO 8 J = 1,3
      UDR(I) = UDR(I) + EDGRID(I,J) * Z(J)
    8 CONTINUE
  10 CONTINUE
    ZM=SQRT(ZM2)
    RSUM = RA + RB
    RDIF=ZM-RSUM
C  ENDIF
C ----- END OF LINEAR CONTACT SECTION -----
C
C      1. AFTER CONTACT, PROCEEDS
C  THREE CASES: 2. BEFORE CONTACT, ENCOUNTER ASPHALT (GOTO 200)
C      3. BEFORE CONTACT, NO EFFECTS OF ASPHALT (GOTO 300)
C

```

```

      IF (RDIF.GT.dmin) GOTO 300
      IF (RDIF.GT.0.0) GOTO 200
C
C ( CASE 1. AFTER Particle CONTACT )
C
      UNDM=0.0
      DO 20 I=1,3
      RN(I)=Z(I)/ZM
20 UNDM=UNDM+UDR(I)*RN(I)
C
      DO 30 I=1,3
      UND(I)=UNDM*RN(I)
30 TD(I)=UDR(I)-UND(I)
C ( START OF GEAR-WHEEL THEOREM )
      CALL CROSS(Z,TD,THDR)
C
      ZM2T=TDEL/ZM2
      DO 40 I=1,3
      F(I)=C(I)
      THDR(I)=THDR(I)*ZM2T
40 FZ(I)=C(I)
      DO 50 N=1,2
      CALL CROSS(THDR,F,C)
      DO 50 I=1,3
      C(I)=C(I)+FZ(I)
50 F(I)=0.5*(FZ(I)+C(I))
C tangential displacement at contact
C due to relative rotation
      DO 60 I=1,3
      I15=I+15
60 TRS(I)=B2(I15)*RB+B1(I15)*RA
      CALL CROSS(TRS,RN,SD)
C ( END OF GEAR-WHEEL THEOREM )
C---CALCULATE NORMAL FORCE, COMBINED EFFECTS---
C      if (hertz) then
C          c(4) = ccnh * unorm**1.5 - UNDM*(ASTIFN+ASCCN)
C          aksloc = ccsh * c(4)**ak13
C      else
          qln = edalnn

```



```

      q2n = edalnn*eda2nn/e2nn
      pln = edalnn/elnn+edalnn/e2nn+eda2nn/e2nn
      p2n = edalnn*eda2nn/elnn/e2nn
      An = sqrt(abs(pln**2-4*p2n))
      r1n = (pln+An)/2/p2n
      r2n = (pln-An)/2/p2n
      ttl1n = p2n*r1n*(r1n-r2n)
      tt2n = p2n*r2n*(r1n-r2n)
      templn = q1n*undm/p2n/r1n/r2n
      temp2n = undm*(q1n-q2n*r1n)/ttl1n
      temp3n = undm*(q2n*r2n-q1n)/tt2n
      dsigman= templn
      +      + temp2n*exp(-r1n*tdel)
      +      + temp3n*exp(-r2n*tdel)
c**** disable asphalt
c      dsigman = dsigman * 0.0
      C(4) = C(4) - UNDM*stifn - dsigman
c* force in tension is ruled out after particle contact
      IF (C(4) .LT. 0.0) GOTO 300
      aksloc = stifs
c      endif
c* count the total contacts
      NCONT = NCONT + 1
C---CALCULATE SHEAR FORCE, COMBINED EFFECTS---
      FSM = 0.0
      DO 70 I=1,3
        SD(I) = TD(I) - SD(I)
        q1s = edalss
        q2s = edalss*eda2ss/e2ss
        pls = edalss/elss+edalss/e2ss+eda2ss/e2ss
        p2s = edalss*eda2ss/elss/e2ss
        As = sqrt(abs(pls**2-4*p2s))
        r1s = (pls+As)/2/p2s
        r2s = (pls-As)/2/p2s
        ttl1s = p2s*r1s*(r1s-r2s)
        tt2s = p2s*r2s*(r1s-r2s)
        temp1s = q1s*sd(I)/p2s/r1s/r2s
        temp2s = sd(I)*(q1s-q2s*r1s)/ttl1s
        temp3s = sd(I)*(q2s*r2s-q1s)/tt2s

```

```

        dsigmas= templs
      +      + temp2s*exp(-r1s*tdel)
      +      + temp3s*exp(-r2s*tdel)
      C(I) = C(I) - SD(I)*aksloc - dsigmas
70 FSM    = FSM + C(I) * C(I)
      FSM    = SQRT(FSM)
c... Calculate P-A-P contact area, Act
      thk=dmin/2
      t1 = 3*thk**4+8*(ra+rb)*thk**3
      .   + 4*(ra**2+rb**2+5*ra*rb)*thk**2
      .   + 8*ra*rb*(ra+rb)*thk
      t2=4*(ra+rb+thk)**2
      Act=pi*t1/t2
c... Calculate P-P contact area, Actp
      tp1 = 2*(ra**2+rb**2)*ZM**2
      .   - ZM**4-(ra**2-rb**2)**2
      tp2 = 4*ZM**2
      Actp=Pi*tp1/tp2
C---CHECK FOR SLIP, COMBINED EFFECTS---
      FSMAX = (FRIC+ASMU) * C(4) + COHES*Actp +ACOH*Act
      if (fsmax .eq. 0.0) then
c  no friction
          slide = slide + 1.0
          do 75 i = 1,3
              c(i) = 0.0
75      continue
          else
c  some friction
              IF (FSM .LE. FSMAX) GOTO 90
c  no reduction in shear force
              SLIDE = SLIDE + 1.0
              if (fsm .eq. 0.0) then
                  rat = 0.0
              else
                  RAT = FSMAX / FSM
              endif
c  reduction in shear force
              DO 80 I=1,3
80          C(I) = C(I) * RAT

```

```

endif
C---RESOLVE FORCES TO GLOBAL DIRECTIONS---
90 CALL CROSS(C,RN,TEMP)
DO 100 I=1,3
  I18=I+18
  I21=I+21
  FNR=C(4)*RN(I)+C(I)
C    (save stress tensor)
  FNRS = FNR * RSUM
  DO 95 K = 1,3
    SSAMPL(K,I) = SSAMPL(K,I) - FNRS * RN(K)
95 CONTINUE
  B1(I18)=B1(I18)-FNR
  B2(I18)=B2(I18)+FNR
  B1(I21)=B1(I21)+TEMP(I)*RA
100 B2(I21)=B2(I21)+TEMP(I)*RB
C
  RETURN
C
C (CASE 2. BEFORE Particle CONTACT, ENCOUNTER ASPHALT effects)
C
200 UNDM=0.0
DO 220 I=1,3
  RN(I)=Z(I)/ZM
220 UNDM=UNDM+UDR(I)*RN(I)
C
DO 230 I=1,3
  UND(I)=UNDM*RN(I)
230 TD(I)=UDR(I)-UND(I)
C---CALCULATE NORMAL FORCE---
c    if (hertz) then
c      c(4) = ccnh * unorm**1.5 - UNDM*(ASTIFN+ASCCN)
c      aksloc = ccsh * c(4)**ak13
c    else
      qln = edalnn
      q2n = edalnn*eda2nn/e2nn
      pln = edalnn/elnn+edalnn/e2nn+eda2nn/e2nn
      p2n = edalnn*eda2nn/elnn/e2nn
      An = sqrt(abs(pln**2-4*p2n))

```

```

      r1n = (p1n+An)/2/p2n
      r2n = (p1n-An)/2/p2n
      tt1n = p2n*r1n*(r1n-r2n)
      tt2n = p2n*r2n*(r1n-r2n)
      temp1n = q1n*undm/p2n/r1n/r2n
      temp2n = undm*(q1n-q2n*r1n)/tt1n
      temp3n = undm*(q2n*r2n-q1n)/tt2n
      dsigman= temp1n
+           + temp2n*exp(-r1n*tdel)
+           + temp3n*exp(-r2n*tdel)
      C(4) = C(4) - dsigman
c* force in tension considered when asphalt effects
c* no tension currently
      IF (C(4) .LT. 0.0) GOTO 300
c      endif
c* count asphalt contacts and total contacts
      nascont = nascont + 1
      NCONT = NCONT + 1
C---CALCULATE SHEAR FORCE---
      FSM = 0.0
      DO 270 I=1,3
        SD(I) = TD(I) - SD(I)
        q1s = edalss
        q2s = edalss*eda2ss/e2ss
        p1s = edalss/elss+edalss/e2ss+eda2ss/e2ss
        p2s = edalss*eda2ss/elss/e2ss
        As = sqrt(abs(p1s**2-4*p2s))
        r1s = (p1s+As)/2/p2s
        r2s = (p1s-As)/2/p2s
        tt1s = p2s*r1s*(r1s-r2s)
        tt2s = p2s*r2s*(r1s-r2s)
        temp1s = q1s*sd(I)/p2s/r1s/r2s
        temp2s = sd(I)*(q1s-q2s*r1s)/tt1s
        temp3s = sd(I)*(q2s*r2s-q1s)/tt2s
        dsigmas= temp1s
+           + temp2s*exp(-r1s*tdel)
+           + temp3s*exp(-r2s*tdel)
        C(I) = C(I) - dsigmas
270 FSM = FSM + C(I) * C(I)

```

```

      FSM  = SQRT(FSM)
c... Calculate P-A-P contact area, Act
      thk=dmin/2
      t1 = 3*thk**4+8*(ra+rb)*thk**3
      .   + 4*(ra**2+rb**2+5*ra*rb)*thk**2
      .   + 8*ra*rb*(ra+rb)*thk
      t2=4*(ra+rb+thk)**2
      Act=pi*t1/t2
C---CHECK FOR SLIP---
      FSMAX = ASMU * C(4) + ACOH*Act
      if (fsmax .eq. 0.0) then
c* no friction
          slide = slide + 1.0
          do 275 i = 1,3
              c(i) = 0.0
275      continue
          else
              IF (FSM .LE. FSMAX) GOTO 290
c* kinematic friction
          SLIDE = SLIDE + 1.0
c* calculate reduction shear force
          if (fsm .eq. 0.0) then
              rat = 0.0
          else
              RAT = FSMAX / FSM
          endif
          DO 280 I=1,3
280      C(I) = C(I) * RAT
          endif
C---RESOLVE FORCES TO GLOBAL DIRECTIONS---
290 CALL CROSS(C,RN,TEMP)
      DO 299 I=1,3
          I18=I+18
          I21=I+21
          FNR=C(4)*RN(I)+C(I)
C      (save stress tensor)
          FNRS = FNR * RSUM
      DO 295 K = 1,3
          SSAMPL(K,I) = SSAMPL(K,I) - FNRS * RN(K)

```

```

295 CONTINUE
      B1(I18)=B1(I18)-FNR
      B2(I18)=B2(I18)+FNR
      B1(I21)=B1(I21)+TEMP(I)*RA
299 B2(I21)=B2(I21)+TEMP(I)*RB
C
      RETURN
C
C   (CASE 3. BEFORE ANY CONTACT, NO EFFECTS OF ASPHALT)
C
300 DO 310 I=1,4
310 C(I)=0.0
c   contact breaks
      DFLAG=RDIF.GT.TOL
      RETURN
      END
C ----- END OF SUBROUTINE ASFORD -----
C*
```

APPENDIX C
USERS' MANUAL FOR ASBAL

USERS' MANUAL FOR ASBAL

ASBAL (version 3.0B) has replaced Kelvin-Voigt Model with Burgers' element as the viscoelastic element for asphalt binder. The executable was compiled using Microsoft Powerstation, a 32 bits Fortran compiler for PCs. The executable can access expended memory and use free hard disk space as virtual memory. Thus, the maximum allowable array for this executable can be larger than that complied by NJIT VAX (Tesla) Fortran.

ASBAL is preferably running in batch mode and the input file is called "asbal3.dat". The output files include: file.out (a detailed output file), file.plt (a summarized list file), asb.ps (a graphical snapshot in postscript format), file.log (a log file tracking the CPU time). A utility file, ASPOST, is used to post-process the summary file, file.plt, in order to produce file.prn for importing into spreadsheet for producing figures.

The input commands, modified from TRUBAL, are presented as follows:

(capital characters may be used as abbreviation of input commands)

COHesion coh itype jtype Acoh Dmin

The cohesion between particles with itype surface and particles with jtype surface is assigned to coh. The cohesion at asphalt binder contacts is assigned to Acoh. Dmin is the minimum distance between two particle surfaces to have asphalt effects. Therefore, Dmin is twice of the thickness of asphalt coating of particles.

Create x y z ize isurf

A sphere is created at location (x, y, z) with size type, isize, and surface type, isurf. A radius must have been defined for size type, isize, by Radius command. ASBAL inherited from TRUBAL to have limitation of 5 size-types and 5 surface-types. Users should be cautious to prevent significant particle overlapping.

Cycle	n	<S0	v>
		<S1MS2	v>
		<S11	v>
		<S22	v>
		<S33	v>
		<RING	v>

It is to perform n calculation cycles under servo-control. Servo-control will keep the specified parameter as a constant:

S0 is corresponding to mean stress which is defined as: $S0 = (S11+S22+S33)/3$.

S1MS2 is mean stress at horizontal plane: $S1MS2 = (S11+S22)/2$

S11, S22, S33 are the principle stresses in x, y, z direction respectively.

RING controls the angle of major principle in a ring shear test.

Physically reasonable combination of the above variables may be used.

Damping frac freq imass istiff

Damping is specified in terms of the Rayleigh damping parameters: frac is the fraction of critical damping at the model frequency freq. Rayleigh damping involves mass-

proportional damping (set imass as 0) and stiffness-proportional damping (set istiff as 0). Stiffness-proportional damping requires a reduction in time-step for numerical stability. One should not be confused the damping to achieve numerical stability with the dashpots in Burgers element.

Density d isize

d is taken as the mass-density of all particles of size type, isize.

Fix ix iy iz irx iry irz iadd

All

The translational or angular velocity of any particle may be held constant by setting the appropriate parameter equal to 1: ix, iy, and iz control the x, y, and z velocities, and irx, iry, and irz the angular velocities about the x, y, and z axes, respectively. The restraints may be removed by setting the parameters to zero. The final parameter, iadd, is the address of the particle to be fixed. If the word, All, is substituted, then all particles are affected. Users should be aware of that only Zero command can set velocities to zero.

FRAction f

The fraction of critical time-step is set to f. The critical time-step is calculated on the basis of one particle, acted on by one set of linear normal and shear springs given by Normal and Shear commands. The smallest mass and largest stiffness are used. However, in a real assembly, each particle is acted on by several springs. To allow for this increase in

apparent stiffness, the critical time-step is reduced by factor f , which is typically taken as 0.05. If numerical instability is suspected, f should be reduced even further.

Friction **amu** **isurf** **jsurf** **asmu**

The friction coefficient between surface types **isurf** and **jsurf** is set to **amu**. The friction coefficient between asphalt binders is set to **asmu**.

GAIN **g** **edmax**

The servo gain, g , and the maximum allowed strain-rate, $edmx$, are set. In mode 0, the parameter g represents $\Delta\dot{\epsilon}/\sigma_{error}$, where $\Delta\dot{\epsilon}$ is the change in grid strain-rate that occurs for an error in the controlled stress of σ_{error} . The “controlled stress” is the one given on the Cycle command, and the “error” is the difference between the given value and the measured value for the assembly of particles. For mode 1 operation, the parameter g is $\dot{\epsilon}/\sigma_{error}$. The optimum value of g is obtained by try-and-error.

GENerate **n** **isize** **isurf**

Seed **n**

n particles of size **isize** and surface type **isurf** are generated randomly over the whole volume of periodic space. No effect is made to fit particles into gaps between other particles: if a candidate particle overlaps an existing particle, it is rejected and another one is tried. Before giving this command, a radius must already have been defined for the size type **isize**. If several sizes of particles are to be combined in an assembly, the larger ones

should be generated first, since it is easier to fit small particles into gaps than large particles. If the second form of the command (Gen Seed n) no particles are generated, but the random number generator produces n numbers that are discarded. This is useful when generating different distributions of the same particles.

GRAvity **gx** **gy** **gz**

Gravitational accelerations are prescribed for each of the coordinate directions. Note that gravity is not meaningful when full periodic boundaries are in effect.

GRID **ed11** **ed22** **ed33** **ed12** **ed23** **ed31**

The strain-rates, ed11, ed22, ed33, ed12, ed23, and ed31 of periodic space are set. Note that the strain-rates ed23 and ed31 are not used. The components ed11, ed22 and ed33 caused the periodic volume to change shape. However, the component ed12 does not distort the periodic volume in shear, rather, there is a step in x or z displacement between the bottom y-boundary and top y-boundary. This step in shear is printed out when the Print Grid command is given.

HERTZ **gmod** **poiss** **isize**

This command use a non-linear contact law, based on the Hertz-Mindlin theory. Parameter gmod is the shear modulus and poiss is the Poisson's ratio of the solid material of the particles. These properties are for particles of size-type isize. Both normal stiffness

and shear stiffness depend on normal force in a non-linear manner, but partial sliding is not modeled.

The time-step calculation does not recognize the Hertz contact formulation, therefore shear and normal stiffnesses should be given that correspond to the equivalent Hertz-contact stiffnesses at the prevailing stress level. These linear stiffnesses are only used to compute the time-step, but not used in the mechanical calculation when Hertz mode is in effect.

Iset k iadd

The integer k is inserted into the main memory array IA() at address iadd. Great caution is needed when using this command.

Log On
OFF

The command Log On cause all commands, comments, error messages to be reproduced in a file: filename.out. The command, Log OFF suppress this echo function, except for output from the Print command.

Mode n

This selects the type of servo control. Mode 0, which is the default, selects “velocity increment control,” in which the increment in grid velocity is proportional to the error (difference between measured value and desired value). Mode 1 selects “velocity

control,” whereby the grid velocity is set directly by the servo. In mode 0, however, ignores any strain-rate that may have been given: it is useful for getting to an equilibrium condition of zero velocity. In such a case the mode 0 servo would be unsatisfactory because it would continue to “hunt”, without coming to final equilibrium.

New

The program returns to the point at which it expects a Start or Restart command. The data for the current problem is lost from memory.

NOrmal akn isurf jsurf askn1 lamn1 askn2 lamn2

The normal stiffness of particles is set to akn between two particles of surface types isurf and jsurf. The Burgers parameter (in normal direction) for asphalt binder are set to: askn1, lamn1, askn2, and lamn2 for E1, V1, E2, and V2, respectively.

Plot BOund

Disks

Forces

Rdisp

ROtation

Save

Velocisty

Wall

WCap

The plot command produces plots of the x-y plane. The “plots” are in the form of PostScript directives in files called filename.ps. This file is sent to a postscript laser printer. Users can also view and/or print this file using a shareware, GhostScript, which is a PostScript file interpreter.

Each Plot command produces one plotted page. Parameter Bound produces a plot of the boundary of periodic space. Shaded circles are plotted with the Disks parameter. The force parameter produces a series of lines that corresponds to contact forces, where line thickness is proportional to force magnitude. The Save parameter does not produce a plot, but it causes the current state to be saved in a memory buffer; this saved state is necessary before using parameters Rdisp and Rotation, which produce, respectively, plots of relative displacement and relative rotation. The parameter Vel causes velocity vectors to be plotted. The final two parameters, Wall and Wcap, are described under the command Wall.

PRint	Balls
	CHist
	Contacts <All>
	<Gap>
	Entries
	Grid
	Info

Map

Partitions

Stress

Printout is made of various parameters; the above correspond, respectively, to: balls, contact histogram, contacts, box entries, gird size, general information, memory map, stress partitions, and stress tensor. The optional keyword All requests that all contacts are printed, rather than just those taking load, which is the default. The optional keyword Gap causes only contact overlaps and normal forces to be printed. Several keywords may be given on the same line. To reduce the amount of output, the Window command may be given prior to the Print command.

PRObe E11

E22

E33

E12

E23

E31

E1M2

E2M3

E3M1

This command causes an strain increment to be made at the current state. The resulting modulus is printed out. Only one of the above keywords may be given per Probe

command: they correspond, respectively, to probes of E11, E22, E33, E12, E23, E31, E1M2, E2M3, and E3M1. The current state is saved before the probe is done, and restored afterwards. During the probe, 500 cycles of zero strain are done.

RAdius **r** **isize**

r is taken as the radius of particles of size type isize.

REset

Accumulated rotations are set to zero. This has no effect on the mechanical behavior, since only increment rotations are used in this calculation. Note that the rotations are simply the summations, over time, of the incremental rotations. They have no physical meaning, since the three components of rotation do not constitute a vector.

Restart **<filename>**

A previous-saved problem is restored from the file filename. If a file name is not given, a default file name of save.sav is assumed. The command Restart may only be given as the first command of a run or as the first command after a New command.

Rset **r** **iadd**

The real number r is inserted into the main memory array IA() at address iadd. Great caution is needed when using this command.

SAve <filename>

The current problem state is saved in the file filename. If a file name is not given, a default file name of save.sav is assumed. If a file name is specified that already exists, the existing data is over-written. The saved state records all positions, velocities, forces, options, options and so on, at a given stage in a run; it corresponds to a “snapshot” a single point in time. The Save command does not record a sequence of commands.

SHear aks isurf jsurf aks1 lams1 aks2 lams2

The shear stiffness is set to aks for contact between two particles of surface types isurf and jsurf. The Burgers parameters in the tangential direction are: aks1, lams1, aks2, and lams2 for E1, V1, E2, and V2, respectively.

Start xmax ymax zmax nbox nball nwall <log>

This command must be the first one given in a input file. The parameters xmax, ymax, and zmax are the total widths of the box volume (as well as the periodic volume) in the x, y, and z directions, respectively. nbox is the number of boxes requested, and nball is the maximum number of particles that may be needed. There is no problem if fewer particles are subsequently generated and the purpose of the Start command is to allocate enough memory to hold all the required boxes and particles. The parameter nwall is not used at present, and should be set to zero. The optional keyword Log turns the “log” facility on immediately: i.e. output is echoed to the output file.

Stop

The program stops. The current state of the problem is not saved automatically.

WALL	Gain	g
	Nstress	sig
	Pos	ybot ytop
	Vel	vmax
	Xvel	xvbot xvtop

This command sets up two sheets of particles that are controlled in velocity: they resemble rough walls. The “walls” are perpendicular to the y axis, and can be given x velocities in order to do a shear test. The y velocities are controlled by a servo-mechanism so as to keep the average normal stress on the walls constant. Before the first Wall command is given, a stable, compacted sample must exist. The lower (low-y) and upper (high-y) wall positions are specified, respectively, by ybot and ytop, following the keyword Pos. All particles that are intersected by the two planes (at $y = ybot$ and $x = ytop$) are captured by the walls, and are controlled in any subsequent tests. Particles above the top wall and below the bottom wall are marked as inactive during the calculation cycle. The positions of the two planes may be plotted by the Plot Wall command, and in 2-D mode, the controlled particles may be plotted by the Plot Wcap command, which plots white circles rather than shaded circles. Keyword Xvel is used to specify the x velocities of the lower and upper walls: xvbot and xvtop, respectively. The servo control resembles that described under commands Cycle and Gain; for the wall servo, gain is specified as g,

following the Gain keyword, and the limit to velocity is vmax, following the vel keyword. The wall servo operates in velocity-increment mode. Currently, the wall is not used in ASBAL.

Window **x1** **x2** **y1** **y2** **z1** **z2**

This command limits the volume of space that is addressed by the Print command, when it is printing out information on particles, contacts, etc.

Zero

Translational velocities of all particles are set to zero.

2-D

This command causes the program to operate in two-dimensional mode. The particles are still regarded as spheres, but they are constrained to move in the x-y plane only. Although the equations of motion are truncated to two dimensions, the force-displacement calculation still operates in three dimensions. This could be modified, to improve the same value, corresponding to the center of the box volume in the x direction. Only one box should be specified in the z direction.

APPENDIX D
SAMPLE INPUT FILES FOR ASBAL

Example 1. 150-particle test under constant mean stress

```

START 200 200 200 27 152 0 LOG
85a for asbal3c, uniaxial, recompact
RAD 10 1
RAD 15 2
GEN 50 2 1
GEN 100 1 1
SH 1E8 1 1 2E6 2E5 2E4 2E2
NO 2E8 1 1 2E6 2E5 2E4 2E2
FRIC 1 1 1 0
COHE 0 1 1 1E5 0.4 1.0
DAMP .5 .25 0 0
DENS 1000 1
DENS 1000 2
FRAC 0.05
GRID -2E-2 -2E-2 -2E-2 0 0 0
C 200
PR G I S
*SAVE S1.SAV
C 200
PR G I S
C 200
PR G I S
C 200
PR G I S
C 200
stop
GRID -1E-2 -1E-2 -1E-2 0 0 0
*SAVE S1.SAV
PR G I S
C 200
PR G I S
C 200
PR G I S
C 200
PR G I S
C 200
PR G I S
C 200
PR G I S

```

```

C 200
*SAVE S2.SAV
GRID -5E-3 -5E-3 -5E-3 0 0 0
PR G I S
C 200
PR G I S
C 200
PR G I S
C 200
PR G I S
C 200
PR G I S
C 200
*SAVE S3.SAV
PR G I S
C 200
PR G I S
*
* NOW RELAX
*
GRID 0 0 0 0 0 0
C 200
* PR G I S
C 200
*PR G I S
C 200
*SAVE S4.SAV
*PR G I S
C 200
* PR G I S
C 200
*PR G I S
FRIC .1 1 1 0
C 200
*PR G I S
C 200
*PR G I S
C 200
FRIC 1 1 1 0

```

```

C 200
*PR G I S P
*SAVE STATE1.SAV
*stop
*finish compaction
*start the test
PR G I S
*print starting condition
GAIN 5E-8 3E-3
*plot save
GRID 0 0 -1E-3 0 0 0
C 200 S0=-2.00E5
PR G I S
*plot bound rdis rota
*plot bound disks
*plot bound disks vel
*save temp.sav
*stop
C 200 S0=-2.00E5
PR G I S
C 200 S0=-2.00E5
PR G I S
C 200 S0=-2.00E5
PR G I S
C 200 S0=-2.00E5
PR G I S
*SAVE S5.SAV
*
* 6000 CYC
*
C 200 S0=-2.00E5
PR G I S
C 200 S0=-2.00E5
PR G I S
C 200 S0=-2.00E5
PR G I S
C 200 S0=-2.00E5
PR G I S
C 200 S0=-2.00E5

```



```
PR G I S
stop
*
* 7000 CYC
*
C 200 S0=-2.00E5
PR G I S
C 200 S0=-2.00E5
PR G I S
C 200 S0=-2.00E5
PR G I S
C 200 S0=-2.00E5
PR G I S
C 200 S0=-2.00E5
PR G I S
*
* 8000 CYC
*
C 200 S0=-2.00E5
PR G I S
C 200 S0=-2.00E5
PR G I S
C 200 S0=-2.00E5
PR G I S
C 200 S0=-2.00E5
PR G I S
C 200 S0=-2.00E5
PR G I S
*
* 9000 CYC
*
C 200 S0=-2.00E5
PR G I S
C 200 S0=-2.00E5
PR G I S
C 200 S0=-2.00E5
PR G I S
C 200 S0=-2.00E5
PR G I S
```

```

C 200 S0=-2.00E5
PR G I S
*
* 10000 CYC
*
C 200 S0=-2.00E5
PR G I S
C 200 S0=-2.00E5
PR G I S
C 200 S0=-2.00E5
PR G I S
*
* CHECK EQUILIBRIUM
*
*GRID 0 0 0 0 0 0
C 200 S0=-2.00E5
PR G I S
*SAVE STATE2.SAV
*
* NOW UNLOAD
*
*GRID 0 0 1E-3 0 0 0
C 200 S0=-2.00E5
PR G I S
*
* 11000 CYC
*
C 200 S0=-2.00E5
PR G I S
C 200 S0=-2.00E5
PR G I S
C 200 S0=-2.00E5
PR G I S
C 200 S0=-2.00E5
PR G I S
C 200 S0=-2.00E5
PR G I S
*
* 12000 CYC

```

```

*
C 200 S0=-2.00E5
PR G I S
C 200 S0=-2.00E5
PR G I S
C 200 S0=-2.00E5
PR G I S
C 200 S0=-2.00E5
PR G I S
C 200 S0=-2.00E5
PR G I S
*
* 13000 CYC
*
*plot save
*save temp2.sav
*stop
C 200 S0=-2.00E5
PR G I S
*plot rdis rota
*stop
C 200 S0=-2.00E5
PR G I S
C 200 S0=-2.00E5
PR G I S
*
* CHECK EQUILIBRIUM
*
*GRID 0 0 0 0 0 0
C 200 S0=-2.00E5
PR G I S
*SAVE STATE3.SAV
*
* NOW RE-LOAD
*
*GRID 0 0 -1E-3 0 0 0
C 200 S0=-2.00E5
PR G I S
*

```

```
* 14000 CYC
*
C 200 S0=-2.00E5
PR G I S
C 200 S0=-2.00E5
PR G I S
C 200 S0=-2.00E5
PR G I S
C 200 S0=-2.00E5
PR G I S
C 200 S0=-2.00E5
PR G I S
C 200 S0=-2.00E5
PR G I S
*
* 15000 CYCLES
*
C 200 S0=-2.00E5
PR G I S
C 200 S0=-2.00E5
PR G I S
C 200 S0=-2.00E5
PR G I S
C 200 S0=-2.00E5
PR G I S
C 200 S0=-2.00E5
PR G I S
C 200 S0=-2.00E5
PR G I S
*
* 16000 CYC
*
C 200 S0=-2.00E5
PR G I S
C 200 S0=-2.00E5
PR G I S
C 200 S0=-2.00E5
PR G I S
C 200 S0=-2.00E5
PR G I S
C 200 S0=-2.00E5
PR G I S
C 200 S0=-2.00E5
PR G I S
*
```

```
* 17000 CYC
*
C 200 S0=-2.00E5
PR G I S
C 200 S0=-2.00E5
PR G I S
C 200 S0=-2.00E5
PR G I S
C 200 S0=-2.00E5
PR G I S
C 200 S0=-2.00E5
PR G I S
*
* 18000 CYC
*
C 200 S0=-2.00E5
PR G I S
C 200 S0=-2.00E5
PR G I S
C 200 S0=-2.00E5
PR G I S
*SAVE STATE4.SAV
STOP
```

Example 2. 512-particle test to simulate Lee & Dass (1992)

```

START 50 50 100 16 514 0 LOG
88g3, one size, compact to 1X2
*simulate Lee&Dass, 1992
RAD 3 1
GEN 512 1 1
SH 1E8 1 1 2E1 2E1 2E1 2E1
NO 2E8 1 1 2E1 2E1 2E1 2E1
FRIC 0.7 1 1 0.0
COHE 0 1 1 0.0
DAMP .5 .25 0 0
DENS 2230 1
FRAC 0.05
*start compaction
*save ini.sav
*stop
GRID -1E-1 -1E-1 -5E-2 0 0 0
C 200
PR G I S
C 200
PR G I S
C 200
PR G I S
C 200
PR G I S
C 200
PR G I S
C 200
PR G I S
*
* 1000 CYC
*
*SAVE S1.SAV
GRID 0 0 -1.5E-2 0 0 0
C 200
PR G I S
C 200
PR G I S
C 200
PR G I S

```

```
C 200
PR G I S
C 200
PR G I S
*SAVE S2.SAV
c 200
PR G I S
C 200
PR G I S
C 200
PR G I S
C 200
PR G I S
*save temp.sav
grid 0 0 0 0 0 0
C 200
PR G I S
*stop
C 200
PR G I S
C 200
PR G I S
FRIC 0.05 1 1 0
C 200
PR G I S
C 200
PR G I S
*SAVE S4.SAV
C 200
PR G I S
FRIC 0.7 1 1 0
C 200
PR G I S
C 200
PR G I S
C 200
PR G I S
C 200
PR G I S
```

```

C 200
PR G I S
*save compact.sav
*stop
*rest compact.sav
*matching Lee's strain level
GAIN 5E-8 3E-3
SH 1.25E8 1 1 2E9 2E7 2E5 2E5
NO 2.5E8 1 1 2E9 2E7 2E5 2E5
COHE 0 1 1 1E5 0.4
FRIC 0.7 1 1 0
*PR G I S
*start the simulation
GRID 1.85E-3 1.85E-3 -3E-3 0 0 0
C 200
PR G I S
*start test
C 200
PR G I S
C 200
PR G I S
C 200
PR G I S
C 200
PR G I S
*SAVE S5.SAV
*
* 6000 CYC
*
C 200
PR G I S
C 200
PR G I S
C 200
PR G I S
C 200
PR G I S
C 200
PR G I S
C 200
PR G I S
C 200
PR G I S

```



```
*
* 7000 CYC
*
C 200
PR G I S
C 200
PR G I S
C 200
PR G I S
C 200
PR G I S
C 200
PR G I S
C 200
PR G I S
*
* 8000 CYC
*
C 200
PR G I S
C 200
PR G I S
C 200
PR G I S
C 200
PR G I S
GRID 1.97E-3 1.97E-3 -3E-3 0 0 0
C 200
PR G I S
*
* 9000 CYC
*
C 200
PR G I S
C 200
PR G I S
C 200
PR G I S
C 200
PR G I S
C 200
```

PR G I S

*

* 10000 CYC

*

C 200

PR G I S

C 200

PR G I S

C 200

PR G I S

C 200

PR G I S

*SAVE STATE2.SAV

C 200

PR G I S

*

* 11000 CYC

*

C 200

PR G I S

C 200

PR G I S

C 200

PR G I S

C 200

PR G I S

C 200

PR G I S

*

* 12000 CYC

*

C 200

PR G I S

GRID 1.97E-3 1.97E-3 -3E-3 0 0 0

C 200

PR G I S

C 200

PR G I S

C 200

```
PR G I S
C 200
PR G I S
*
* 13000 CYC
*
C 200
PR G I S
C 200
PR G I S
C 200
PR G I S
C 200
PR G I S
*SAVE STATE3.SAV
C 200
PR G I S
*
* 14000 CYC
*
C 200
PR G I S
C 200
PR G I S
C 200
PR G I S
C 200
PR G I S
C 200
PR G I S
*
* 15000 CYCLES
*
C 200
PR G I S
C 200
PR G I S
C 200
PR G I S
```

C 200
PR G I S
C 200
PR G I S
*
* 16000 CYC
*
C 200
PR G I S
C 200
PR G I S
C 200
PR G I S
C 200
PR G I S
GRID 1.55E-3 1.55E-3 -3E-3 0 0 0
C 200
PR G I S
*
* 17000 CYC
*
C 200
PR G I S
C 200
PR G I S
C 200
PR G I S
C 200
PR G I S
C 200
PR G I S
*
* 18000 CYC
*
C 200
PR G I S
C 200
PR G I S
C 200

```
PR G I S
C 200
PR G I S
GRID 1.5E-3 1.5E-3 -3E-3 0 0 0
C 200
PR G I S
*
* 19000 CYC
*
C 200
PR G I S
C 200
PR G I S
C 200
PR G I S
C 200
PR G I S
C 200
PR G I S
*
* 20000 CYC
*
C 200
PR G I S
C 200
PR G I S
C 200
PR G I S
C 200
PR G I S
C 200
PR G I S
*
* 30000 CYC
*SAVE STATE4.SAV
STOP
```

APPENDIX E
METHOD OF MICROMECHANICAL LABORATORY TESTS FOR HMA

METHOD OF MICROMECHANICAL LABORATORY TESTS FOR HMA

Lee and Dass (1993) performed micromechanical laboratory tests to characterize and quantify actual packing structures of HMA. This research is performed in Tyndall Air Force Base. This experimental method uses X-ray computerized tomography (CT) machine to non-intrusively acquire data on the internal packing structures of HMA. Three-dimensional reconstruction algorithms were developed to accurately identify the packing structures of laboratory-packed mixture samples of glass beads and asphalt.

CT Machine and 3D Scanning

The CT work was performed at Oak Ridge National Laboratory (ORNL), Oak Ridge, Tennessee. The CT machine is a high-resolution industrial CT device, CITA Model 101B+, manufactured by Scientific Measurement System (SMS), Inc. The CT machine uses a 420 KeV X-ray source with spatial resolution ranging from 0.002 to 0.04 inch and is capable of resolving density differences as low as 0.25 %.

Thirteen images at a spacing of 2 mm were taken using CT. The scanning was performed within the middle portion of the samples (see Figure E.1). Figure E.2 shows the acquired raw CT image of the glass beads with asphalt sample. The image has 752X752 pixels (each pixel is 0.0789 mm square). The ring immediately surrounding the beads is the plastic container. The beads appear to have various diameters because their centers are either above or below the plane of this cross section. Voids between particles appear in black. The halo surrounding each bead is a density smearing effect caused by

spatial resolution of the CT scan. The microstructure of the particles and asphalt films can be extracted by the following numerical algorithms.

Processing 2D CT Images and Reconstruction of 3D Packing Structure

To extract the required information from the 2D CT images, numerical algorithms were developed to detect edge points of particles and asphalt structures. First, the CT images are masked to eliminate numerical artifacts and the plastic container. Then, the histograms of CT images are plotted to represent more accurately the pixel value profile of the sample.

Numerical algorithms such as first order derivative and second order derivative analysis can be used to determine the edges among particles, asphalt and voids. Since the pixel values are directly related to the density values of the materials being scanned at a particular cross section, the gradients of the pixel values are evaluated to detect the edge of a particle. Therefore, the threshold values for edges can be obtained by above methods (see Figure E.3).

Threshold values identify edge points and object types (particles, asphalt, or voids). A numerical method can identify individual objects by considering a set of equally spaced lines (e.g. 2 pixels or 0.16 mm) cutting cross the image. Line segments cutting through objects are collected. Calculation of the distances and corresponding spatial gradients between two adjacent edge points is performed. Tracking changes in calculated distances and gradients to group the line segments within the same object are carried out (see Figure E.4).

Edge points of individual objects can be evaluated numerically to their locations and sizes (see Figure E.5). Since a 2 mm scanning spacing is $1/3$ of the bead diameter, it is ensured that each glass bead would appear in at least two consecutive CT images. The scanning is performed for the middle 24 mm portion of the sample. A numerical algorithm is applied to each of the thirteen CT images to calculate x-y coordinates and corresponding sizes of the objects. The locations and sizes of objects can be calculated from these groups of objects in the adjacent CT images. Figure E.6 shows the identification of a particle from a group of circles. Thus, three dimensional information of the sample can be obtained. Figure E.7 shows a 3D view of the reconstructed internal packing structure of the scanned portion of the HMA sample.

The parameters for microscopic modeling can now be quantified by the CT results. The parameters include: sizes and locations of particles (Figure E.8) , thickness of asphalt binder (Figure E.9), and contacts (or coordination number) of asphalt-coated particles (Figure E.10).

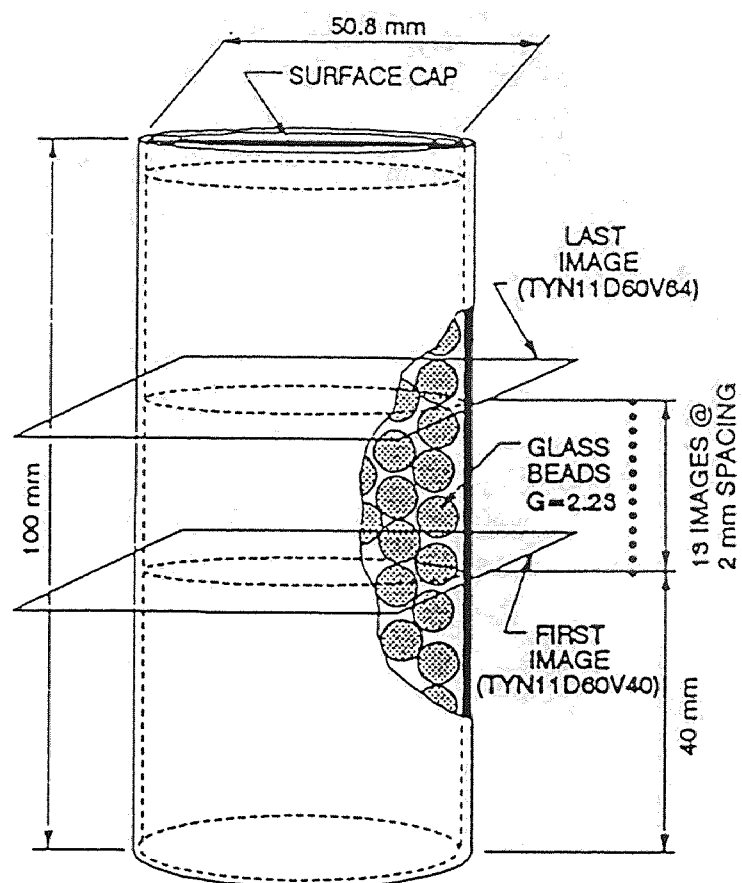


Figure E.1 Dimensions for 3D CT Scanning
(Lee and Dass, 1992)

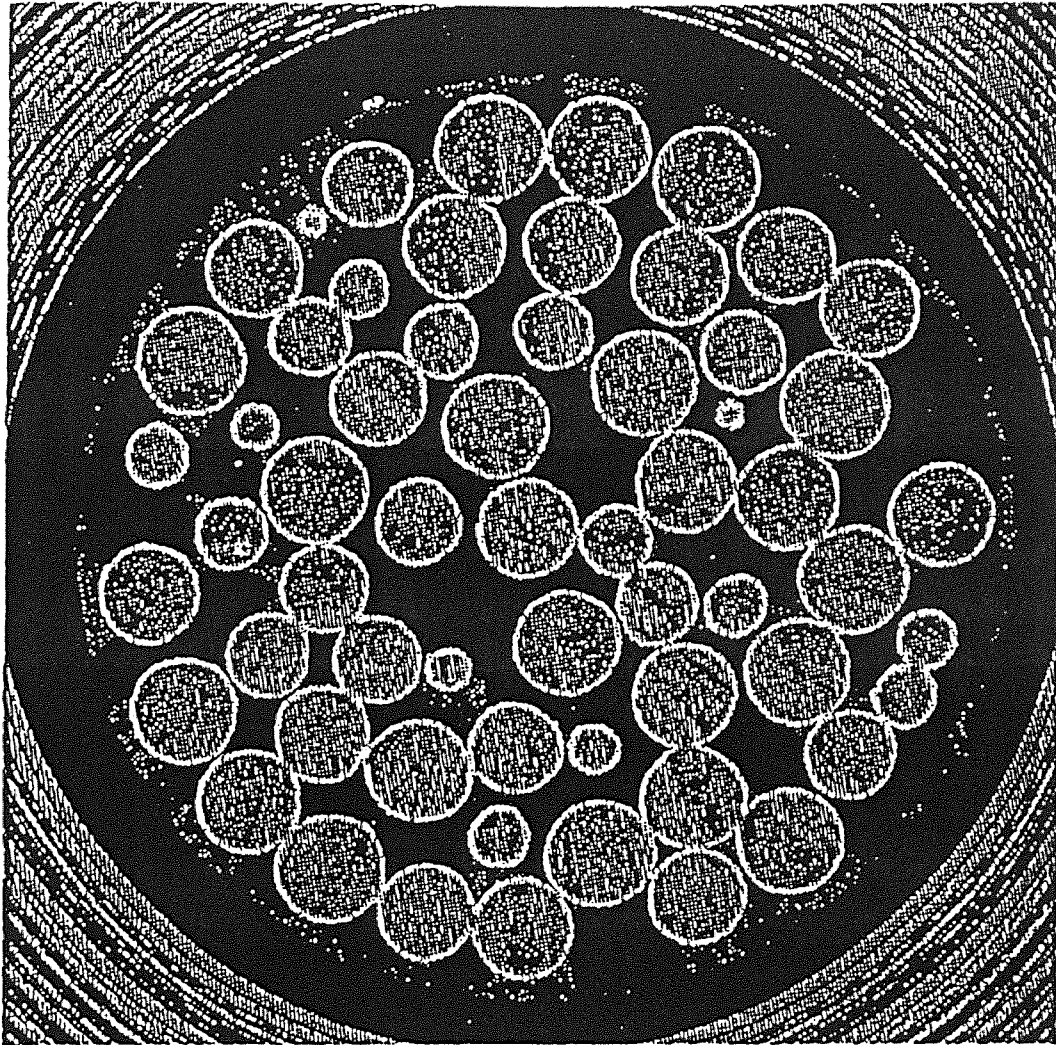
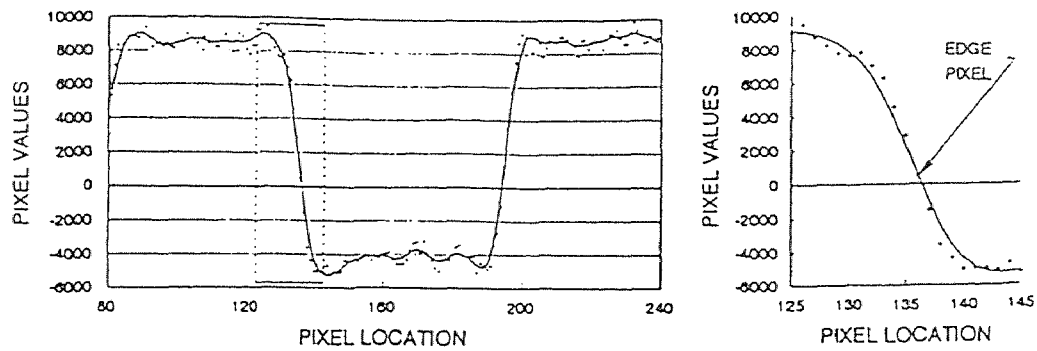
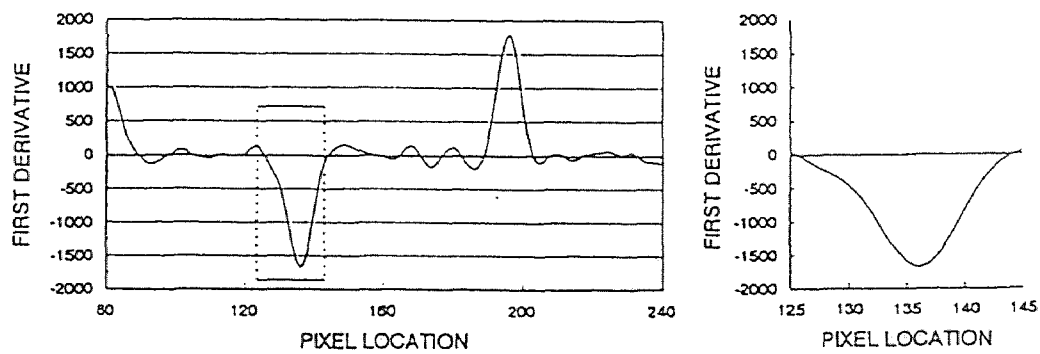


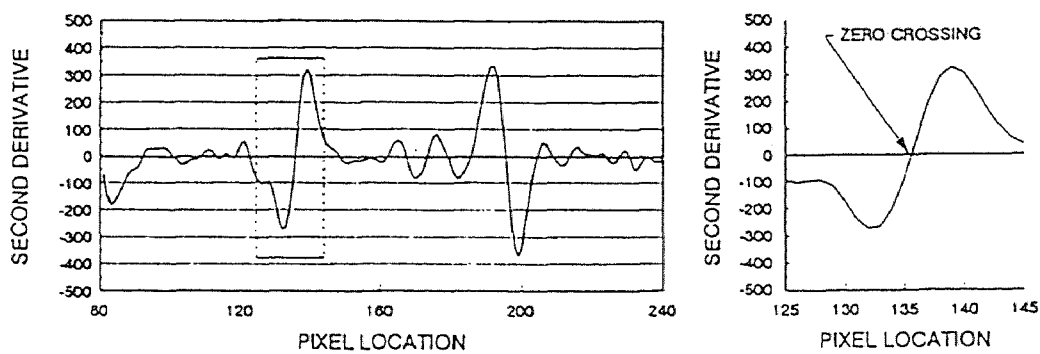
Figure E.2 Raw CT Image of Glass Beads with Asphalt
(Lee and Dass, 1992)



(a) Pixel Value Profile Near the Particle Edges.



(b) First Order Derivative Edge Detection Method.



(c) Second Order Derivative Edge Detection Method.

Figure E.3 Threshold Pixel Values for Edges
(Lee and Dass, 1992)

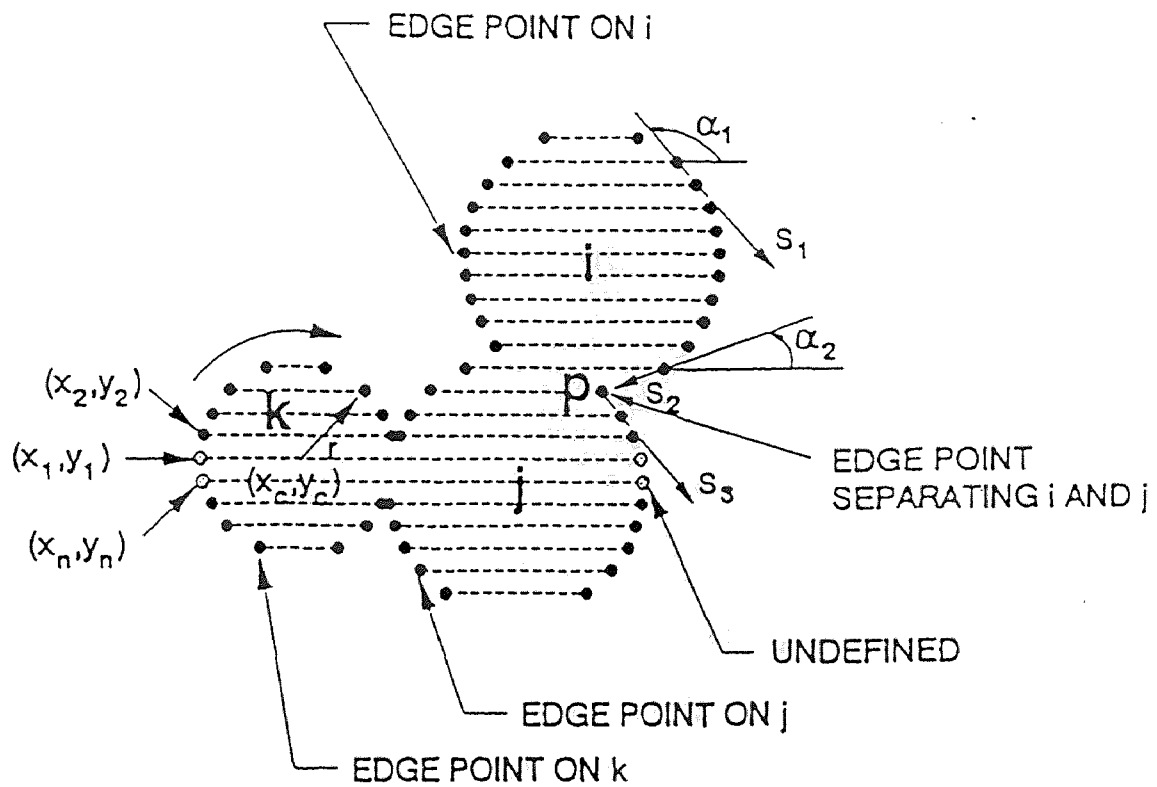


Figure E.4 Identification of Particles from Line Segments
(Lee and Dass, 1992)

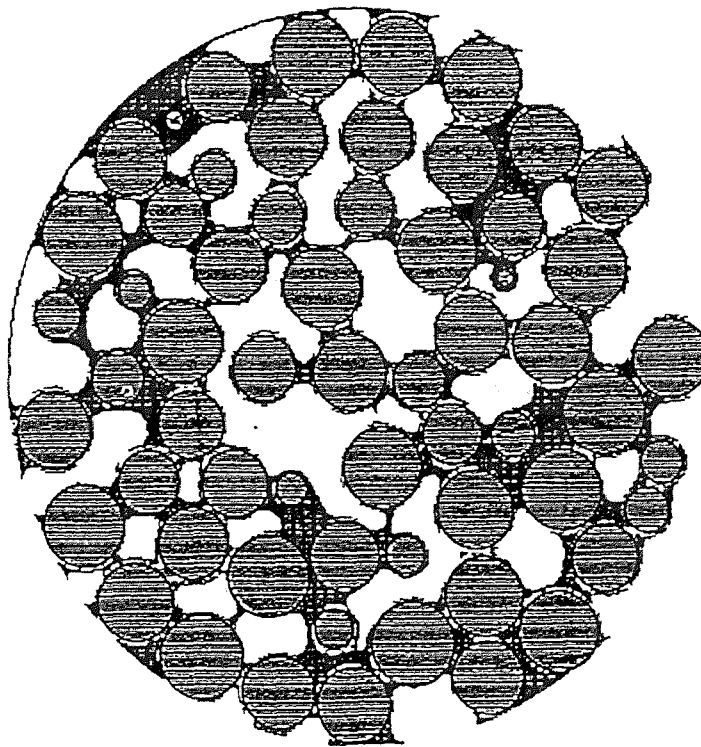
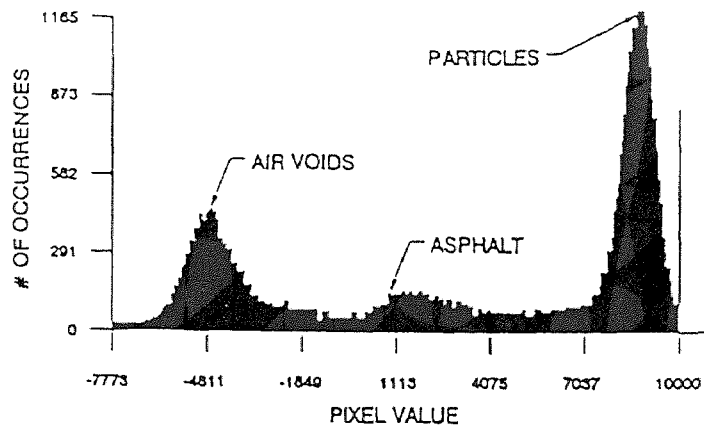


Figure E.5 Pixel Values Histogram of a CT Image and Identification of Particles and Asphalt (Lee and Dass, 1992)

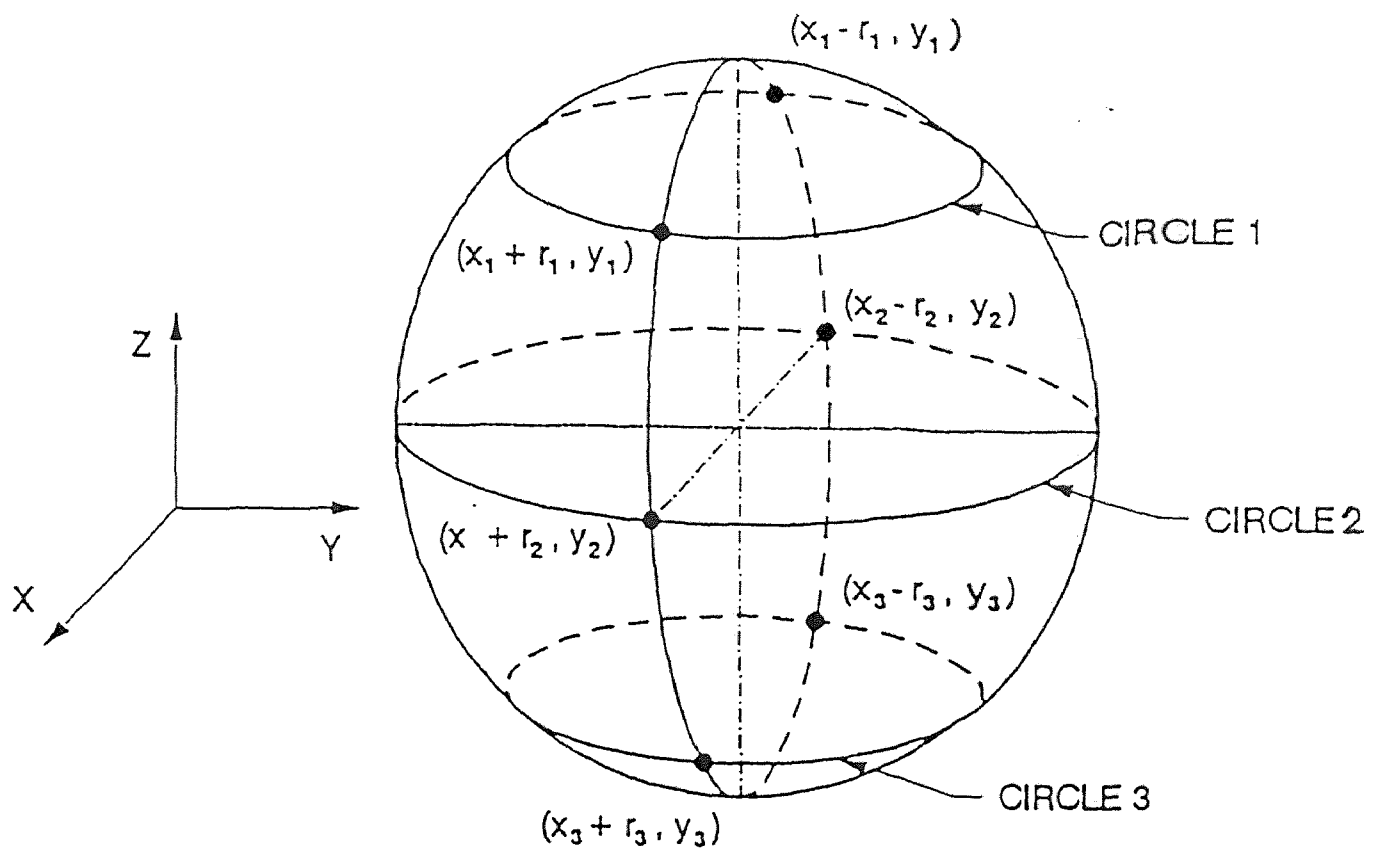


Figure E.6 Identification of a Particle from Adjacent CT Images
(Lee and Dass, 1992)

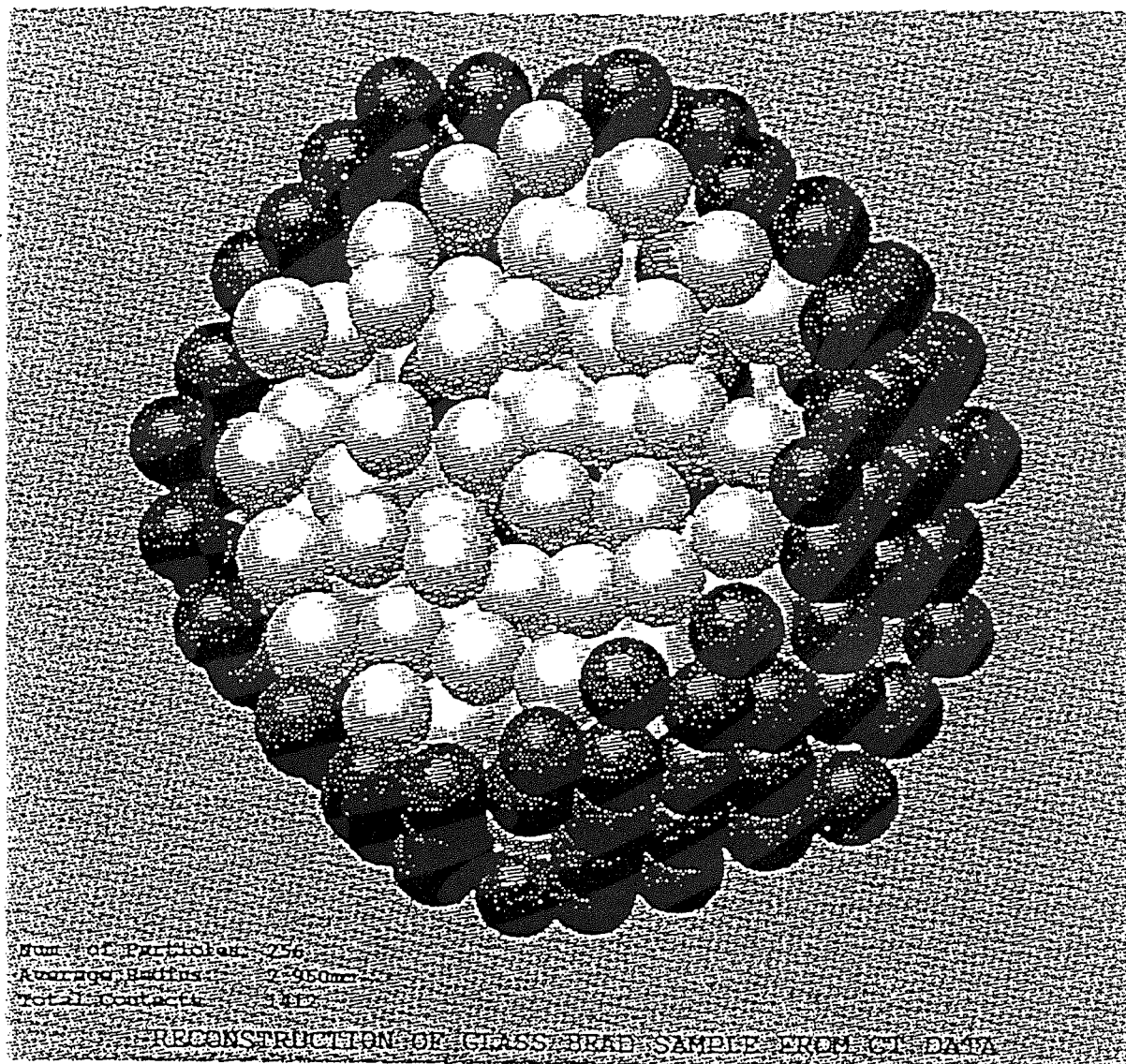
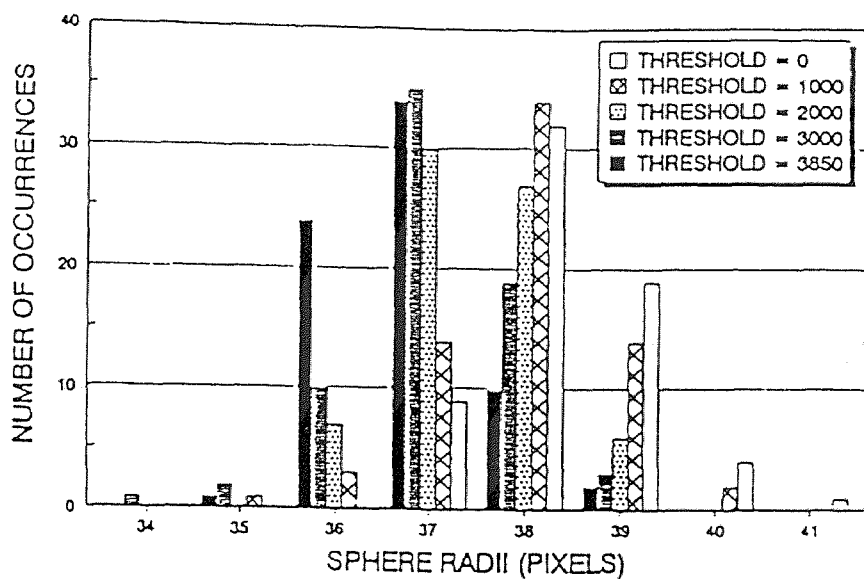
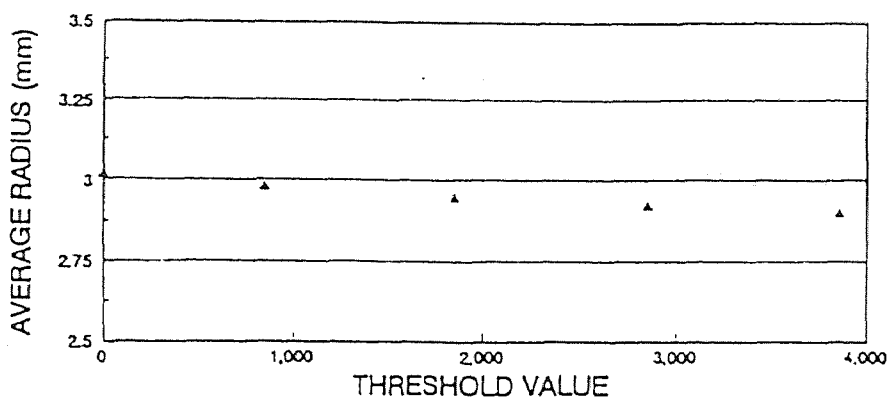


Figure E.7 3D View of the Reconstructed Internal Packing Structure of HMA
(Lee and Dass, 1992)



(a) Bead Radii.



(b) Average Radii.

Figure E.8 Micro-parameters of Particles
(Lee and Dass, 1992)

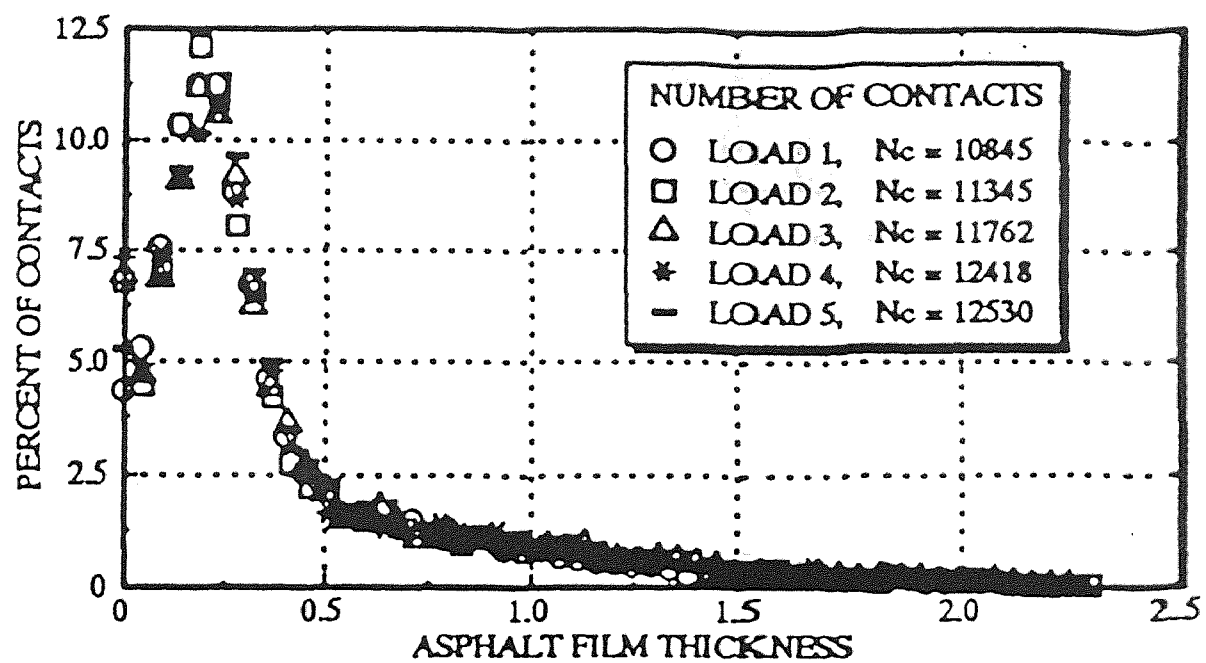
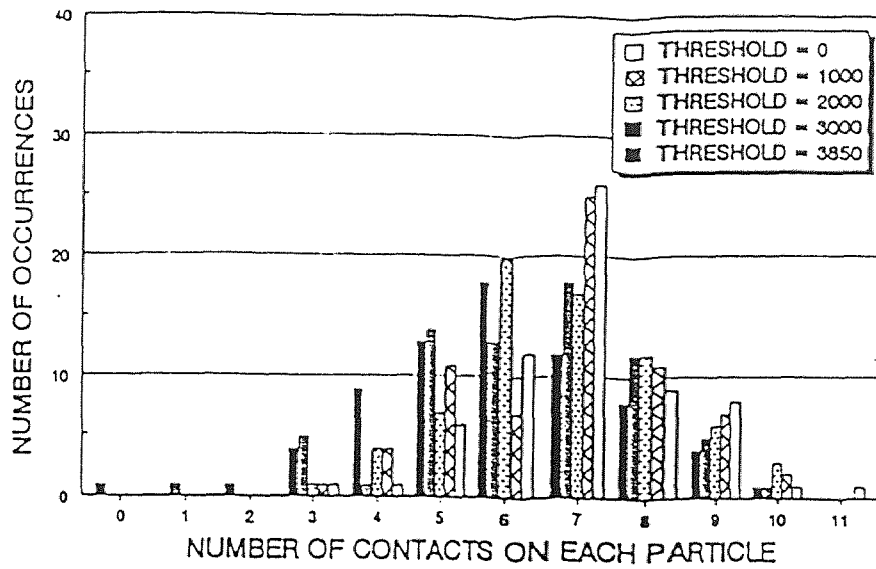
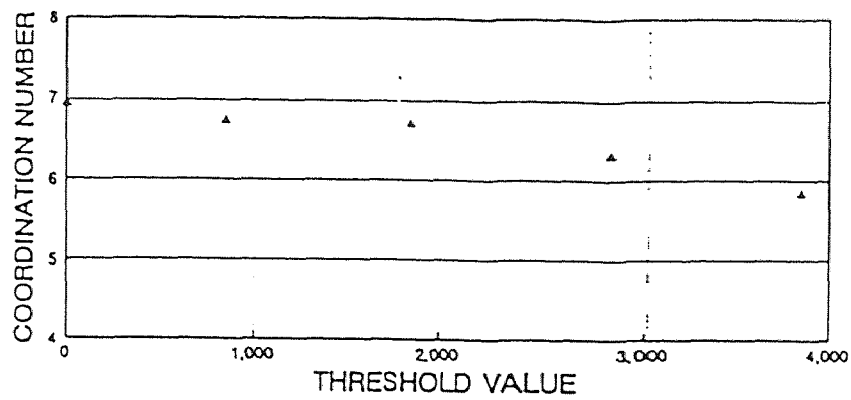


Figure E.9 Asphalt Binder Thickness
(Lee and Dass, 1993)



(a) Distributions.



(b) Average Values.

Figure E.10 Microstructural Parameters: Coordination Number
(Lee and Dass, 1992)

APPENDIX F
TIME-TEMPERATURE SUPERPOSITION THEOREM FOR ASPHALT

TIME-TEMPERATURE SUPERPOSITION THEOREM FOR ASPHALT

SHRP research has developed laboratory tests to characterize asphalt binders. The followings are brief descriptions of the Dynamic Shear Rheometer (DSR) tests, the Bending Beam Rheometer (BBR) tests, construction of master curves, and time-temperature superposition theorem. (Anderson, et al., 1994)

Dynamic Shear Rheometer Tests

The DSR (e.g. Rheometric Mechanical Spectrometer, model RMS-803) applied sinusoidal angular deflections to asphalt binders. The test specimens (1 mm or 2 mm films) are mounted between plates or twisted in torsion (see Figure F.1). At temperatures from 5° to 35°C, 8-mm-diameter parallel plates are used. At temperatures above 35°C, 25-mm-diameter plates are used. At temperatures of 5°C and below, the torsion bar was used.

The DSR testing can generate the following data: applied maximum peak-to-peak strains as a function of time, resulting maximum peak-to-peak torque as a function of time, and the temperature of the lower plate (parallel plates) or oven (torsion bar). Therefore, the following information can be obtained: the complex modulus, the maximum peak-to-peak stress divided by the maximum peak-to-peak strain, the phase angle between the applied strain and the resulting stress.

Figure F.2 shows the phase lag of the stress and strain. The relationship of the complex modulus and phase angle can be expressed as:

$$G^* = \frac{\hat{\tau}}{\hat{\gamma}} = G' + iG'' \quad (\text{F.1})$$

$$G' = |G^*| \times \cos \delta \quad (\text{F.2})$$

$$G'' = |G^*| \times \sin \delta \quad (\text{F.3})$$

where G^* : Complex modulus;

G' : Storage modulus;

G'' : Loss modulus;

τ, γ : Amplitudes of shear stress and strain;

δ : Phase angle.

Energy dissipation is described using $\tan \delta$ which is expressed as:

$$\tan(\delta) = \frac{G''}{G'} \quad (\text{F.4})$$

Because of the temperature dependency of asphalt binder, temperature of specimen should be controlled with an accuracy of at least ± 0.2 °C. The changes of complex modulus with respect to temperature range from 15 to 25 °C for most paving grade asphalt. To comply with linear viscoelastic scheme, a strain sweep test can be used to define the linear viscoelastic region (See Figure F.3). For the case of Figure F.3, limiting shear strain of 13% (or maximum torsion angle, θ , is 46.8°) is determined. The limiting strains for SHRP Core binders are presented in Figure F.4. Therefore, DSR tests can be performed for an asphalt binder at different temperature (See Figure F.5).

Bending Beam Rheometer Tests

BBR was developed to characterize low-temperature rheology of asphalt binders. The technique was based on the guidelines of the ASTM D790 Standard Test Method for

measuring flexural properties of plastics and other elastomers. The specimen is a slender beam (6.25×6.25×125 mm). The device of BBR is illustrated in Figure F.6. The BBR consists of the loading frame unit, temperature-controlled bath, and a data acquisition system. The deflection is measured by a high-precision linear variable differential transformer (LVDT); the load applied is measured by a load cell.

Based on the elasto-viscoelastic correspondence principle, the stress distribution in a viscoelastic beam is the same as that in an elastic beam under the same load. The shear is neglected since the sample is with span-to-depth ratio of 16 to 1. Therefore, the flexural stiffness can be calculated:

$$S(t) = \frac{PL^3}{4bh^3\Delta(t)} \quad (F.5)$$

where $S(t)$: Time-dependent flexural creep stiffness;

$\Delta(t)$: Time-dependent deflection of beam;

P : Applied constant load (100 g);

L : Span length, mm;

b : Width of beam, mm;

h : Depth of beam, mm.

The recommended setup of BBR is as follows: a load of 100 g, stiffness values range between 32.2 MPa at maximum deflection 2.5 mm, and 31,000 MPa at a deflection of 0.0025 mm.

Construction of Master Curves

Using the principle of time-temperature superposition, the results from DSR and BBR tests can be used to produce a master curve for the binder tested. Time-temperature superposition is valid for thermalrheological-simple material such as asphalt binder when tested under linear viscoelastic limits.

The first step to produce a master curve is to determine the reference temperature. Usually, 20°C is used as the reference temperature. This is the temperature to which the stiffnesses obtained at other temperatures are shifted along the frequency axis.

The second step is to determine the shift factor. The shift factors are calculated based on either WLF equation or Arrhenius equation for use of above the defining temperature and below the defining temperature respectively:

WLF equation:

$$\log a(T)_d = \frac{-C_1(T - T_d)}{(C_2 + T - T_d)} \quad (\text{F.6})$$

Arrhenius equation:

$$\log a(T)_d = 2.303 \frac{E_a}{R} \left(\frac{1}{T} - \frac{1}{T_d} \right) \quad (\text{F.7})$$

where $a(T)_d$: The shift factor relative to the defining temperature, T_d ;

C_1, C_2 : Empirical determined constant;

T : The selected temperature, °C;

T_d : The defining temperature, °C.

E_a : The activation energy for flow below T_d ;

R : The ideal gas constant, 8.34 J/mol-°K.

The defining temperature can be obtained from a full dynamic characterization combined with nonlinear least squares analyses. The shift factors of SHRP core asphalt are presented in Figure F.7.

Therefore, master curve can be produced by shifting the data curves obtained at different temperatures along the frequency axis. Figures F.8 and F.9 are examples of master curves from DSR and BBR data respectively.

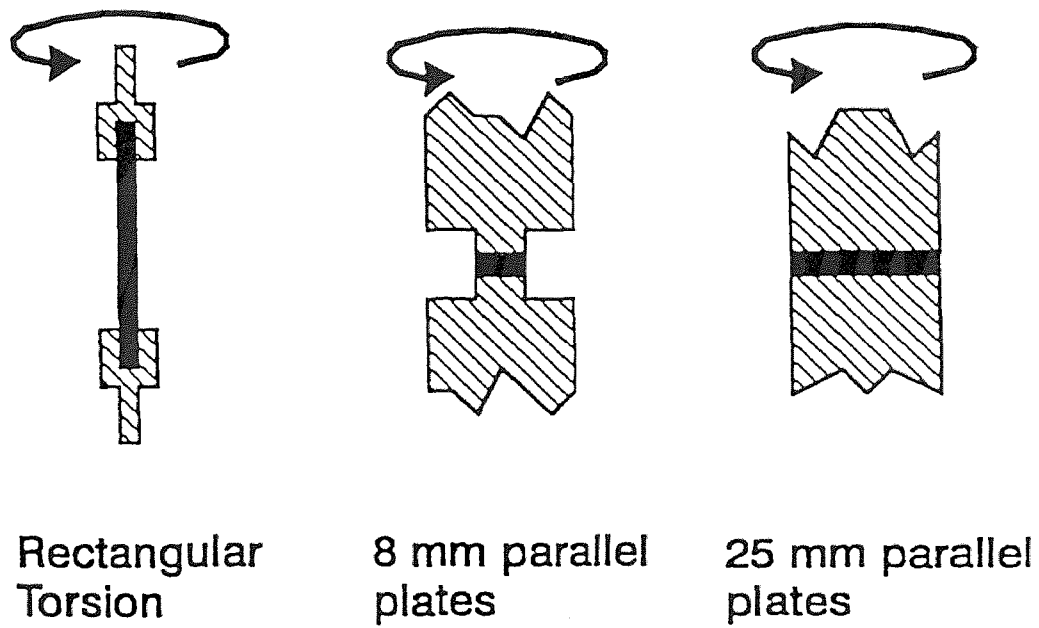


Figure F.1 Parallel Plate and Torsion Bar used for Dynamic Shear Tests
(Anderson, et al., 1994)

Viscoelastic: $0 < \delta < 90^\circ$

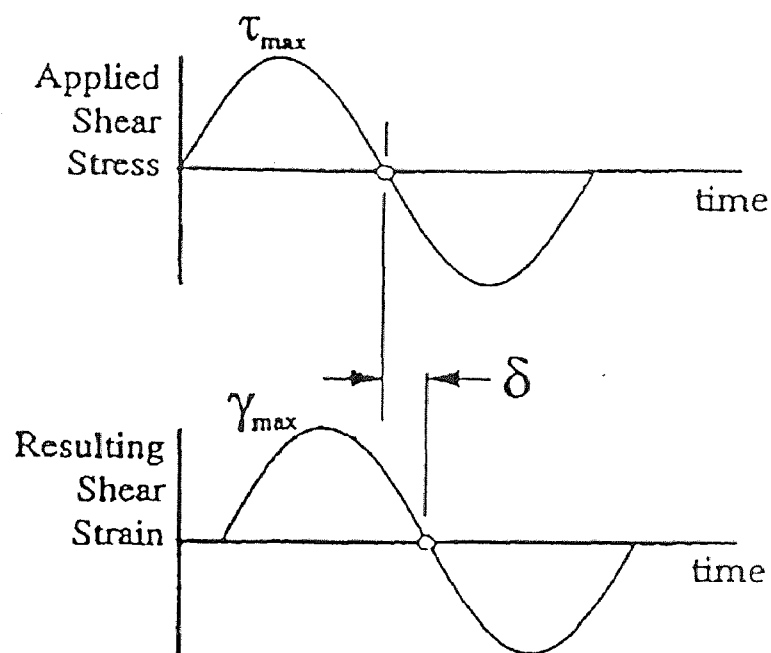


Figure F.2 The Phase Lag in Dynamic Shear Rheometer Tests

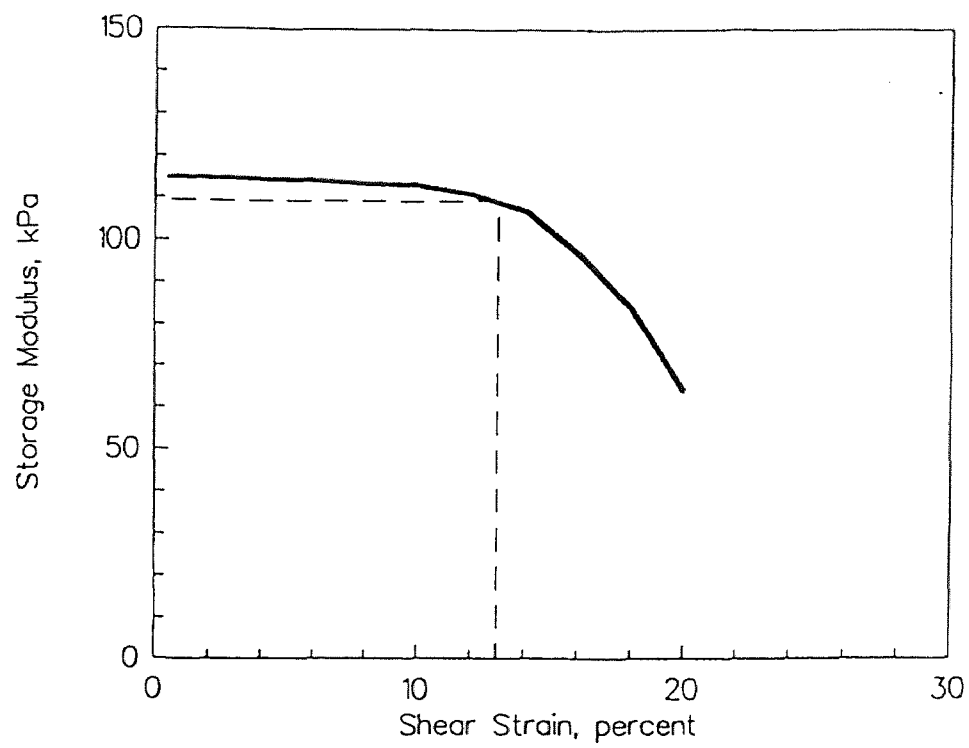


Figure F.3 Strain Sweep Tests to Determine Linear Viscoelastic Limits
(Anderson, et al., 1994)

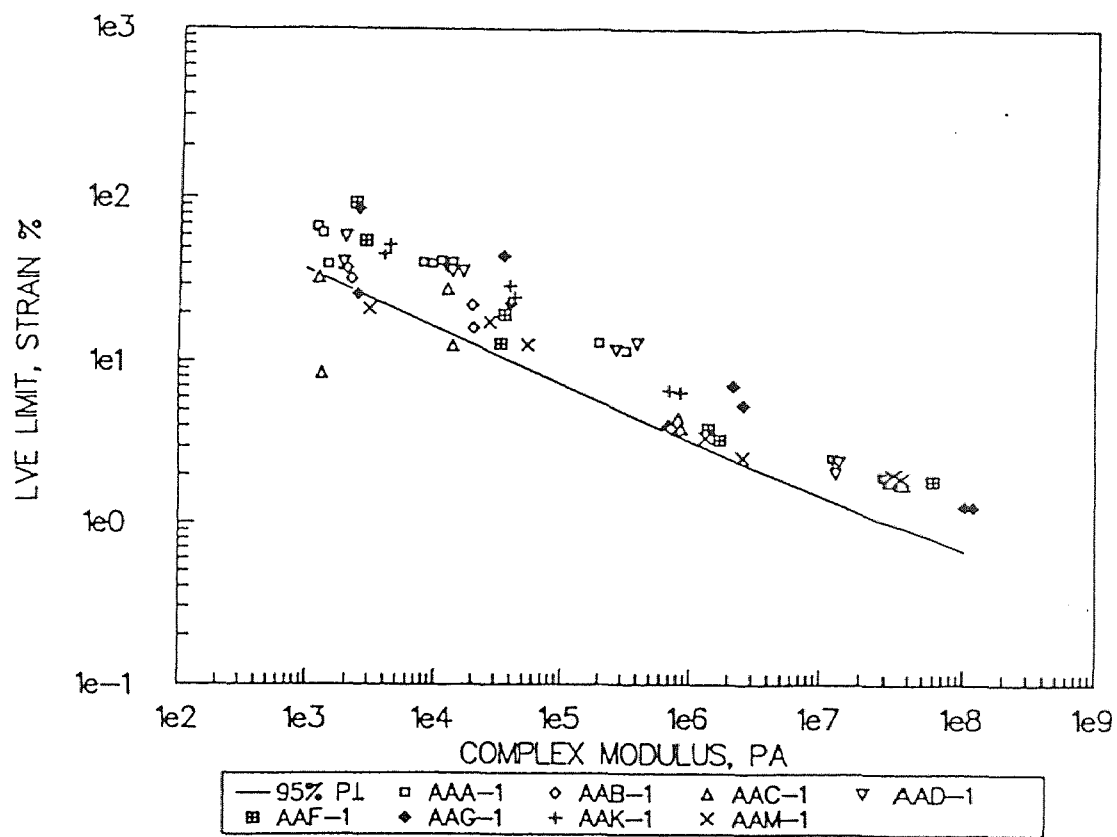


Figure F.4 Limiting Strains for SHRP Core Binders
(Anderson, et al., 1994)

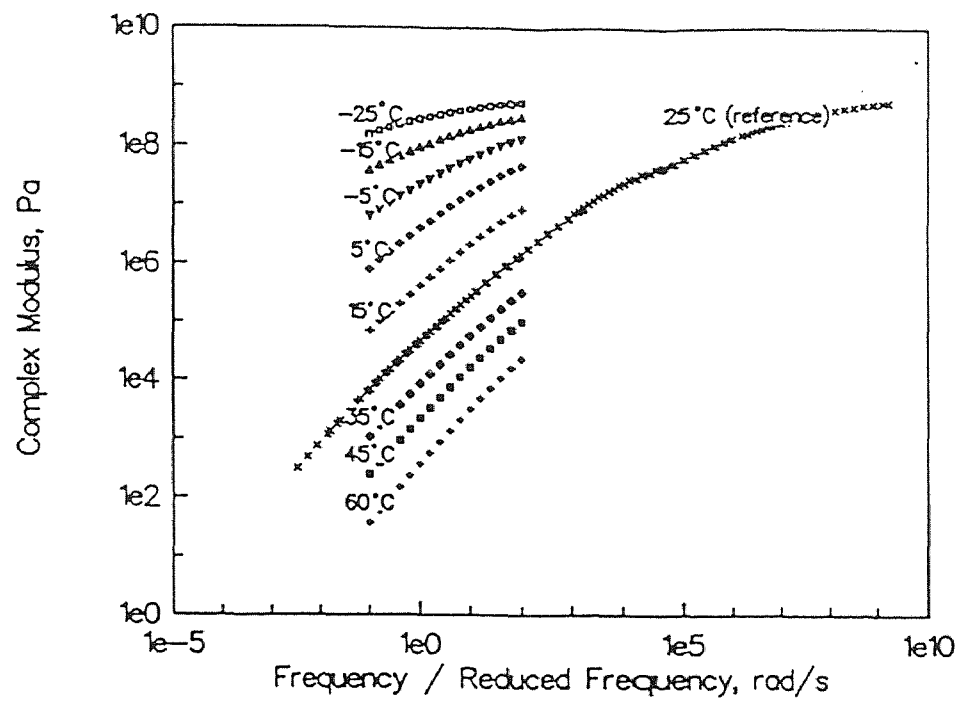


Figure F.5 Complex Modulus at Different Temperatures for DSR Tests
(Anderson, et al., 1994)

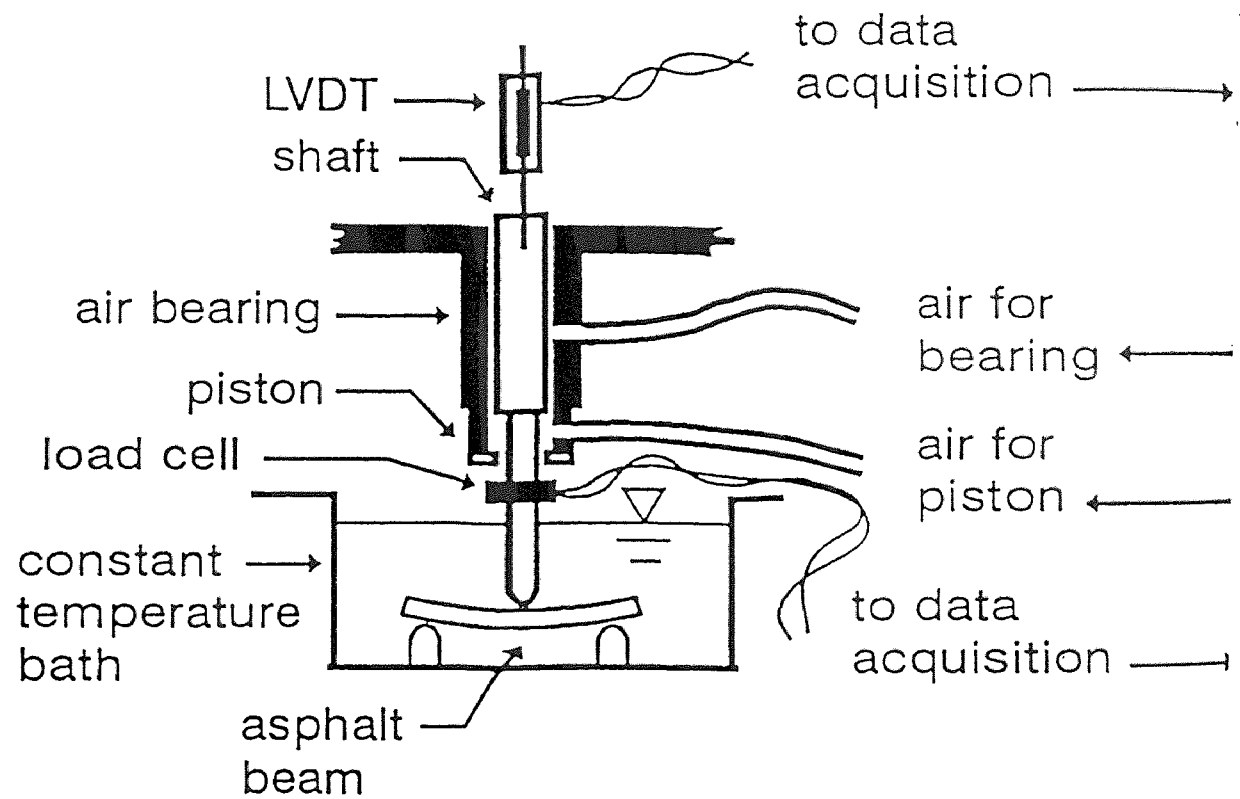


Figure F.6 Bending Beam Rheometer, SHRP Test Method B-002
(Anderson, et al., 1994)

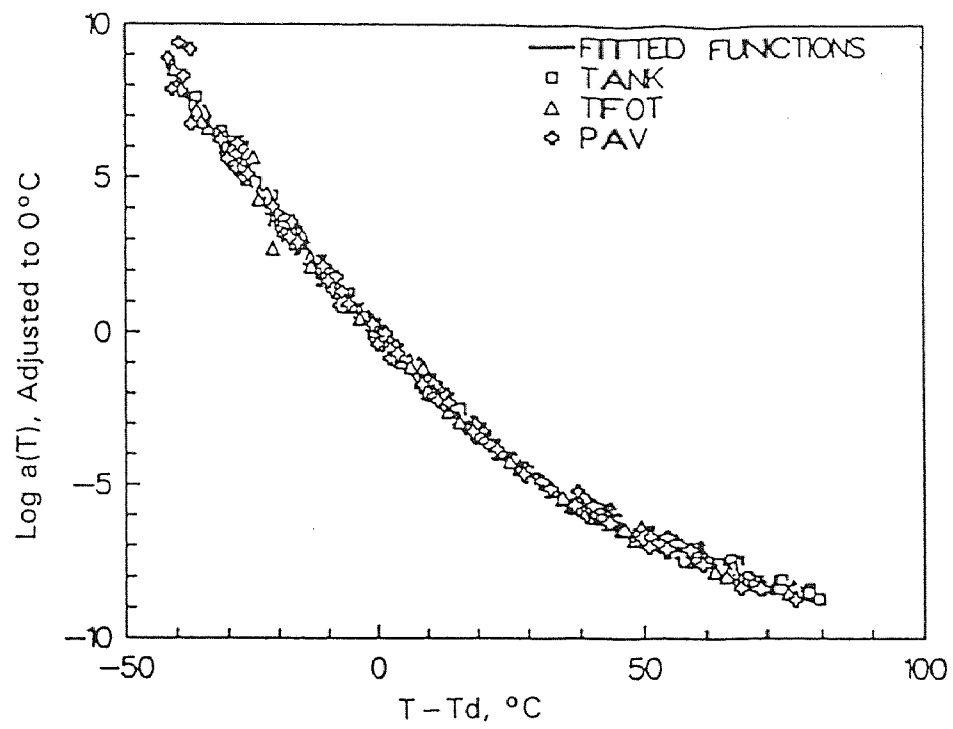


Figure F.7 Shift Factors of SHRP Core Binders
(Anderson, et al., 1994)

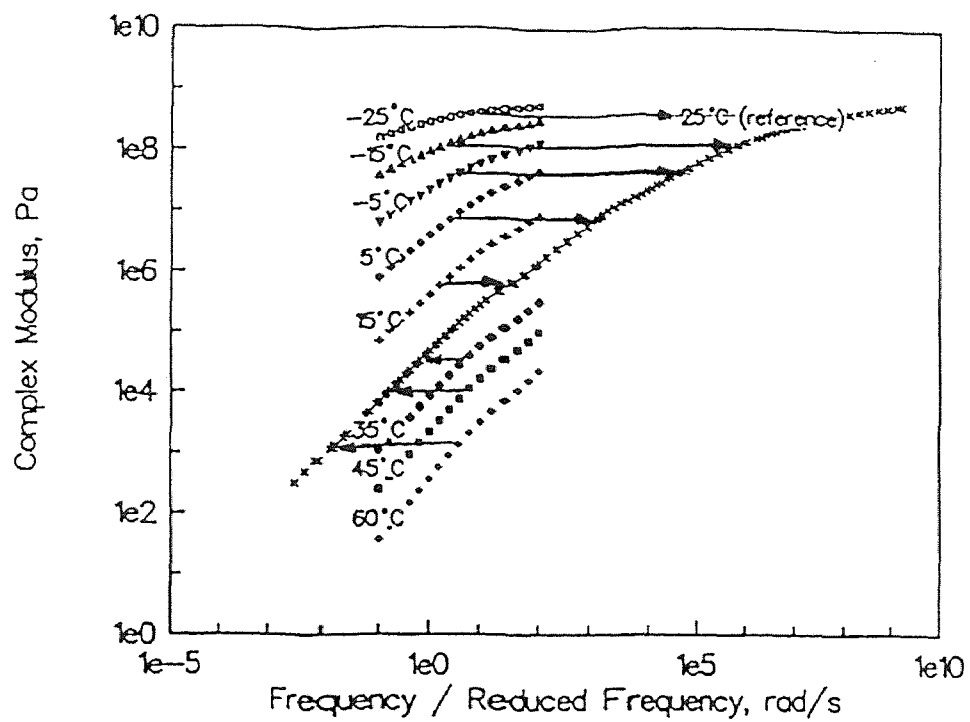
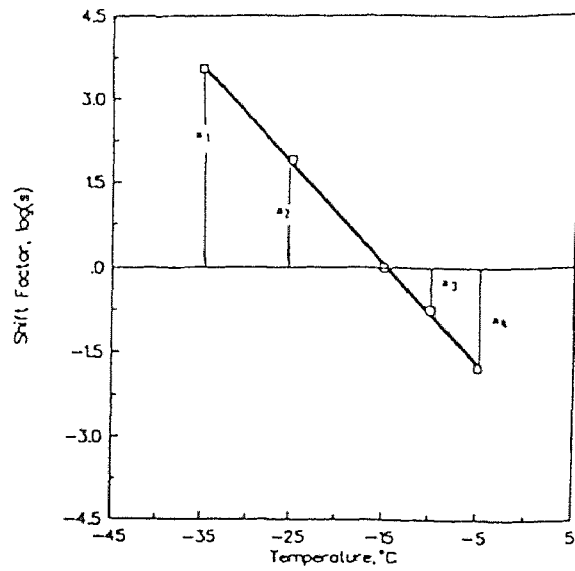
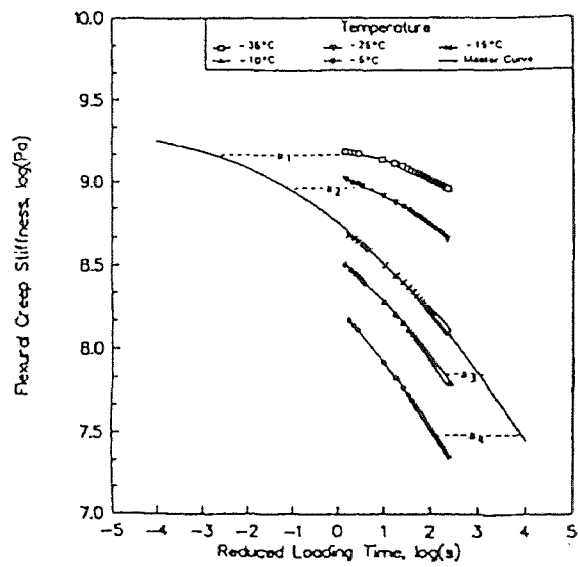


Figure F.8 A Master Curve from DSR Data- Asphalt AAD-1, Tank
(Anderson et al., 1994)



(b)



(a)

Figure F.9 A Master Curve from BBR Data, Asphalt AAM-1
(Anderson, et al., 1994)

APPENDIX G
OBTAINING PARAMETERS OF TWO-PARALLEL-MAXWELL ELEMENT
FROM SHRP BINDER AAB-1 (TANK) MASTER CURVES

OBTAINING PARAMETERS OF TWO-PARALLEL-MAXWELL ELEMENT FROM SHRP BINDER AAB-1 (TANK) MASTER CURVES

The master curves of SHRP binder AAB-1 (Tank) were used to obtain the parameters (E_i , V_i , E_{ii} , V_{ii}) of Two-Parallel-Maxwell element. The followings are the output of Material Utilities of the PACE program (version 1.02) (SWK (PE), Inc., 1994) at 5, 15, 25, and 15 °C.

1. Output for the case of 5 °C

VISCO-ELASTIC PARAMETERS OF 2-MAXWELL-UNIT FLUID FROM FREQUENCY SWEEP DATA 20-NOV-1994

Data from file C:\PACE\TST\AAB05.FSD

FREQUENCY SWEEP DATA

AND_93

AAB-1

TEMPERATURE

(C) 5

FREQUENCY_Hz COMPLEX_SHEAR_MODULUS_PSI PHASE_ANGLE_degrees

OBSERVED SHEAR DATA			DERIVED EXTENSIONAL DATA				
Frequency	Complex	Phase	Complex	Phase	Angular	Storage	Loss
	Modulus	Angle	Modulus	Angle	Velocity	Modulus	Modulus
Hz	psi	degrees	MPa	degrees	rad/sec	MPa	MPa.sec
10.0	54585	9.3	1129.05	9.350	62.8319	1114.05	183.43
5.0	49390	10.4	1021.60	10.400	31.4159	1004.81	184.42
2.0	42571	11.9	880.55	11.930	12.5664	861.53	182.02
1.0	37534	13.2	776.36	13.210	6.2832	755.82	177.42
0.5	32676	14.6	675.88	14.600	3.1416	654.05	170.37
0.2	26638	16.6	550.99	16.620	1.2566	527.97	157.60
0.1	22437	18.3	464.09	18.290	0.6283	440.65	145.64

VISCOELASTIC PARAMETERS FROM NON-LINEAR REGRESSION ON DERIVED STORAGE MODULUS
AND LOSS MODULUS, WITH COMPARISON OF RESULTING COMPLEX MODULUS AND PHASE ANGLE

NB. FOR 2 MAXWELL UNITS, FITTING IS ATTEMPTED WITH 1st 2 FREQUENCIES ONLY

E - V PARAMETERS
FROM REGRESSION

Maxwell Unit No.	E MPa	V MPa.sec
1	1840.	1404.
2	666.5	12.57

RELAXATION SPECTRUM
FROM REGRESSION

Mode Number	Strength MPa	Time seconds
1	919.9	0.76338
2	333.3	0.01885

C O M P L E X M O D U L U S

P H A S E A N G L E

Frequency	Derived	Fitted	Error	Error	Derived	Fitted	Error	Error
Hz	MPa	MPa	MPa	%	degrees	degrees	degrees	%
10.0	1129.1	1129.1	0.0	0.00	9.35	9.35	0.00	0.00
5.0	1021.6	1021.6	0.0	0.00	10.40	10.40	0.00	0.00

S T O R A G E M O D U L U S

L O S S M O D U L U S

Frequency	Derived	Fitted	Error	Error	Derived	Fitted	Error	Error
Hz	MPa	MPa	MPa	%	MPa	MPa	MPa	%
10.0	1114.1	1114.1	0.0	0.00	183.4	183.4	0.0	0.00
5.0	1004.8	1004.8	0.0	0.00	184.4	184.4	0.0	0.00

2. Output for the case of 15 °C

VISCO-ELASTIC PARAMETERS OF 2-MAXWELL-UNIT FLUID FROM FREQUENCY SWEEP DATA 20-NOV-1994

Data from file C:\PACE\TST\AAB15.FSD

FREQUENCY SWEEP DATA

AND_93

AAB-1

TEMPERATURE

(C) 15

FREQUENCY_Hz COMPLEX_SHEAR_MODULUS_PSI PHASE_ANGLE_degrees

OBSERVED SHEAR DATA

DERIVED EXTENSIONAL DATA

Frequency	Complex	Phase	Complex	Phase	Angular	Storage	Loss
-----------	---------	-------	---------	-------	---------	---------	------

	Modulus	Angle	Modulus	Angle	Velocity	Modulus	Modulus
Hz	psi	degrees	MPa	degrees	rad/sec	MPa	MPa.sec
10.0	31129	15.1	643.88	15.080	62.8319	621.71	167.52
5.0	26608	16.6	550.37	16.630	31.4159	527.35	157.51
2.0	21134	18.9	437.14	18.860	12.5664	413.67	141.31
1.0	17428	20.7	360.49	20.690	6.2832	337.24	127.36
0.5	14131	22.6	292.29	22.640	3.1416	269.77	112.51
0.2	10421	25.4	215.55	25.390	1.2566	194.73	92.42
0.1	8100	27.6	167.54	27.610	0.6283	148.46	77.65

VISCOELASTIC PARAMETERS FROM NON-LINEAR REGRESSION ON DERIVED STORAGE MODULUS AND LOSS MODULUS, WITH COMPARISON OF RESULTING COMPLEX MODULUS AND PHASE ANGLE

NB. FOR 2 MAXWELL UNITS, FITTING IS ATTEMPTED WITH 1st 2 FREQUENCIES ONLY

E - V PARAMETERS FROM REGRESSION			RELAXATION SPECTRUM FROM REGRESSION		
Maxwell Unit No.	E MPa	V MPa.sec	Mode Number	Strength MPa	Time seconds
1	931.0	402.5	1	465.5	0.43227
2	602.1	9.99	2	301.1	0.01660

C O M P L E X M O D U L U S					P H A S E A N G L E			
Frequency	Derived	Fitted	Error	Error	Derived	Fitted	Error	Error
Hz	MPa	MPa	MPa	%	degrees	degrees	degrees	%
10.0	643.9	643.9	0.0	0.00	15.08	15.08	0.00	0.00
5.0	550.4	550.4	0.0	0.00	16.63	16.63	0.00	0.00

S T O R A G E M O D U L U S					L O S S M O D U L U S			
Frequency	Derived	Fitted	Error	Error	Derived	Fitted	Error	Error
Hz	MPa	MPa	MPa	%	MPa	MPa	MPa	%
10.0	621.7	621.7	0.0	0.00	167.5	167.5	0.0	0.00
5.0	527.3	527.3	0.0	0.00	157.5	157.5	0.0	0.00

3. Output for the case of 25 °C

VISCO-ELASTIC PARAMETERS OF 2-MAXWELL-UNIT FLUID FROM FREQUENCY SWEEP DATA 20-NOV-1994

Data from file C:\PACE\TST\AAB25.FSD

FREQUENCY SWEEP DATA
 AND_93
 AAB-1
 TEMPERATURE
 (C) 25
 FREQUENCY_Hz COMPLEX_SHEAR_MODULUS_PSI PHASE_ANGLE_degrees

OBSERVED SHEAR DATA				DERIVED EXTENSIONAL DATA			
Frequency	Complex	Phase	Complex	Phase	Angular	Storage	Loss
	Modulus	Angle	Modulus	Angle	Velocity	Modulus	Modulus
Hz	psi	degrees	MPa	degrees	rad/sec	MPa	MPa.sec
10.0	16286	21.3	336.86	21.320	62.8319	313.81	122.48
5.0	13129	23.3	271.56	23.310	31.4159	249.40	107.46
2.0	9604	26.1	198.65	26.120	12.5664	178.36	87.46
1.0	7418	28.4	153.44	28.370	6.2832	135.01	72.91
0.5	5618	30.7	116.20	30.720	3.1416	99.90	59.36
0.2	3774	34.0	78.06	33.970	1.2566	64.74	43.62
0.1	2728	36.5	56.43	36.510	0.6283	45.35	33.57

VISCOELASTIC PARAMETERS FROM NON-LINEAR REGRESSION ON DERIVED STORAGE MODULUS
 AND LOSS MODULUS, WITH COMPARISON OF RESULTING COMPLEX MODULUS AND PHASE ANGLE

NB. FOR 2 MAXWELL UNITS, FITTING IS ATTEMPTED WITH 1st 2 FREQUENCIES ONLY

E - V PARAMETERS			RELAXATION SPECTRUM		
FROM REGRESSION			FROM REGRESSION		
Maxwell	E	V	Mode	Strength	Time
Unit No.	MPa	MPa.sec	Number	MPa	seconds
1	428.2	120.6	1	214.1	0.28170
2	443.7	6.420	2	221.8	0.01447

COMPLEX MODULUS				PHASE ANGLE			
Frequency	Derived	Fitted	Error	Error	Derived	Fitted	Error
Hz	MPa	MPa	MPa	%	degrees	degrees	degrees
							%

10.0	336.9	336.9	0.0	0.00	21.32	21.32	0.00	0.00
5.0	271.6	271.6	0.0	0.00	23.31	23.31	0.00	0.00

S T O R A G E M O D U L U S L O S S M O D U L U S

Frequency	Derived	Fitted	Error	Error	Derived	Fitted	Error	Error
Hz	MPa	MPa	MPa	%	MPa	MPa	MPa	%
10.0	313.8	313.8	0.0	0.00	122.5	122.5	0.0	0.00
5.0	249.4	249.4	0.0	0.00	107.5	107.5	0.0	0.00

4. Output for the case of 35 °C

VISCO-ELASTIC PARAMETERS OF 2-MAXWELL-UNIT FLUID FROM FREQUENCY SWEEP DATA 20-NOV-1994

Data from file C:\PACE\TST\AAB35.FSD

FREQUENCY SWEEP DATA
 AND_93
 AAB-1
 TEMPERATURE
 (C) 35
 FREQUENCY_Hz COMPLEX_SHEAR_MODULUS_PSI PHASE_ANGLE_degrees

OBSERVED SHEAR DATA				DERIVED EXTENSIONAL DATA			
Frequency	Complex Modulus	Phase Angle	Complex Modulus	Phase Angle	Angular Velocity	Storage Modulus	Loss Modulus
Hz	psi	degrees	MPa	degrees	rad/sec	MPa	MPa.sec
10.0	7418	28.4	153.44	28.370	62.8319	135.01	72.91
5.0	5618	30.7	116.20	30.720	31.4159	99.90	59.36
2.0	3774	34.0	78.06	33.970	12.5664	64.74	43.62
1.0	2728	36.5	56.43	36.510	6.2832	45.35	33.57
0.5	1932	39.1	39.96	39.110	3.1416	31.01	25.21
0.2	1186	42.6	24.53	42.600	1.2566	18.06	16.60
0.1	801	45.3	16.57	45.270	0.6283	11.66	11.77

VISCOELASTIC PARAMETERS FROM NON-LINEAR REGRESSION ON DERIVED STORAGE MODULUS AND LOSS MODULUS, WITH COMPARISON OF RESULTING COMPLEX MODULUS AND PHASE ANGLE

NB. FOR 2 MAXWELL UNITS, FITTING IS ATTEMPTED WITH 1st 2 FREQUENCIES ONLY

E - V PARAMETERS
FROM REGRESSION

Maxwell	E	V
Unit No.	MPa	MPa.sec
1	168.2	33.11
2	273.0	3.379

RELAXATION SPECTRUM
FROM REGRESSION

Mode	Strength	Time
Number	MPa	seconds
1	84.12	0.19681
2	136.5	0.01238

C O M P L E X M O D U L U S

P H A S E A N G L E

Frequency	Derived	Fitted	Error	Error	Derived	Fitted	Error	Error
Hz	MPa	MPa	MPa	%	degrees	degrees	degrees	%
10.0	153.4	153.4	0.0	0.00	28.37	28.37	0.00	0.00
5.0	116.2	116.2	0.0	0.00	30.72	30.72	0.00	0.00

S T O R A G E M O D U L U S

L O S S M O D U L U S

Frequency	Derived	Fitted	Error	Error	Derived	Fitted	Error	Error
Hz	MPa	MPa	MPa	%	MPa	MPa	MPa	%
10.0	135.0	135.0	0.0	0.00	72.9	72.9	0.0	0.00
5.0	99.9	99.9	0.0	0.00	59.4	59.4	0.0	0.00

APPENDIX H
CONVERSION BETWEEN TWO-PARALLEL-MAXWELL MODEL AND
BURGERS MODEL

CONVERSION BETWEEN TWO-PARALLEL-MAXWELL MODEL AND BURGERS MODEL

The followings are the derivation of the equations to convert Two-Parallel-Maxwell element parameters to Burgers' element parameters.

The differential equation for Burgers' element is expressed as:

$$E_1 \dot{\varepsilon} + \frac{E_1 E_2}{V_2} \varepsilon = \dot{\sigma} + \left(\frac{E_1}{V_1} + \frac{E_2}{V_2} + \frac{E_1}{V_2} \right) \sigma + \frac{E_1 E_2}{V_1 V_2} \int \sigma dt \quad (\text{H.1})$$

while the differential equation for Two-Parallel-Maxwell element is expressed:

$$(E_i + E_{ii}) \dot{\varepsilon} + E_i E_{ii} \left(\frac{1}{V_i} + \frac{1}{V_{ii}} \right) \varepsilon = \dot{\sigma} + \left(\frac{E_i}{V_i} + \frac{E_{ii}}{V_{ii}} \right) \sigma + \frac{E_i E_{ii}}{V_i V_{ii}} \int \sigma dt \quad (\text{H.2})$$

The Two-Parallel-Maxwell is also known as the “overlay” equivalent to Burgers model.

Therefore, the following relationship can be established:

$$E_1 \equiv E_i + E_{ii} = A \quad (\text{H.3})$$

$$\frac{E_1 E_2}{V_2} \equiv E_i E_{ii} \left(\frac{1}{V_i} + \frac{1}{V_{ii}} \right) = B \quad (\text{H.4})$$

$$\frac{E_1}{V_1} + \frac{E_1}{V_2} + \frac{E_2}{V_2} \equiv \frac{E_i}{V_i} + \frac{E_{ii}}{V_{ii}} = C \quad (\text{H.5})$$

$$\frac{E_1 E_2}{V_1 V_2} \equiv \frac{E_i E_{ii}}{V_i V_{ii}} = D \quad (\text{H.6})$$

Solving the equations (F.3), (F.4), (F.5), and (F.6), we get:

$$E_1 = A \quad (\text{H.7})$$

$$V_1 = \frac{B}{D} \quad (\text{H.8})$$

$$E_2 = \frac{AB^2}{ABC - A^2D - B^2} \quad (\text{H.9})$$

$$V_2 = \frac{A^2B}{ABC - A^2D - B^2} \quad (\text{H.10})$$

Thus, equations (F.7), (F.8), (F.9) and (F.10) can be used to convert the parameters of Two-Parallel-Maxwell element to Burgers model.

REFERENCES

- Ahlborn, G. (1972). Computer Program for Determining Stresses and Deformations in Five Layer Elastic System, University of California, Berkeley.
- Alavi, S. H. (1992). Viscoelastic and Permanent Deformation Characteristics of Asphalt-Aggregate Mixes Tested as Hollow Cylinders and Subjected to Dynamic Axial and Shear Loads, Ph.D. Dissertation, Civil Engineering, University of California at Berkeley.
- Anderson, D.A., Christensen, D.W., Bashia, H.U., Dongre, R., Sharma, M.G., Antle, C.E., and Button, J., (1994). Binder Characterization and Evaluation - Volume 3: Physical Characterization, Strategic Highway Research Program, SHRP-A-369, National Research Council, Washington, DC.
- Asphalt Institute (1994). SUPERPAVE Asphalt Mixture Design, National Asphalt Training Center, Demonstration Project 101, Federal Highway Administration, Office of Technology Applications, Washington, DC.
- Bashia, H.U., Anderson, D.A., and Christensen, D.W. (1992). "The Bending Beam Rheometer: A Simple Device for Measuring Low-Temperature Rheology of Asphalt Binders," Association of Asphalt Paving Technologist, vol. 61, pp. 117 - 148.
- Baumgaertel, M. and Winter, H.H. (1989). "Determination of Discrete Relaxation and Retardation Time Spectra from Dynamic Mechanical Data," Rheologica Acta, vol. 28, pp. 511-519.
- Cambou, B., (1993). "From Global to Local Variables in Granular Material," Powder and Grain, 93', Thorton (ed.), Balkema, Rotterdam, pp. 73-86.
- Chang, K.G., and Meegoda, N.J. (1993). "Simulation of the Behavior of Asphalt Concrete Using Discrete Element Methods," Proceedings of the Second International Conference on Discrete Element Methods, Massachusetts Institute of Technology, Boston, MA, March 18-19, pp. 437 - 448.
- Chen, Y.C. (1986). Experimental Determination of Fabric for Granular Material, Ph.D. Dissertation, Civil Engineering, Cornell University.
- Christensen, D.W. and Anderson, D.A., (1992). "Interpretation of Dynamic Mechanical Test Data for Paving Grade Asphalt Cement," Association of Asphalt Paving Technologist, vol. 61, pp. 67 - 116.

- Cundall, P.A. (1971). "A Computer Model for Simulating Progressive, large scale Movements in Block Rock Systems," Proc. Int. Symp. on Rock Fracture, Nancy, France, II-8.
- Cundall, P.A. (1988). "Computer Simulations of Dense Sphere Assemblies," Micromechanics of Granular Materials, Satake, M. and Jenkins, J. T. (Eds.) Elsevier Science Publishers, Amsterdam, pp. 113-123.
- Cundall, P.A., and Hart, R.D. (1990). Numerical Modeling of Discontinua, Itasca Consulting Group, Inc., Minneapolis, Minnesota.
- Cundall, P.A., and Strack, O.D.L. (1979a). "The Distinct Element Method as a Tool for Research in Granular Media: Part I," Report to NSF, ENG76-20771, Dept. of Civil and Mineral Eng., Univ. of Minnesota.
- Cundall, P.A., and Strack, O.D.L. (1979b). "A Discrete Numerical Model for Granular Assemblies," Geotechnique, vol. 29, pp. 47-65.
- Cundall, P.A., and Strack, O.D.L. (1979c). "The Development of Constitutive Laws for Soils Using the Distinct Element Method," Numerical Methods in Geomechanics: Proc. 3rd Int. Conf. on Numerical Methods in Geomechanical, Aachen, vol. 1, Balkema, Rotterdam, pp. 289-317.
- Dehlen, G.L. (1969). The Effect of Nonlinear Material on the Behavior of Pavements Subjected Traffic Loads, Ph.D. Dissertation, University of California.
- Duncan, J.M., Monismith, C.L., Wilson, E.L. (1968) "Finite Element Analysis of Pavements," Highway Research Record 228, HRB, National Research Council, Washington, D.C.
- Findley, W.N., Lai, J.S., and Onaran, K. (1976). Creep and Relaxation of Nonlinear Viscoelastic Materials, North-Holland Publishing Company, Amsterdam-New York-Oxford.
- Ghaboussi, J., Basole, M.M., and Ranjithan, S. (1993). "Three Dimensional Discrete Element Analysis on Massively Parallel Computer," Proceedings of the Second International Conference on Discrete Element Methods, Massachusetts Institute of Technology, Boston, MA, March 18-19, pp. 95-104.
- Harrigan, E. (1991). "Describing the Relationship Between Asphalt Chemistry and Performance: A Status Report," FOCUS, Strategic Highway Research Program, Washington, D.C., September.

- Hicks, R.G. (1970). Factors Influencing the Resilient Properties of Granular Materials, Ph.D. Dissertation, University of California, Berkeley.
- Jimenez, R. A. (1993). "ASPHALT: A Mixture Design Method to Minimize Rutting," presented at the 72nd Annual Meeting of the Transportation Research Board, Jan. 10 - 14, Washington, D.C.
- Kennedy, and Huber, G. (1993). "The SHRP Final Products: Performance Based Specifications," presented in AAPT (Association of Asphalt Paving Technologists) Annual Meeting, March 22 - 24, Austin, Texas.
- Kim, Y.R., and Little, D.N. (1990). "One-Dimensional Constitutive Modeling of Asphalt Concrete," *Journal of Engineering Mechanics*, ASCE, vol. 116, no. 4, pp. 751 - 772.
- Lee, X. and Dass, W. (1992). Packing Structure Characterization and Micromechanical Modeling of Granular Materials, Annual Technical Report (FY 92), under Scientific and Engineering Technical Assistance (SETA) Contract Number F08635-88-C-0067, Applied Research Associates, Inc., Tyndall Air Force Base, FL.
- Lee, X. and Dass, W. (1993). "An Experimental Study of Granular Packing Structure Changes under Load," *Powder and Grain*, 93', Thorton (ed.), Balkema, Rotterdam, pp. 17-22.
- Lorig, L.J., and Cundall, P.A. (1987). "Modeling of Reinforced Concrete Using the Distinct Element Method," SEM/RILEM Int. Conf. on Fracture of Concrete and Rock, Houston, Texas.
- Meegoda, N.J., and Chang, K.G. (1993). "A Novel Approach to Develop A Performance Based Test for Rutting of Asphalt Concrete," *Proceeds of ASCE Specialty Conference on "Airport Pavement Innovation --- Theory to Practice*, Sept. 8-10, Vicksburg, Mississippi, pp. 126-140.
- Meguro, K., and Hakuno, M. (1989). "Fracture Analyses of Concrete Structures by the Modified Distinct Element Method," *Structural Eng./Earthquake Eng. (Proc. of JSCE no. 410/I-12)*, vol. 6, no. 2, pp. 283s-294s.
- Mindlin, R.D. (1949). "Compliance of Elastic Bodies in Contact," *J. Appl. Mech.*, ASME, vol. 71, pp. A259-268.
- Ng, T.T. (1989). Numerical Simulation of Granular Soil under Monotonic and Cyclic Loading: a Particulate Mechanics Approach, Ph.D. Dissertation, Civil Engineering, Rensselaer Polytechnic Institute.

- Nunn, M.E. Powell, W.D., and Colwill, D.M. (1986). "Theoretical Assessment of the Contribution of Chemcrete Binder to the Performance of Road Pavements," Transport and Road Research Laboratory, Materials Memorandum no. 131.
- Pagen, C., (1972). "Dynamic Structural Properties of Asphalt Pavement Mixtures," Proceedings, Third International Conference on the Structural Design of Asphalt Concrete Pavements, vol. I, University of Michigan, pp. 290-315.
- Pande, G.N., Beer, G., and Williams, J.R. (1990). Numerical Methods in Rock Mechanics, John Wiley & Sons Ltd., England.
- Peltonen, P.V. (1992). "Road Aggregate Choice Based on Silicate Quality and Bitumen Adhesion," J. Trans. Eng., ASCE, vol. 118, no. 1, pp. 50-61.
- Ratnaweera, P. (1992). The Influence of Chemical Contaminants on Shear Strength and Stress-strain Behavior of Clay Soils, Ph.D. Dissertation, Civil Engineering, New Jersey Institute of Technology.
- Roberts, F.L., Kandhal, P.S., Brown, E.R., Lee, D.Y., and Kennedy, T.W. (1991). Hot Mix Asphalt Materials, Mixture Design, and Construction, first edition, NAPA Education Foundation, Lanham, Maryland.
- Schapery, R. A. (1981). "On Viscoelastic Deformation and Failure Behavior of Composite Materials with Distributed Flaws," Advances in Aerospace Structure and Materials, Aerospace Structures and Materials, 01, S. S. Wang and W. J. Renton, eds., pp. 5 - 20.
- Schapery, R. A. (1984). "Correspondence Principles and a Generalized J Integral for Large Deformation and Fracture Analysis of Viscoelastic Media," Int'l J. of Fracture, 25, pp. 195 - 223.
- SUPERPAVE (1994). SUPERPAVE Asphalt Design, National Asphalt Training Center, Demonstration Project 101, Federal Highway Administration, Office of Technology Applications, Washington, DC, Pilot Workshop Edition, February.
- SWK(PE), Inc. (1994). PACE Program: Pavement Analysis and Construction Evaluation, Basking Ridge, New Jersey.
- Tam, W.S., and Brown, S.F. (1988). "Back-Analysis Elastic Stiffness: Comparison Between Different Evaluation Procedures," Proceeding of First International Symposium on Nondestructive Testing of Pavements Back-calculation of Moduli, Baltimore, Maryland, USA, June 29-30.

- Tayebali, A.A., Tsai, B., and Monismith, C.L., (1994). Stiffness of Asphalt-Aggregate Mixes, Strategic Highway Research Program, SHRP-A-388, National Research Council, Washington, DC.
- Thompson, M.R., and Elliot, R.P. (1985). "ILLI-PAVE Based Response Algorithms for Design of Conventional Flexible Pavements," Transportation Research Record 1043, TRB, National Research Council, Washington, D.C.
- Thornton, C., and Barnes, D.J. (1986). "Computer Simulated Deformation of Compact Granular Assemblies," *Acta Mechanica*, vol. 64, pp. 45-61.
- Ting, J. M. (1992). "Computational Laboratory for Discrete Element Geomechanics," *J. Computing in Civil Eng.*, vol. 6, no. 2, pp. 129 - 146.
- Ting, J. M., Corkum, B. T., Kauffman, C. R., and Greco, C. (1989). "Discrete Numerical Model for Soil Mechanics," *J. Geotech. Eng.*, vol. 115, no. 3, pp. 379-398.
- Trent, B.C. (1988). "Microstructural Effects in Static and Dynamic Numerical Experiments," *Key Questions on Rock Mechanics*, P.A. Cundall, eds., Balkema, Rotterdam, pp. 395-402.
- Uemura, D., and Hakuno, M. (1987). "Granular Assembly Simulation with Cundall's Model for the Dynamic Collapse of the Structural Foundation," *Structural Eng./Earthquake Eng. (Proc. of JSCE no. 380/I-7)*, vol. 4, no. 1, pp. 155s-164s.
- Underwood, P. (1983). "Dynamic Relaxation," Chapter 5 of Computational Methods for Transient Analysis, T. Belytscko and T.J.R. Hughes, eds., Elsevier Publication, pp. 245 - 265.
- Van der Poel, C.J., (1954). "A General System Describing the Visco-Elastic Properties of Bitumens and Its Relationship to Routine Test Data," *Journal of Applied Chemistry*, vol. 4, pp. 221 - 236.
- Walton, O.R. (1983). "Particle-dynamic Calculations of Shear Flow," *Mechanics of Granular Materials: New Models and Constitutive Relationships*, J.T. Jenkins and M. Satake, eds., Elsevier Science Publishers, Amsterdam, pp. 327-338.
- Wang, V. (1990). Application of Acoustic to the Studies of Cohesive and Adhesive Strength, Quarterly Report, Part 2, SHRP Contract A002B, University of Southern California, School of Engineering, Center for Asphalt Research, LA, California.

- Ward, I.M. (1983). Mechanical Properties of Solid Polymers, John Wiley & Son, New York.
- White, T.D., Zaghoul, S.M., Anderson, G.L., and Smith, D.M. (1995). "Three Dimensional, Dynamic Finite Element Method (3-DFEM) Analysis of Flexible Pavements for A Moving Aircraft Load," to be presented at the 74th Annual Meeting of the Transportation Research Board, Washington, D.C., January.
- Williamson, R.H. (1972). Environmental Effects in Road Pavements and their Engineering Significance, Ph.D. Dissertation, Department of Civil Engineering, University of Natal, Durban, South Africa.